Coded Aperture Imaging Applied to Pixelated CdZnTe Detectors

by

Sonal Joshi

A dissertation submitted in partial fulfillment
of the requirements for the degree of
Doctor of Philosophy
(Nuclear Engineering and Radiological Sciences)
in the University of Michigan
2014

Doctoral Committee:

    Professor Zhong He, Chair
    Professor Jeffrey A. Fessler
    Professor Kimberlee J. Kearfott
    Associate Professor Sara A. Pozzi

"If I have seen further it is by standing on the shoulders of giants."

~ Sir Isaac Newton

To my mother, Dr. Nisha Joshi,
for sacrificing everything for her daughters' education.

ACKNOWLEDGEMENTS

TABLE OF CONTENTS

LIST OF FIGURES

LIST OF TABLES

LIST OF APPENDICES

LIST OF ABBREVIATIONS

ASIC	Application-Specific Integrated Circuit
CAI	Coded Aperture Imaging
CAR	Cathode-to-Anode Ratio
CS	Compton Scatter
CZT/CdZnTe	Cadmium Zinc Telluride
FOV	Field of View
FCFV	Fully-Coded Field of View
PCFV	Partially-Coded Field of View
PSF	Point Spread Function
FWHM	Full Width at Half Maximum
HEU	Highly Enriched Uranium
HPGe	High-Purity Germanium
MCNP	Monte Carlo N-Particle
MURA	Modified Uniformly Redundant Array
NaI(Tl)	Sodium Iodide
NORM	Naturally Occurring Radiological Material
PE	Photoelectric Effect
POE	Port of Entry
PSF	Point Spread Function
RNG	Random Number Generator
ROI	Region of Interest
SBP	Simple Back Projection
SNM	Special Nuclear Material
SNR	Signal-to-Noise Ratio
URA	Uniformly Redundant Array
WGU	Weapons Grade Uranium

ABSTRACT

In the past decade, there has been a significant increase in demand for radiation detectors to detect, identify, and locate potentially threatening nuclear materials. The Polaris system was developed to be used for such applications. This portable, room-temperature operated detector system is composed of 18 thick CdZnTe detectors, and has the ability to detect gamma rays of energies between 30 keV and 3 MeV with an energy resolution <1% FWHM at 662 keV. Detection is extended to source directionality using Compton imaging to map out gamma-ray distributions in 4-pi space. This modality is most effective at imaging gamma-ray energies greater than 300 keV. Due to the low Compton-interaction probability in CdZnTe at lower energies, an alternate imaging technique, coded aperture imaging (CAI), was implemented to extend gamma-ray imaging to the energy range where photoelectric absorption is most probable. The purpose of this work is to describe the evolution of the CAI modality as applied to the Polaris system.

During the course of this study, for the first time, CAI is applied to thick 3D position sensitive CdZnTe detectors to image lower-energy gamma rays. With the knowledge of 3D positions of gamma interactions, masks are applied to five of the six sides of a single CdZnTe crystal, extending the field-of-view (FOV) to near 4-pi through simulation and measurement. Material properties such as "pixel jumping" that are caused by non-uniform electric fields within the detector that result in degradation of image quality are also studied. Next, a single mask is applied to a 3 × 3 array of detectors showing improved image quality when combining images from multiple detectors. Finally, CAI is combined with Compton imaging and applied to the 18-detector Polaris system allowing for the extension of gamma-ray imaging capabilities across the entire dynamic range of the electronic readout system. This work was funded by the US Department of Homeland Security Domestic Nuclear Detection Office and National Science Foundation Academic Research Initiative.

PART I
BACKGROUND/MOTIVATION

CHAPTER 1
INTRODUCTION

The 9/11 terrorist attacks prompted a surge in interest and funding in radiation detection for homeland and national security purposes to protect U.S. citizens from a potential nuclear or radiological terrorist attack. Laboratories across the country were challenged to provide neutron and gamma-ray detection systems to be placed at various Ports of Entry (POE), including radiation portal monitors for border protection. In a limited amount of time, scientists and engineers adapted existing technologies and put them to best use, producing radiation portal monitors and other detection technologies for homeland security applications.

The abundance of research and development funds led to technological development that benefited other applications, as well. This research most directly benefited domestic and international efforts in nuclear safeguards, treaty verification, emergency response, as well as other fields such as nuclear power plant monitoring, medical diagnosis and treatment, and astronomical observation. The constant improvement and development of technology has resulted in a symbiotic relationship between the various fields that rely on similar technology.

Nonetheless, some key challenges remain in radiation detector technology. Research groups around the world are constantly striving towards developing more sensitive, higher-resolution spectrometers and imagers that are also portable, efficient, and room-temperature operated to quickly and effectively detect, identify, and locate nuclear materials of interest. The research group at the University of Michigan has developed a system that meets most of the needs of the community. However, until recently, the device did not image gamma rays of lower energies, where many special nuclear material (SNM)

lines exist. This thesis focuses on the path that was taken and challenges associated with extending gamma-ray imaging to lower energies.

1.1 Gamma-ray Spectrometry

In many situations, radiation levels are sufficiently higher than background such that the use of a simple Geiger counter indicating whether or not radiation is present is adequate for most applications. However, in scenarios where source levels are on the order of background levels, or in the case where material characterization such as isotope identification is sought after, the use of spectrometry is essential.

Radioactive isotopes emit radiation with unique characteristics, such as particle type and energy. With the use of spectrometry, measured intensity versus energy information can be used to detect materials of interest (e.g. Special Nuclear Material [SNM]) and to differentiate them from non-threatening sources (e.g. Naturally Occurring Radioactive Material [NORM], medical and industrial isotopes). This study focuses on identifying and discriminating sources based on gamma-ray emissions.

Characteristics of an effective gamma-ray spectrometer include high efficiency and low energy resolution. Efficiency is directly a function of the detector's ability to attenuate incident gamma rays. High efficiency can be achieved by 1) using large volume (thick) detectors, and 2) selecting materials with high atomic number and densities, both of which increase the number of electrons in the gamma ray's path, thus increasing its probability of interaction. When interacting, some or all of the gamma ray's energy is transferred to the electrons. This energy can be measured and used to form an energy spectrum. An energy spectrum is a histogram of counts versus energy bins, representing each of the gamma-ray interactions and corresponding energy depositions.

The quality of the energy spectrum can be measured by its energy resolution. Energy resolution characterizes a system's ability to differentiate two neighboring peaks in an energy spectrum, usually in units of keV or Full Width at Half Maximum (FWHM). The FWHM is defined as "the width of the distribution at a level that is just half the maximum ordinate peak" and is shown graphically in Figure 1.1 [1]. In most cases, the FWHM is measured at 662 keV using a Cs-137 source.

$$\text{Resolution } R = \frac{FWHM}{H_0}$$
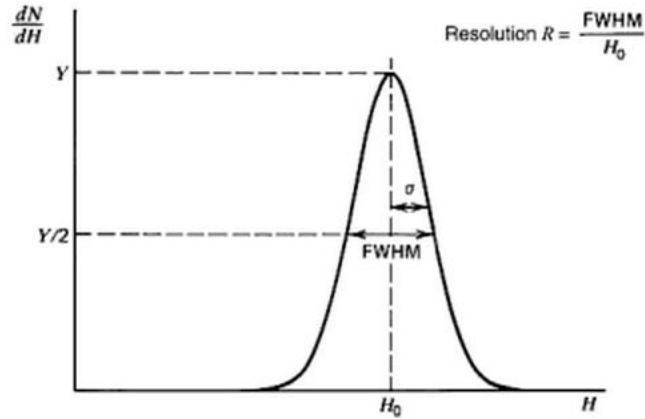
Figure 1.1: Full width at half maximum (FHWM) is a metric often used to describe the energy resolution of a radiation detection system.

The finer the energy resolution, the better two neighboring peaks can be differentiated. Energy resolution is affected several factors. One factor is the material itself, limited by the number of charge carriers (e.g. electron-hole pairs) produced per unit energy by the gamma-ray interaction with the detector material. Energy resolution is also affected by non-material properties, such as electronic noise of the system. Devices range from poor to fine energy resolution. Generally, the energy resolution requirement is dependent on the application space, since a system's peak discrimination ability is only as good as its energy resolution.

The most prevalent gamma-ray spectrometers are scintillators. One example is sodium iodide (NaI(Tl)), which provides an energy resolution of about 6% FWHM at 662 keV [2]. Gamma rays interact with the scintillating material and produce visible light, which is then converted to an electrical signal using a photomultiplier tube. The benefits of these detectors include low cost, highly durability, minimal calibration requirements, and low power demand. Due to theoretical limitation of the material, scintillator energy resolution may not be low enough to identify and discriminate isotopes whose peaks are very close in energy.

On the other end of the spectrum are semiconductor detectors, in particular high purity germanium (HPGe), which provides excellent energy resolution of about 0.5% FWHM at 662 keV, which allows for very precise discrimination between peaks. Semiconductor detectors rely on the production of charge carriers (electrons and holes).

An applied voltage across the detector volume causes the charge carriers to drift, producing an electronic signal that is then read out. Unfortunately, due to the narrow band gap, HPGe detectors must be cooled to liquid nitrogen temperatures to reduce noise from thermal excitation. Therefore, the application space of these detectors is still limited, even with the use of mechanical coolers.
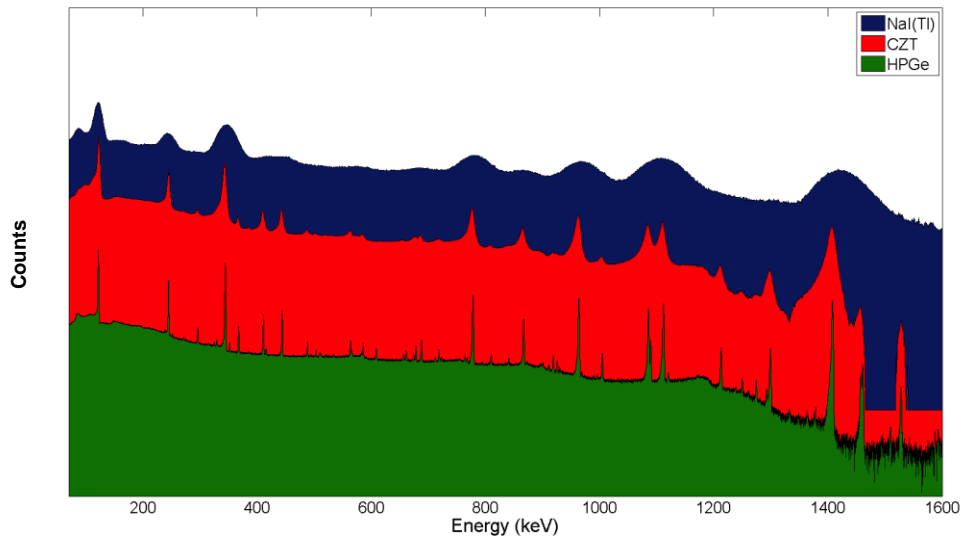
Figure 1.2: A comparison of the energy spectra for NaI(Tl), CdZnTe, and HPGe detector types.

The research group at University of Michigan has been investigating the use of wide band gap semiconductor materials that can provide close to HPGe energy resolution, around 1% FWHM at 662 keV, at room temperature operation. One such material is cadmium zinc telluride (CdZnTe or CZT). Characteristics that make CdZnTe a good gamma-ray detector include wide bang gap, high stopping power, and high electron mobility. One challenge is the difficulty to grow large volumes without impurities, although companies such as Redlen Technologies have made great strides in this area in the past few years, making thick 3D position sensitive CdZnTe a viable radiation detector material for mass production. The Polaris system, developed at the University of Michigan, is made up of an array of CdZnTe crystals, and is described in further detail in Chapter 2.

1.2 Gamma-ray Imaging

In addition to gamma ray spectrometry, which allows for the discrimination of various isotopes, source directionality provides the user with a sense of the distribution of radiation in space. Imaging is especially useful for two reasons. Not only does it provide the shape of the source distribution, it also allows for discrimination and location of weak sources over background. This is especially important when the source of interest is composed of the same isotopes, or energy lines, as an extended background.

Given 3D interaction and energy deposition information, algorithms such as Compton imaging can be utilized to determine the distribution of radiation in space. Due to the relatively low Compton-interaction probability at energies below 200 keV in the CdZnTe, gamma rays at these energies must be imaged using an alternative method. Coded Aperture Imaging (CAI) is an imaging technique that can be used to image low energy gamma rays, where photoelectric absorption is the dominant gamma-ray interaction mechanism. Both Compton imaging and CAI techniques with be discussed in further detail in the next few chapters, as gamma-ray imaging is the focus of this thesis.

1.3 Motivation

Detection for nuclear security applications requires excellent energy resolution for proper isotope identification, especially when measurements are taken in environments where background levels are significant. In addition to energy resolution, source directionality provides the users with much greater knowledge of the surroundings and differentiates between sources of interest and background, allowing for fewer false alarms at border crossings, and much faster identification of rogue materials.

In some cases, gamma-ray imaging may be necessary to gamma ray imaging may be necessary to locate nuclear materials of interest. Materials of highest concern include Highly Enriched Uranium (HEU), Weapons Grade Uranium (WGU), and all isotopes of plutonium. HEU is composed of U-238, trace amounts of U-234, but most importantly, at least 20% U-235, which emits gamma rays with energy of 186 keV. WGU is composed of the same components, but with a much higher U-235 enrichment of at least 90%. Plutonium is composed of Pu-238, Pu-239, Pu-240, and Pu-241, giving off many low intensity gamma rays ranging from 52 keV to 770 keV.

Polaris is a good candidate for nuclear security applications as it is highly portable, room-temperature operated, and can provide gamma ray spectroscopy with an energy resolution of around 1.0% FWHM at 662 keV. The dynamic range extends from 30 keV to 3 MeV, which spans the gamma ray energies of interests. Since the system was originally developed to be a Compton imager, until recently, imaging capabilities were limited to energies above 200 keV in CdZnTe, as Compton imaging is most affective in an energy range where gamma rays will most probably Compton scatter. Since the system was essentially blind to the directionality of single-interaction, photoelectric events, it was very important to extend gamma-ray imaging to lower energies to determine the location of the low-energy sources. This was done through the application of coded aperture masks and implementation of CAI.

1.4 Contribution of this Work

The work presented in this thesis contributes to the capabilities of the Polaris detector technology, as well as to the field of radiation detection and imaging in a few ways. The first is the extension of gamma-ray imaging to lower energies using CdZnTe material, in an energy range where Compton imaging is less effective due to low Compton scatter probability at these energies. In addition, since it was the first time that CAI is applied to thick (15 mm) pixelated CdZnTe detectors, additional challenges were posed. For example, when utilized in the low-energy range, CdZnTe is more susceptible to consequences of material defects such as pixel jumping.

Due to the fact that 3D gamma-ray interaction positions are known, for the first time, multiple masks were applied to a single detector, extending the limited field of view (FOV) to near 4-pi and making the CAI FOV more comparable to the existing Compton imaging modality. A single mask was also applied to the cathode side of an array of detectors, showing the improvement in signal-to-noise ratio (SNR) when combining images from multiple detectors of various quality. The final contribution of this work is the combination of CAI and Compton imaging modalities using the 18-detector Polaris system

This system has been demonstrated and utilized by users at facilities all over the US. The CAI contribution has allowed for the imaging and characterization of radioactive

materials, particularly in the low-energy domain where many special nuclear material (SNM) gamma-ray emissions lie.

1.5 Focus of this Thesis

The focus of this thesis is to design a CAI system for Polaris to extend gamma-ray imaging to lower energies. The thesis is divided into three parts: Part I introduces CdZnTe detector material in Chapter 1, the need to extend gamma-ray imaging to lower energies using CAI in Chapter 2, and provides basic CAI theory in Chapter 3.

Part II focuses on near 4-pi CAI by applying multiple masks to a single detector. This is theoretically demonstrated in Chapter 4 using Monte Carlo simulations, by first applying a single mask to the cathode side, then masks to the non-cathode sides. Chapter 5 extends the investigation to a bench top demonstration of CAI using radiation check sources, revealing material properties that affect the quality of CAI using thick 3D CdZnTe detectors. These properties are then studied in further detail in Chapter 6.

Finally, Part III focuses on the benefits of applying coded aperture masks to an array of 3D CdZnTe in Chapter 7. All of the work leads up to Chapter 8, which describes the state of CAI as applied to the current Polaris system. Lastly, Chapter 9 summarizes the work presented in this thesis, and describes possible directions for future work.

1.6 References

[1]   G.F. Knoll, Radiation Detection and Measurement. New York: John Wiley & Sons, Inc., third ed., 2000.

[2]   Cherry, S. R., J. A. Sorenson, and M. E. Phelps, Physics in Nuclear Medicine. Elsevier, fourth ed., 2012.

CHAPTER 2

PIXELATED CdZnTe Detectors

As described in Chapter 1, pixelated CdZnTe detectors were developed and studied due to a need for room-temperature operated detectors that would provide excellent energy and position resolution to be used for gamma-ray detection and imaging. Large-volume CdZnTe detectors, each with the dimension of $2.0 \times 2.0 \times 1.5$ cm^3, were provided by Redlen Technologies. The current system, Polaris II, is composed of two 3×3 arrays of CdZnTe detectors, with a total volume of 108 cm^3, resulting in a relative efficiency of about 30%, as compared to 3×3 NaI(Tl) at 1332 keV.
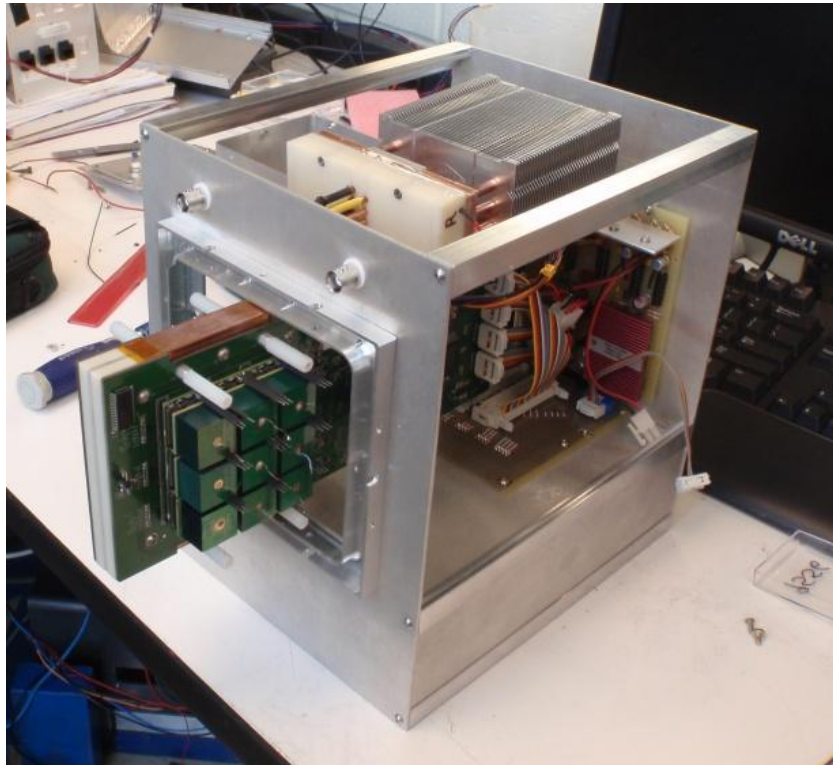
Figure 2.1: Current 18-detector Polaris system with aluminum enclosure removed, consisting of two 3 × 3 planes of large-volume CdZnTe detectors [1].

Separated by 2 mm, each detector has a planar cathode held at approximately -3000 V, and a grounded pixelated anode. The 11 × 11 anode pixels have a pitch of 1.72 mm, separated by a common steering grid held at a negative bias. The signal from each pixel is read out using an application specific integrated circuit (ASIC) developed by Gamma Medica – Ideas. With this, each individual detector is capable of identifying 3D gamma-ray interaction positions with millimeter-scale position resolution and energy depositions with resolution less than 1% FWHM at 662 keV for the combined 18-detector energy spectrum.
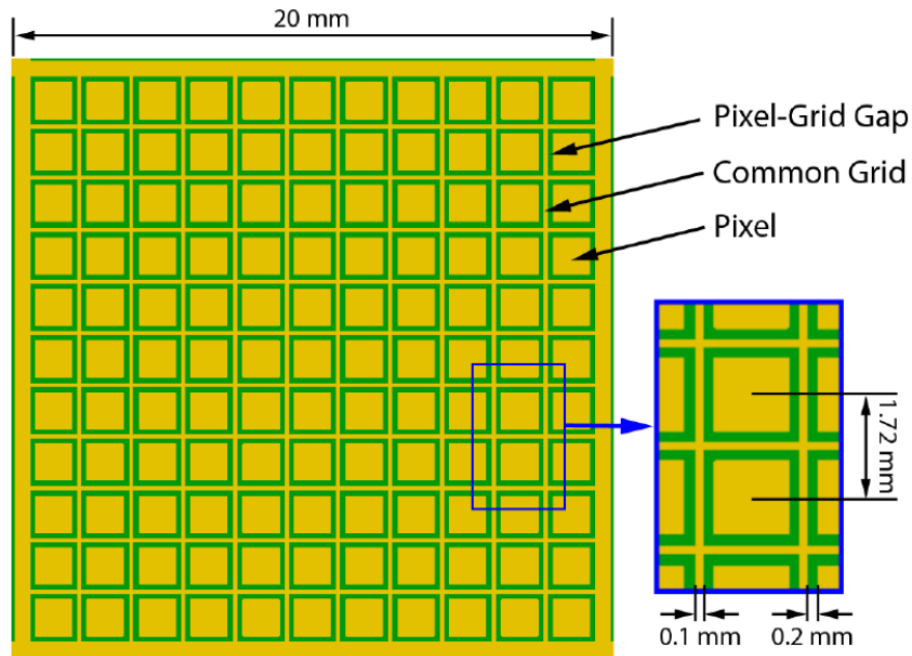
Figure 2.2: Each CdZnTe detector has a planar cathode and 11 ×11 pixelated anode, with a pixel pitch of 1.72 mm, separated by a common grid [2].

2.1 Detector Physics

When a gamma ray interacts with the detector crystal, its energy is fully or partially transferred to the material via creation of electron-hole pairs. The number of electron-hole pairs created from each interaction is a stochastic process, but is on average proportional to the gamma-ray energy deposited. As soon as an electron cloud is formed, the cloud begins to drift away from the cathode due to its negative bias, inducing charge on both the cathode and anode. Unlike HPGe, CdZnTe detectors rely on single-polarity charge sensing

since the holes are essentially stationary relative to the electrons, due to slow hole mobility.
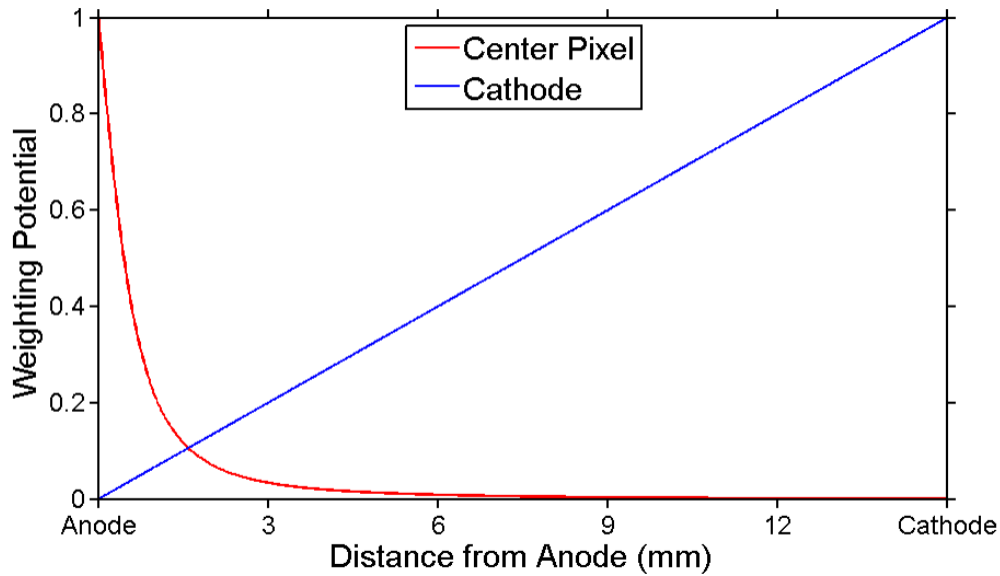
Figure 2.3: Cathode and anode weighting potential as a function of interaction depth. The induced charge is proportional to the difference between the initial and final weighting potential based on the depth of interaction [2].

The charge induced on the cathode and pixelated anode can be predicted using the Shockley-Ramo theorem [3]. As shown in Figure 2.3, the weighting potential of the cathode is linearly proportional to the depth of interaction. As for the pixelated anodes, due to the nature of the small-pixel effect, the induced charge is shared amongst many pixels for most of the detector volume, resulting in a relatively small and flat weighting potential that is (nearly) independent of interaction position. As the electron cloud approaches the anode, the weighting potential quickly increases as it nears the pixel under which it interacted, as shown in Figure 2.4. This generally results in full charge induction of a single anode pixel (ignoring charge sharing effects), providing the user with the x-y position of the interaction. These are known as single-pixel events. The large weighting potential near the anode results in a few millimeter dead region, which limits low energy gamma detection and imaging on that side.
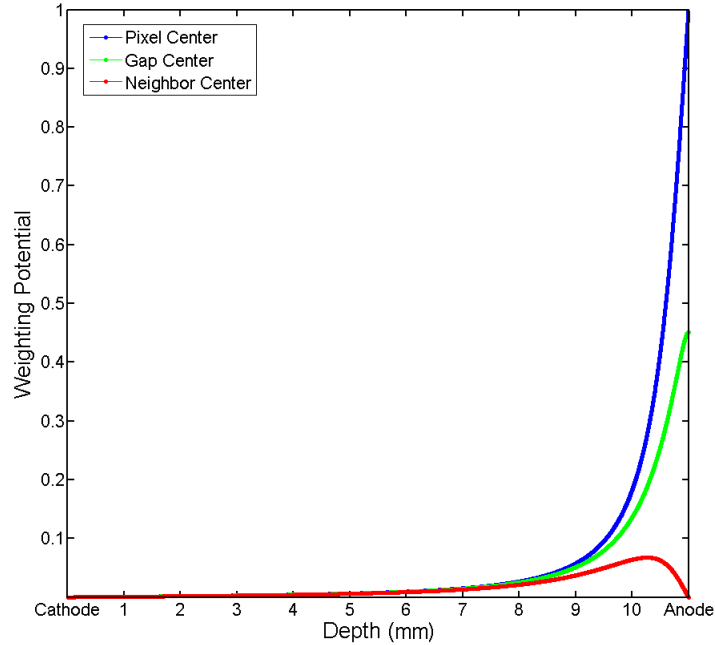
Figure 2.4: Anode weighting potential versus depth for three positions relative to the center of the collecting pixel.

The third dimension, depth, is calculated through a novel technique by taking the ratio of the cathode and anode signals, known as the Cathode-to-Anode Ratio (CAR) [4]. This is possible due to the fact that the cathode signal amplitude is a function of interaction depth, while the anode signal amplitude is essentially independent of interaction depth. Depth of interaction can also be determined by measuring the electron cloud drift time, or the time between the initial interaction and collection at the anode [5].

After extensive signal processing, the energy depositions and interaction positions (x, y, depth) for each event are read out by the system. The position information is not only essential for proper spectroscopic correction, but also allows for source localization using various gamma-ray imaging techniques [2].

2.2 Gamma-Ray Interactions in CdZnTe

In CdZnTe material, gamma rays in the 30 keV to 1 MeV energy range are most likely to undergo two main interaction types: photoelectric effect (PE) or Compton scattering (CS). In the photoelectric absorption process, the gamma ray interacts with a bound electron and is completely absorbed. This interaction is only possible when the gamma

energy exceeds the binding energy of the electron. Through this process an electron, usually bound by the K shell, is emitted. The excess gamma-ray energy is transferred to the electron as kinetic energy, calculated as

$$E_e = E_\gamma - E_B \tag{2.1},$$

where E_e is the kinetic energy of the electron, E_γ is the initial gamma-ray energy, and E_B is the electron binding energy. Photoelectric absorption results in full-energy deposition of the incident gamma ray, creating a photopeak in the recorded energy spectrum once many gamma rays of equal incident energy are absorbed. As the gamma-ray energy increases from tens to hundreds of keV, Compton scatter becomes the most likely gamma-ray interaction. In this process, the gamma ray interacts with a loosely bound electron, transferring some of its energy to the electron and any excess energy to a secondary gamma ray. The amount of energy transferred and angle at which the gamma ray scatters are related by the Compton scatter formula:

$$E_\gamma' = \frac{E_\gamma}{1 + \frac{E_\gamma}{m_o c^2}(1 - \cos\theta)} \tag{2.2},$$

where E_γ and E_γ' are the initial and scattered gamma-ray energies, respectively, $m_o c^2$ is the rest mass energy of an electron, and θ is the gamma-ray scatter angle [6]. If the gamma ray were to scatter and then escape the detector material, the result is a partial energy deposition; these events contribute to the Compton continuum in an energy spectrum. However, if the gamma ray is ultimately absorbed via photoelectric absorption, a full-energy deposition occurs.

Whether the gamma ray is likely to interact under photoelectric effect or Compton scatter is a function of the gamma-ray energy, as well as the material composition and density. In CdZnTe material, the transition region between the two interaction types occurs around 200 keV, as shown in Figure 2.5.
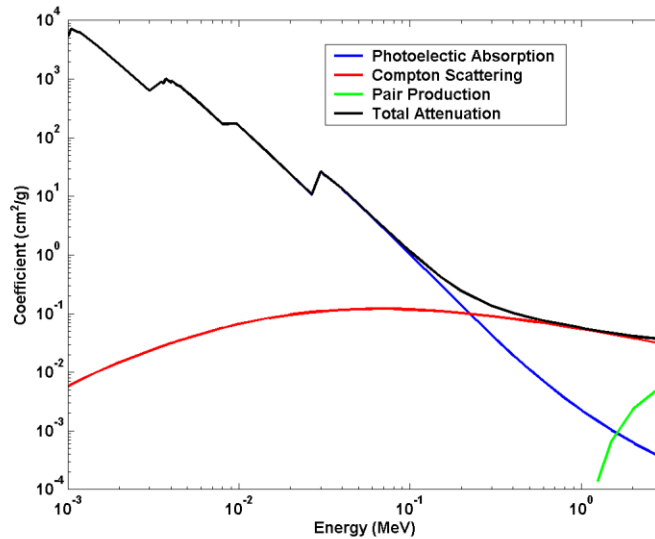
Figure 2.5: Gamma-ray attenuation coefficients and interaction mechanisms in the energy range of interest in CdZnTe material [7].

2.3 Compton Imaging and Limitation

If a gamma ray interacts at least twice in a detector (CS + PE or CS + CS + …) and the positions and energy depositions of its first two interactions is known, the direction of the source can be limited in space through the Compton imaging technique. With this information, using the Compton scatter equation (Eq. 2.2), the scatter angle of the gamma ray (θ) can be calculated. With this, the possible incident directions of the gamma ray are limited to the surface of a cone and can be back projected into space around the detector. Since the electron scatter angle is unknown, the azimuthal angle within the cone's surface is ambiguous. After multiple gamma rays interact within the detector, these cones begin to overlap in space at a single point, indicating the direction of the source.

Traditionally, Compton imagers require two or more detectors, consisting of a scatter plane where Compton scatter occurs, and absorption plane where the gamma ray subsequently undergoes photoelectric absorption. However, due to the system's 3D position sensitivity and ability to differentiate multiple interactions occurring close in time within a single crystal, imaging can be implemented not only using multiple detectors, but a single detector, which greatly improves the Compton imaging efficiency.

13
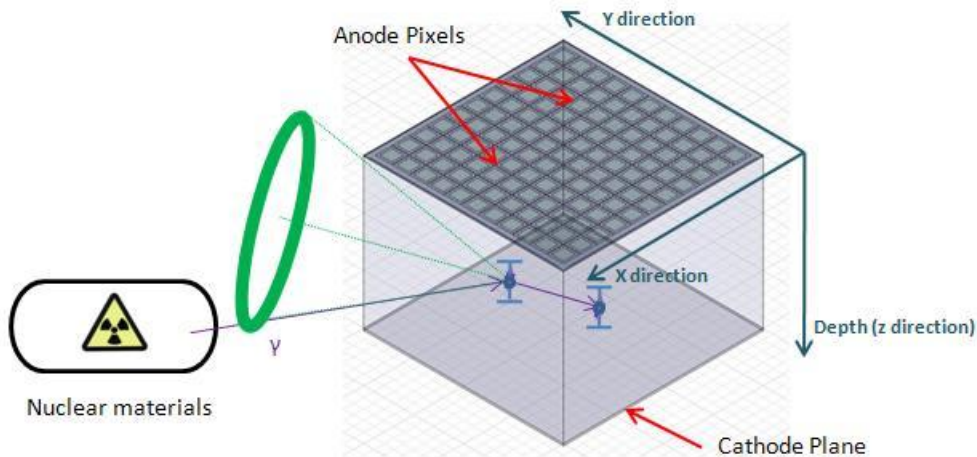
Figure 2.6: Multiple scatter event and resultant Compton cone in 3D position sensitive CdZnTe.

Unfortunately, Compton imaging requires that the gamma ray interacts at least twice in the detector system. In the energy range where photoelectric absorption dominates, below 200 keV or so, Compton imaging is less feasible, if at all. Although the presence of low-energy gamma rays is indicated through gamma-ray spectroscopy, the user is essentially "blind" to the direction or location of these sources. For practical applications, a method needed to be developed and implemented to seamlessly extend gamma-ray imaging to lower energies.

2.4 Low-Energy Solution

To extend gamma-ray imaging to photoelectric energies, an attenuation-based method was investigated to utilize single-interaction events. However, the method was limited by the fact that it could only locate multiple point sources if they were at different energies [8]. Due to this limitation, coded aperture imaging (CAI) was the next possible solution considered. It had been put aside until then since the method inherently reduces gamma-ray flux, due to the attenuating coded mask (as described in Chapter 3). Despite the loss in efficiency, the technique has been proven in medical imaging and astrophysics applications to image multiple point sources of the same energy while providing images with angular resolutions comparable to Compton imaging.

2.5 References

[1]   Boucher, Y. A., "Analysis of Cadmium Zinc Telluride Detector Performance and Characteristics for Applications in Gamma-Ray Imaging Spectrometers," Ph.D. Thesis, University of Michigan, 2013.

[2]   Kaye, W. R., "Energy and Position Reconstruction in Pixelated CdZnTe Detectors," Ph.D. Thesis, University of Michigan, 2012.

[3]   He, Z. "Review of the Shockley-Ramo theorem and its application in semiconductor gamma-ray detectors," Nuclear Instruments and Methods in Physics Research Section A, volume 463, issue 1-2, pp 250-267, May 2001.

[4]   Z. He et al "1-D position sensitive single carrier semiconductor detectors" NIMA 380 (1996) 228 – 231.

[5]   Li, W. "Three-dimensional position sensitive CdZnTe gamma ray spectrometers," Ph.D. Thesis, University of Michigan 2001.

[6]   Knoll, G.F., "Radiation Detection and Measurement." New York: John Wiley & Sons, Inc., third ed., 2000.

[7]   Berger, M. J., J.H. Hubell, S. M. Seltzer, J. Chang, J. S. Coursey, R. Sukumar, D. S. Zucker, and K. Olsen, "XCOM: Photon Cross Section Database," *NIST Standard Reference Database 8 (XGAM)*, 1998.

[8]   Kaye, W. R., N. D. Bennet, C. G. Wahl, Z. He, and W. Wang. "Gamma-Ray Source Location by Attenuation Measurements." IEEE Nuclear Science Symposium Conference Record, (2007).

CHAPTER 3
CODED APERTURE IMAGING

Coded aperture imaging is the proposed solution to extending gamma-ray imaging to low energies where photoelectric absorption dominates in CdZnTe detector materials. This chapter is a brief description of coded aperture imaging (CAI) history, theory, and implementation. The intent is to provide the reader with sufficient knowledge to understand the following chapters regarding use of CAI with 3D CdZnTe detectors. References are included for further reading.

The main reason for the application of CAI in this scenario is to determine the source direction given only single-interaction events in the detector, rather than the multiple-interaction events required for Compton imaging. To determine the direction of a source given a single interaction with a bare detector system would be almost impossible since the gamma ray could have originated from any direction with nearly the same probability. The application of a coded mask limits the possible source directions using attenuation, allowing for the identification of the source location in space.

3.1 Coded Aperture Imaging Principles

Coded aperture imaging is based on the concept of a pinhole camera, which consists of an attenuating material, separating the detector plane from the emitting source, and a single pinhole through which light or radiation can pass, as shown in Figure 3.1. The pinhole camera has the potential to provide excellent angular resolution, however it results in poor efficiency due to loss of counts to the attenuating material.
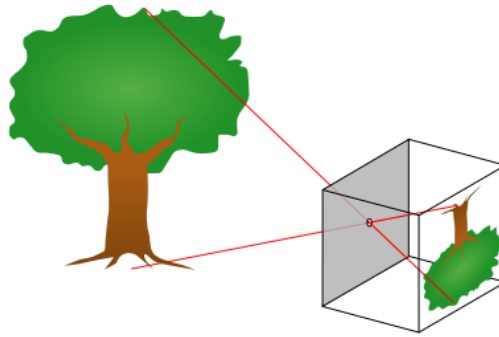
Figure 3.1: The basic concept behind a pinhole camera, a pinhole separating the object from the detector plane [1].

Coded aperture imaging was developed to preserve angular resolution while improving efficiency. Rather than using an attenuating plane with a single pinhole, a coded mask with a larger fraction of "open" (transparent/non-attenuating) to "closed" (opaque/attenuating) elements are used, as shown in Figure 3.2.
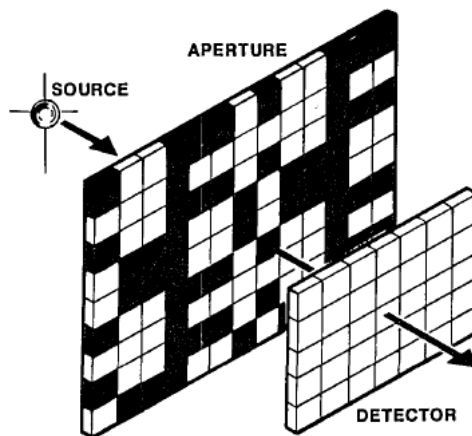
Figure 3.2: The basic concept behind coded aperture imaging, a coded aperture mask separating the source from the position-sensitive detector plane [2].

The image formation in this multiplexing technique consists of two steps. The first is a physical modulation of the incident radiation by the mask. The second is to use an algorithm to reconstruct the source direction given the detected count distribution [3].

Modulation by Mask

Assuming a point source in the far field, the gamma rays incident on the mask are essentially parallel. Depending on the source angle relative to the detector, these gamma rays will pass through a specific region of the mask called the 'working zone'. Since gamma rays are either attenuated by closed pixels or allowed through open pixels, the resultant count distribution is a projection of the pattern of the working zone on the detector plane. In the ideal case, each working zone has a distinct pattern, where no two source directions result in the same count distribution. The quality of the mask pattern will determine the signal-to-ratio (SNR) of the image.

Only source directions where the source is either fully or partially modulated by the mask can be considered for reconstruction. This range of source directions is called the field of view (FOV). The range of angles where the flux is completely modulated by the mask is called the fully coded field of view (FCFV). The directions where only part of the flux passes through the coded mask make up the partially coded field of view (PCFV). Unmodulated sources that are recorded by the detector contribute to the background of the image.
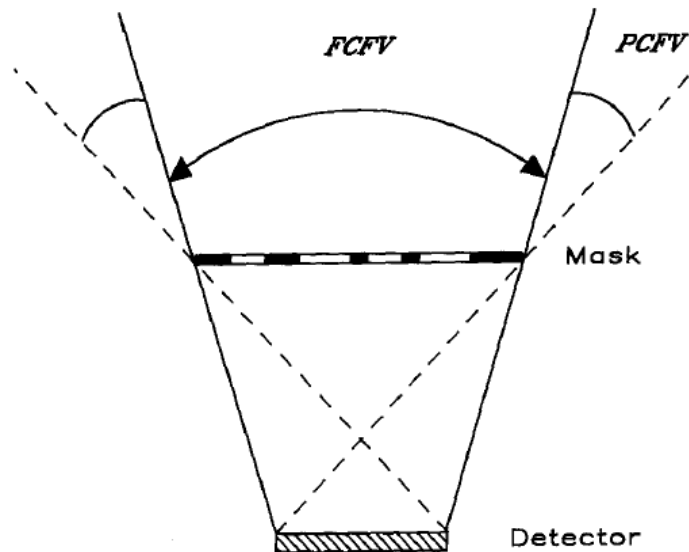
Figure 3.3: Source directions where gamma rays are partially or fully modulated by the coded mask. These regions are known as the partially coded field of view (PCFV) and fully coded field of view (FCFV), respectively [3].

If multiple sources are present in the FOV, each source is modulated by a different working zone. Also, the recorded count rate in each pixel in the detection plane is the sum of the contributions from each source. Figure 3.4 visualizes the contribution of counts from two sources, one on axis, and the second near the edge of the FOV.
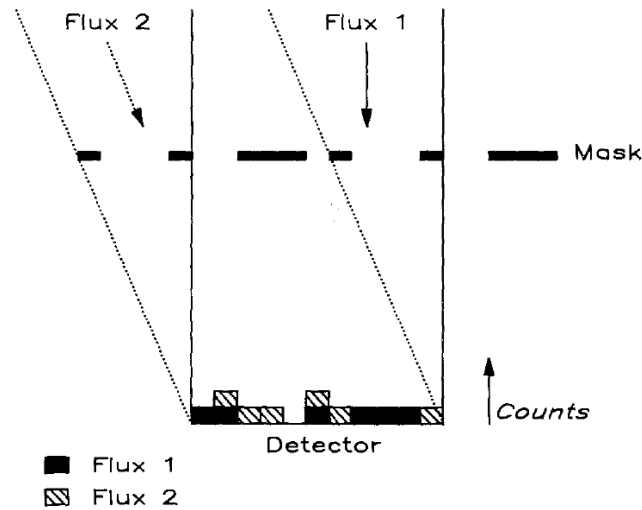
Figure 3.4: Contribution of counts from two sources, one on axis, and the second near the edge of the FOV [3].

Image Reconstruction

Once the count distribution has been recorded on the position-sensitive detector plane, given the relative detector-mask orientation and the mask design, the source direction can be determined using a reconstruction algorithm. The goal is to determine the direction where the mask pattern and detector count distribution match as closely as possible, as this will correspond to the most likely source direction. This is possible due to the fact that for each source direction a unique pattern is projected on the detector plane, as discussed in the preceding section.

In this study, image reconstruction is done using a backprojection method, where for every gamma-ray interaction "event" and every possible source direction, it is determined whether or not the gamma ray could have originated from that direction. This is done by calculating the vector between the detector pixel and image pixel in space, and determining whether or not the mask pixel that the vector passes through is either open or closed. If open, it means that there is a possibility that the gamma ray could have

19

originated from that direction, therefore, a count is added to the image pixel. This is repeated for every image pixel, and then for every gamma-ray event. After summing images of multiple events, a hotspot should form in the image, assuming a point source is present. Essentially, the result is a map that provides the user with best match between the mask pattern and detector count distribution, hence an estimate of the direction of the source.

An optimized mask would result in an image that is flat in all directions except for the source direction, where the result is a peak. However, if the mask is not optimized, there will be partial matches of the mask pattern and detector count distribution that will result in variable artifacts in the image, called sidelobes, which affect the SNR, or quality of the image. The SNR describes how well a source can be picked out from image background, and is especially important when imaging multiple or extended sources in the FOV. It is further described in Appendix C.

3.2 Coded Aperture Mask Design
Mask Patterns

As mentioned in the previous section, using an optimized mask pattern is important to reduce the amplitude and variation of the sidelobes, which contribute to image noise which reduces the image SNR. Studies have been done for over fifty years to mathematically optimize these mask patterns. A brief overview of these patterns will be presented, along with citations for further reference.

As mentioned earlier in this chapter, the concept of CAI is based on the pinhole camera, which consists of a single pinhole in an attenuating material. This configuration provided good angular resolution, with a point spread function (PSF) ideally being a delta function, however, results in very poor sensitivity or efficiency due to the loss of counts to the attenuating material.

One option to improve efficiency is to increase the aperture hole size. This is not a suitable solution, as it inherently worsens the angular resolution. The proposed solution was a mask with many randomly placed pinholes. This way the angular resolution is maintained, and the sensitivity is increased [4][5]. Random patterned masks are utilized in this study.

Unfortunately, when using a random mask, the resultant PSF contains fluctuations in the height or intensity of the sidelobes due to statistical effects. Therefore, a group of optimized mask patterns were designed based on cyclic difference sets to provide a delta-like PSF over uniform and flat sidelobes. This mask pattern is known as uniformly redundant array (URA). URAs were traditionally nearly square in shape [6]; since then patterns that are strongly off-square have been developed [7].

The final mask pattern discussed in this thesis is the modified uniformly redundant array (MURA) [2]. MURAs are square in design and are antisymmetric when rotated 90°. This is especially useful when performing mask/anti-mask measurements. The mask/anti-mask technique is useful to reduce image degradation due to non-uniform background, and unmodulated sources outside of the FOV. Due to its antisymmetry, a simple rotation of the mask allows for the application of this technique. Along with the random mask pattern, MURA masks are used in this study.

Mask Parameters

In addition to the mask pattern itself, specific mask parameters must be optimized for the system to which it will be applied, and for the specific applications that it will be used for. These parameters include mask element size, number of elements, and the mask–detector separation.

The mask element dimensions will affect both the angular resolution of the constructed image and the fraction of attenuated gamma rays as a function of energy. Usually, the element size is on the order of the detector pixel size. Simulations have been performed suggesting that the optimal size is between 1 and 2 times the detector pixel size [8]. The mask element thickness will affect the range of gamma-ray energies that can be used for CAI. In the case of 3D CdZnTe, gamma-rays of energies that result in single-interaction events should be fully attenuated by the mask element, while gamma rays within the energy range that would more likely Compton scatter in the detector should be allowed through for dual modality imaging. Once the mask element size is fixed, the number of elements is selected, which affects the total size of the mask.

Field of View vs. Angular Resolution

After the mask pattern and mask element size are selected, an additional factor must be considered, that is the mask–detector separation. There is a direct tradeoff between two important parameters: FOV and angular resolution. Angular resolution is defined as:

$$\theta \sim D/L \qquad (3.1),$$

where D is the mask element size, and L is the mask – detector separation.

Ideally, the mask would be placed very close to the detectors, reducing the overall size of the system. This configuration results in compact size and large FOV, but poor angular resolution. On the other hand, if the mask is placed at a distance, the angular resolution will improve, however, the compactness and FOV will worsen. Therefore, it is important that these parameters are considered when determining the mask-detector separation distance.

3.3 CAI using 3D CdZnTe

Generally, CAI is applied to 2D position sensitive radiation detection systems. In the case of 3D position sensitivity, the third dimension, or depth of interaction, provides additional information that can potentially improve the quality (precision and accuracy) of the reconstructed image. Major improvement being the reduction of parallax effect, due to more accurate backprojection of events.   3D position sensitivity also allows for the application of multiple masks to a single detector crystal resulting in near 4-pi imaging, which will be discussed in the next chapter.

Coded aperture masks have been applied to the cathode side of thin 3D position sensitive CdZnTe detectors [9]. There are many benefits, as well as challenges, when using thick, large volume 3D position sensitive CdZnTe detectors.   Some of these unique challenges were faced during the course of this study. Issues include material properties, such as non-uniform electric fields, as well as readout settings, which need to be addressed to maintain or improve the quality of the coded aperture images. This thesis is a first attempt to apply multiple coded aperture masks to a single crystal, as well a single mask to

an array of crystals to extend the range of gamma-ray imaging to lower energies using thick, large volume 3D position sensitive CdZnTe detectors.

3.4 References

[1]   "Pinhole Camera." *Wikipedia*. Wikimedia Foundation, 24 Mar. 2014. Web. 2 Apr. 2014.

[2]   S. R. Gottesman and E. E. Fenimore, "New family of binary arrays for coded aperture imaging," *Applied Optics*. 28.4344-4352 (1989).

[3]   Caroli, E., J.B. Stephen, G. Cocco, L. Natalucci, and A. Spizzichino. "Coded Aperture Imaging in X- and Gamma-ray Astronomy." *Space Science Reviews*. 45.3-4 (1987).

[4]   Dicke, R. H. "Scatter-Hole cameras for X-rays and Gamma Rays." *Astrophysical Journal.*153.L101. (1968).

[5]   Ables, J. G. "Fourier transform photography: a new method for X-ray astronomy."*Proceedings of the Astronomical Society of Australia.*1.172. (1968).

[6]   E. E. Fenimore and T. M. Cannon, "Coded aperture imaging with uniformly redundant arrays." *Applied Optics.*17.3.337-347 (1978).

[7]   Busboom, A., H. Elders-Boll, and H. D. Schotten. "Uniformly Redundant Arrays." *Experimental Astronomy*. 8.2.97-123*. (1998).

[8]   I. D. Jupp, K. Byard, A. J. Dean. "An improved sampling configuration for a coded aperture telescope." *Nuclear Instruments and Methods in Physics Research* (1994).

[9]   Grindlay, J. E., W. W. Craig, N. A. Gehrels, F. A. Harrison, and J. Hong. "X-Ray and Gamma-Ray Telescopes and Instruments for Astronomy" *Proc. SPIE* (2003).

PART II
NEAR 4-PI CODED APERTURE IMAGING USING 3D CdZnTe

CHAPTER 4
SIMULATED DEMONSTRATION OF NEAR 4-PI CAI

Investigation of the feasibility of applying CAI to thick, large-volume pixelated CdZnTe began with a single crystal. Initial concerns were that both high (>200 keV) and low energy (<200 keV) gamma-ray imaging efficiency would be significantly reduced due to the 50% opacity of the mask. MCNP5 simulations were run to determine the gamma-ray losses at the various energies. The conclusion was that the losses are minimal at Compton imaging energies and the attenuation of low-energy gammas would be acceptable given the additional directional information.

Although there is a significant reduction of low energy gamma rays and partial reduction of higher energy gammas, since other techniques, such as the centroid method [1] does not provide adequate angular resolution or the ability to distinguish multiple source locations on par with Compton Imaging; coded aperture imaging was the only viable option.

Coded aperture imaging has been done before using thin 3D position sensitive detectors [2]. The use of thicker detectors allows for greater capture of gamma rays. However, due to inherent properties of CdZnTe materials, there are non-uniformities in the response, which are perhaps worse than other gamma ray detection materials.

3D position sensitivity improves imaging in two ways. The first is that due to 3D pixelation, a single detector can provide not only x-y information, but depth as well. This additional depth information should theoretically improve the accuracy of the coded aperture image. This is due to the fact that during the image reconstruction, the event is backprojected from the 3D interaction position rather than the 2D position. Since CAI is a

binary process (events are backprojected either through an open or closed mask element), a slight deviation from actual interaction position will greatly affect the image quality.

The second benefit of 3D position sensitivity is the possibility of adding multiple masks to a single detector. Other systems have shown multiple masks to a multi-detector system. However, applying multiple masks to a single detector is a novel application that is investigated in this study.

This chapter addresses the feasibility of using CAI to image low energy gamma rays with a single CdZnTe detector crystal. Low-energy gamma rays tend to interact near the surface of the detector. Due to the anode dead layer as described in Chapter 2 and the presence of the readout electronics, it is not feasible to place a coded aperture mask in front of the anode surface and form an image of low energy gamma-ray sources, as most of the interactions for a low energy gamma-ray source would occur within the approximately 2 mm anode dead layer that is observed in the readout system when irradiated with 122 keV gamma rays [3].

Image reconstruction was first done on simulated data to verify the practicality of adding a coded aperture mask to a single detector. First, a mask was designed to match the characteristics of the 3D position sensitive CdZnTe detectors, an image reconstruction algorithm was developed to handle the mask-detector geometry, and all this was simulated in MCNP5. This section focuses on the feasibility study and the steps involved. The work is based on the material from [4].

4.1 Mask Design Generator

As mentioned in Chapter 3, coded aperture mask element size is ultimately limited by the position resolution of the detector. Unless the detector readout is pixelated or otherwise spatially segmented, the position resolution is equivalent to the size of each detector element. However, with 3D position sensitive CdZnTe detectors, the position resolution is determined by the readout electronics, which in this case is equivalent to the pixel pitch of 1.72 mm × 1.72 mm.

The first step is to design random and MURA mask patterns to be applied to the 3D CdZnTe. A code was developed in C++ to generate random and MURA masks of various sizes. The random mask is developed using a random number generator, assigning either a

1 or 0 to the position, representing either an open or closed pixel. MURA masks are developed using an algorithm shown in Appendix A. Figure 4.1 shows an example 14 × 14 random mask, and Figure 4.2 shows a 5 × 5 MURA mask array in a 2 × 2 mosaic.
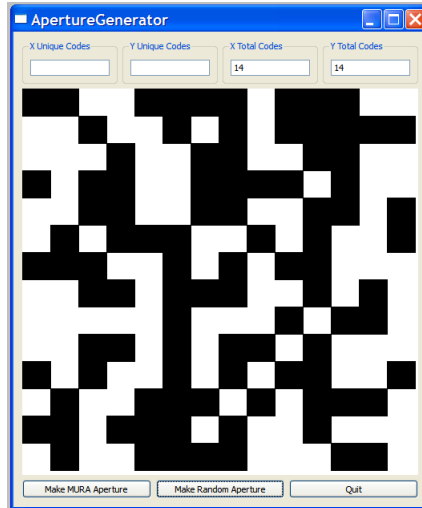
Figure 4.1: An example of a 14 × 14 random array
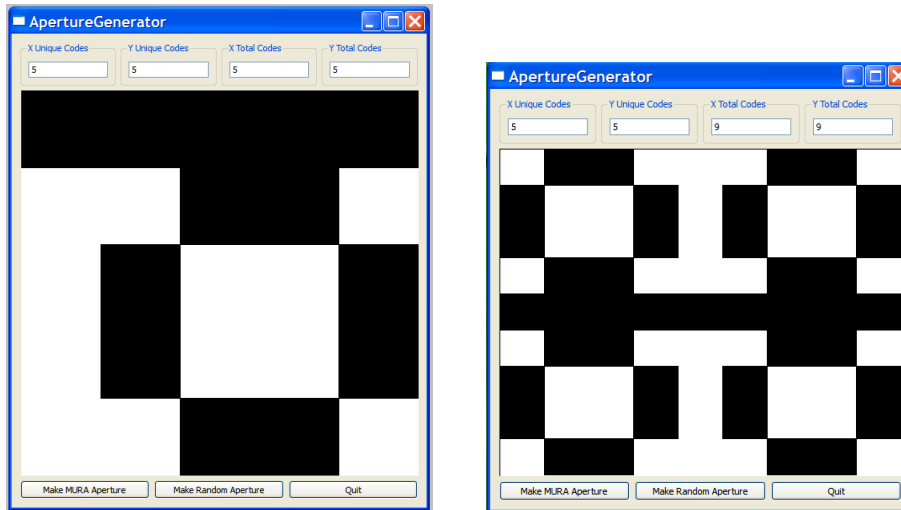
Figure 4.2: 5 × 5 MURA array (left), and a 5 × 5 MURA array in a 2× 2 mosaic (right).

This aperture generating code is used to generate a variety of patterns that were used throughout the investigations presented in this thesis.

4.2 Image Reconstruction Code

A MATLAB code was developed to reconstruct coded aperture images given a hardcoded geometry, which includes the detector and mask orientation in space. The pseudocode for this backprojection reconstruction algorithm can be viewed in Appendix B. The idea behind the algorithm is that for every full-energy (or photopeak) gamma-ray interaction in the detector, the event is backprojected to every image pixel in imaging space. The vector that is created by connecting these two points in space passes through the mask plane. Whether or not the vector passes through an open or closed pixel affects the contribution of the event to the image pixel. If the mask element is opened, the event is considered, otherwise it is ignored. To improve the image reconstruction, a sensitivity image is used to correct for the varying efficiency in each direction following the principles described in [5] This is the event-by-event equivalent of the deconvolution as described in Chapter 3, which is necessary for real-time CAI.

Coded aperture imaging has been performed with 2D position sensitive detectors for over forty years. For each image direction, later referred to as an image pixel, the counts that correspond to open mask pixels are added to the image tally, while the counts from closed mask pixels are subtracted. The image pixel of maximum intensity represents the direction of a source. The 2D technique can be extended to a 3D position sensitive detector for one mask projecting the mask to each depth of the detector for each image direction. With multiple masks, the cross-talk between masks must be corrected. This is done by weighting events depending on the probability that they originated from each mask.

The backprojection method involves the calculation of a vector from the center of each detector voxel to the center of each image pixel. The gamma event contribution depends on whether the mask element the vector passes through is closed or open (0 or 1, respectively). The result using this technique is a very course image mesh. In the case that a hotspot straddles two image pixels, it would be ideal to increase the size of the image mesh to provide a more detailed image.

A novel technique was developed to artificially increase the number of image bins. Rather than forming a vector between detector pixel and image pixel and then determining whether or not the vector intersects an open or closed mask element, the entire detector pixel area is projected up to the mask plane in the direction of the image pixel. The proper

27

projection of the entire pixel area, rather than to and from a single, improves the angular resolution of the image.

The weight of the contribution of each event in the image is based on the fraction of the detector pixel area that overlaps the open mask element. Rather than a discrete contribution of 0 or 1, a relative contribution (between 0 and 1) is calculated based on the fractional open area. This is repeated for each gamma-ray event in the detector until a hotspot representing the source can be clearly identified.

4.3 Simulations in MCNP5

Before investing the time and resources into building a CAI imaging system, a sample geometry, including detector, coded mask, and point source were simulated in MCNP5. Using the PTRAC output file, gamma-ray interaction position information and energy deposition information is provided. This information can be blurred to create a more realistic representation of the system. The position resolution is limited by the known pixel pitch and depth uncertainty, 1.72 mm and 1.36 mm, in this case, and energy deposition is Gaussian blurred to match the measured energy resolution of single-pixel events.

Geometry

A $2 \times 2 \times 1.5$ cm^3 CdZnTe detector is simulated in space, as shown in Figure 4.3. Both random and MURA masks are simulated for the sake of comparison. In each case, a 21×21 element mask is applied to the side of the detector, each mask element is designed to match the 1.73mm pitch of the 11×11 array of detector pixels. The simulated mask design is shown in Figure 4.4
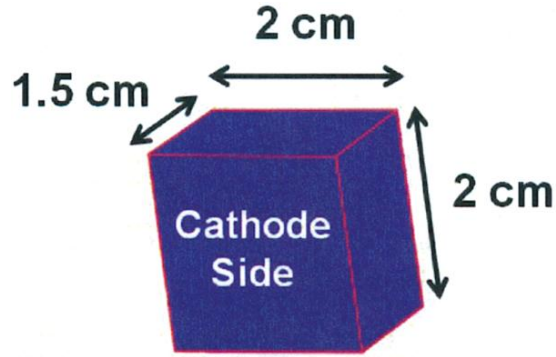
Figure 4.3: 2 × 2 × 1.5 cm³ CdZnTe detector simulated in MCNP5
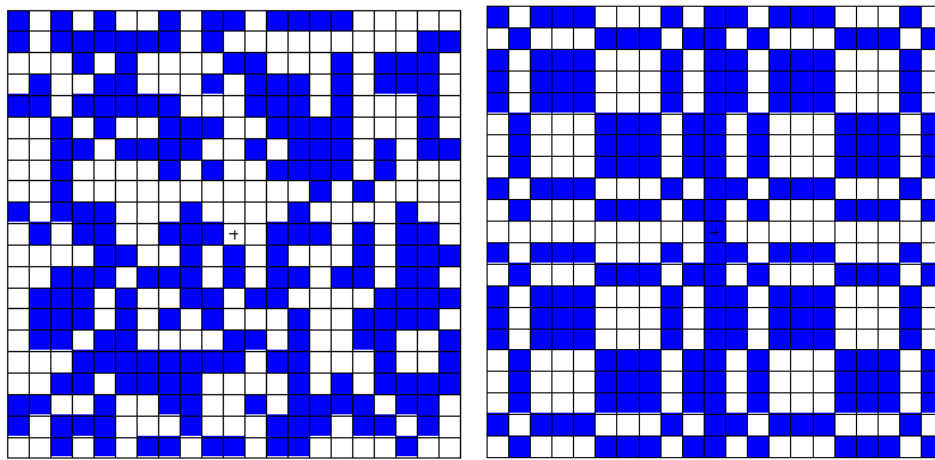
Figure 4.4: 21 × 21 element random mask (left), and MURA mask (right). The darkened regions represent the closed mask elements.

Since the purpose of the system is to act as a multimodal imager, the mask material and thickness must be selected to attenuate most low-energy gamma rays for CAI and allow mid to high energy gamma rays to pass through with minimal attenuation for Compton imaging. The attenuating properties of various thicknesses of tungsten were calculated as a function of photon energy.

$$I = I_0 e^{-\mu x} \tag{4.1}$$

where

I = intensity of photos after being transmitted through material thickness x [gammas cm^{-2} s^{-1}]

I_0 = initially intensity of photos [gammas cm^{-2} s^{-1}]

μ = linear attenuation coefficient [cm^{-1}]

x = material thickness [cm]

The linear attenuation coefficient is a function of elemental composition and density of the material, as well as gamma-ray energy. The tabulated data of mass attenuation coefficients (μ/ρ) for elements or compounds can be calculated on the NIST website [6]. This data was used to generate Figure 4.5 and Table 4.1 to select a suitable mask element thickness.
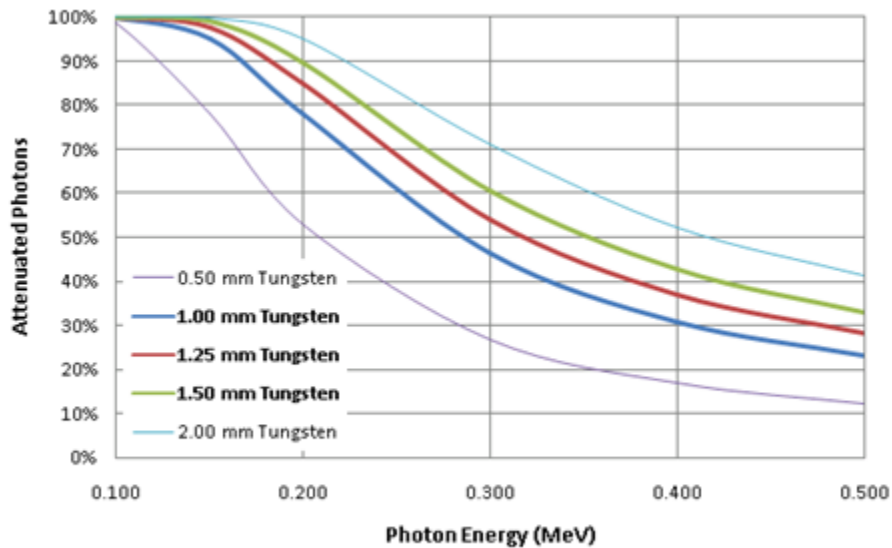
Figure 4.5: Percent attenuated gamma rays as a function of energy and mask thickness [6].

A fractional attenuation close to 100% is ideal for low energy gamma rays, when the only practical imaging modality is CAI; this region is below 200 keV in CdZnTe. For gamma-ray energies in the 200 to 300 keV range, both CAI and Compton imaging modalities are utilized, for photoelectric and Compton events, respectively. As gamma-ray energy increases above 300 keV, attenuation should be minimized as the transition is made toward the Compton imaging modality. From Table 4.1 one can see that an element thickness of 1 mm attenuates over 99% of the low energy gammas and allows most of the

higher energy gammas to pass through. Therefore, a thickness of 1 mm was selected for simulations, and later for measurements.

Table 4.1: Fractional attenuation (I/I_0) of gamma rays using tungsten mask elements

Thickness (mm)	Energy (keV)		
	122	276	356
0.5	92.4%	30.8%	20.2%
1	99.4%	52.2%	36.4%
2	100.0%	77.1%	59.5%

The mask is placed at a distance of 0.75 cm from the surface of the detector, resulting in an angular resolution of 13°. This distance is selected to accommodate the other four masks that will later be placed on the other sides of the detector.

Source

Since CAI is to be used to image gamma-ray sources below about 300 keV, and Co-57 is a check source that will often be used for measurements in the lab, and point source emitting 122 keV gamma rays isotropically was simulated. The source is placed 5 m from the detector to represent a far-field, parallel source.

4.4 Simulation Results

Both single-mask imaging and multi-mask imaging is simulated. In the single-mask scenario, a mask is placed on the cathode side of the detector. In multi-mask imaging, five masks are applied to the detector, on all sides except the anode side, which suffers from a few millimeter dead-layer due to weighting potential affects as described in Chapter 2.

Single-Mask Imaging

In single side imaging, a single mask is applied to the cathode side of the detector. The 122 keV isotropic gamma-ray source is placed 5 m from the detector surface. After

applying both energy and position blurring, the CAI algorithm is used the reconstruct the image as shown in Figure 4.6.
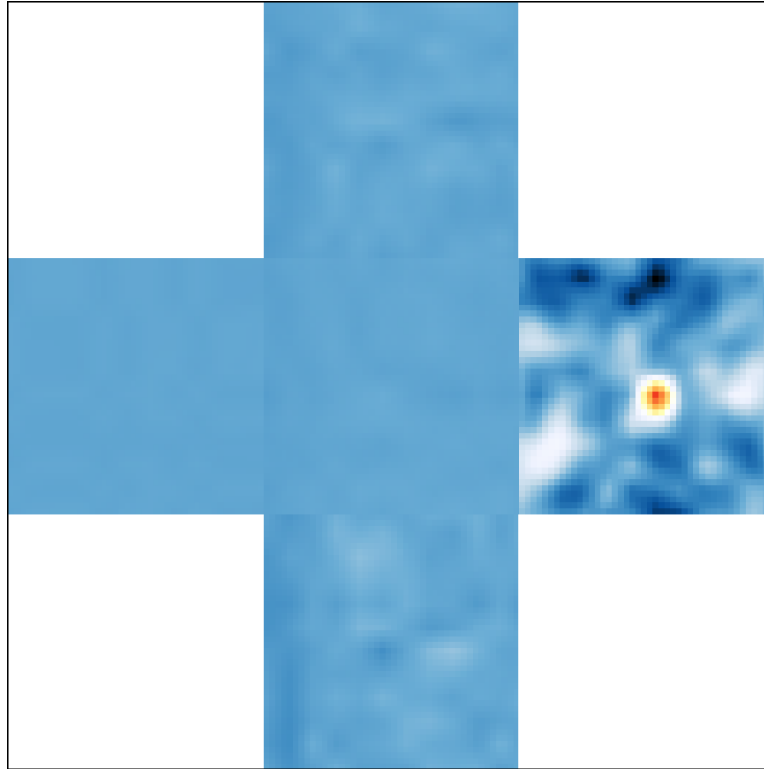
Figure 4.6: Cathode side coded aperture imaging: 122 keV point source located at a distance of 5 m from the detector surface. Each square represents the reconstructed image through one of the five surfaces of the detector.

Figure 4.7 shows the improvement in image quality when oversampling the image bins, a technique described in the image reconstruction section earlier in this chapter. The upper image shows the traditional pixel-to-pixel backprojection, compared to the bottom images, that by using the technique, have an increased number of image pixels, by two and three times, respectively. The result is an oversampling of the image bins, greatly improving the angular resolution of the image. This is repeated for a 186 keV source and provided similar improvements.
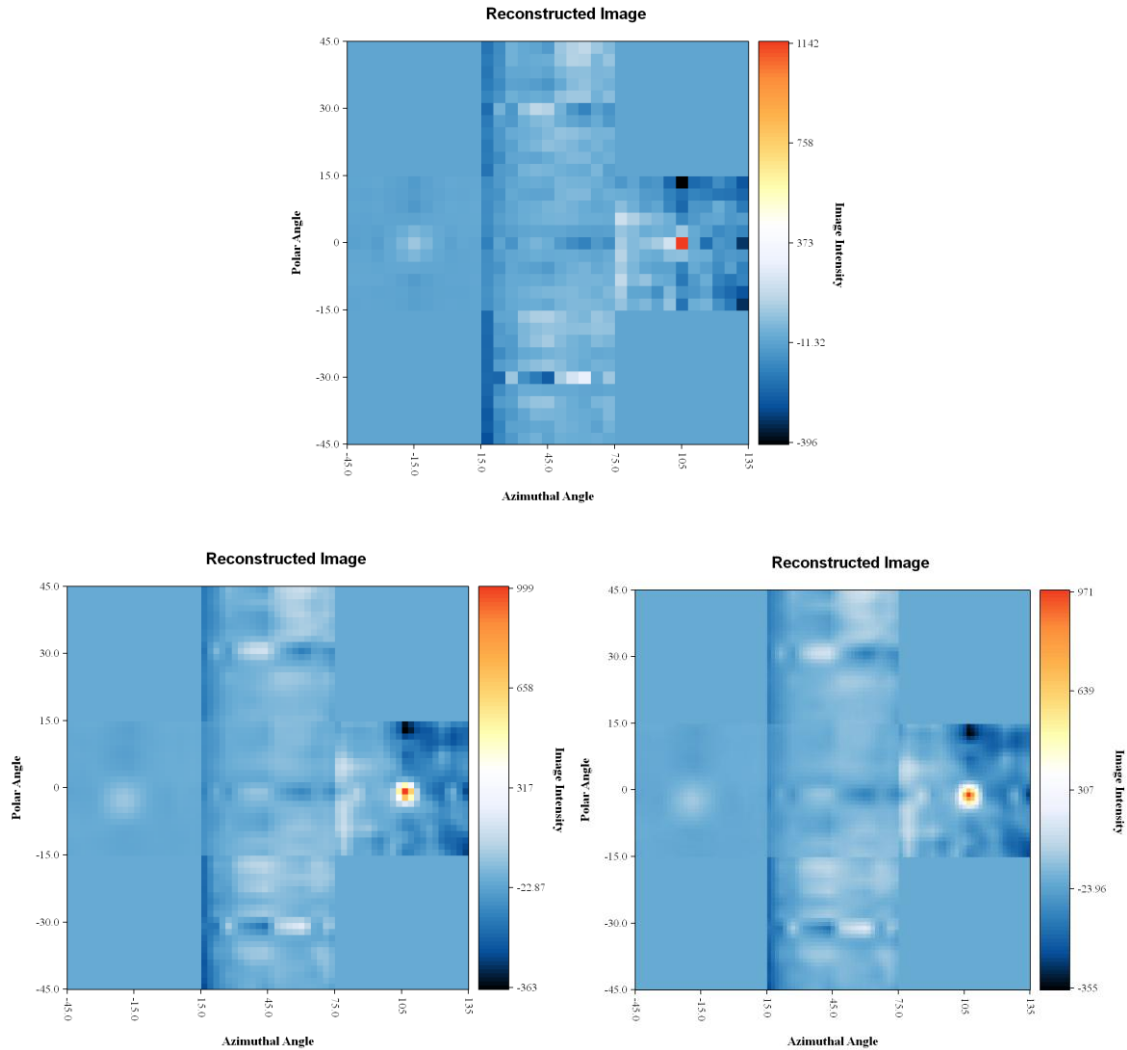
Figure 4.7: Improvement in angular resolution due to 1x (upper), 2x (bottom left), and 3x (bottom right) the number of image pixels, when imaging a simulated 122 keV gamma-ray source at 1 m from the detector surface.

When comparing CAI to the bare-detector technique known as the centroid method, there is a significant improvement in both the accuracy and precision. The accuracy of the CAI method is estimated for both scenarios in MCNP5. In the bare detector scenario, 20,000 gamma-ray events were simulated. These events were broken into 100 data sets, 200 events each. Using the centroid method algorithm described in Chapter 2, the source direction is estimated for each dataset. While the general source direction is determined, there is some fluctuation, as shown in Figure 4.8 (top). These images are compared to the coded aperture images, each containing 100 events (half that used in the bare detector scenario) to reflect the fact that approximately half of the gamma rays would be absorbed

by closed mask elements. In the CAI scenario, 100 of 100 measurements correctly identified the source direction. The directional uncertainty (how accurately the source direction is estimated) improved from 30° to 13°.
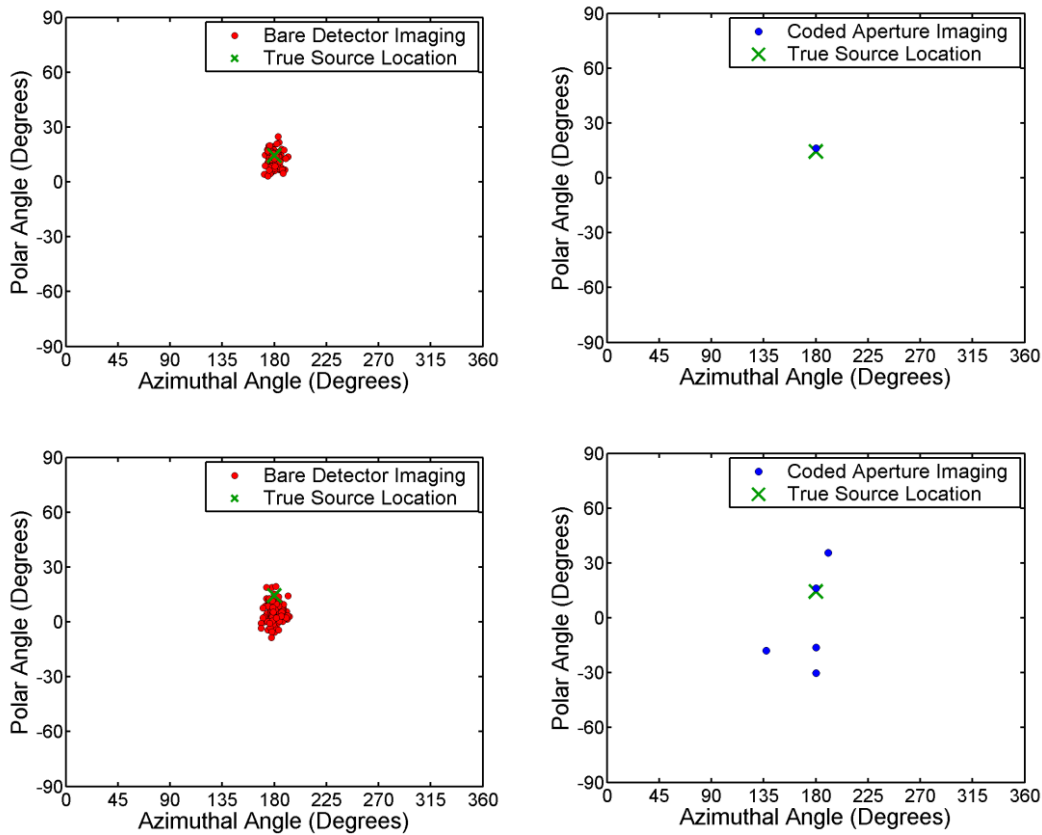
Figure 4.8: A comparison of bare detector (left) and coded aperture imaging (right), without background, the coded aperture imaging technique correctly identifies the source direction 100 of 100 times (top), with background, the coded aperture imaging technique correctly identifies the source direction 95 of 100 times (bottom).

This was repeated with an additional 200 background counts in the bare case and 100 background counts in the CAI case shown in Figure 4.8 (bottom). In the bare detector case, the centroid of the distribution shifts down towards to the equator away from the true source direction. However, in the CAI case, 95 of the 100 datasets are correctly reconstructed to the true source direction. This proves that the determination of the source direction is more precise with CAI even when considering the efficiency loss of half of the counts due to mask attenuation.

Multi-Mask Imaging

The field of view (FOV) for Compton imaging is 4-pi space; in order to match this imaging capability at lower energies it is necessary to image in all directions. 3D position sensitivity allows for the application of multiple masks to a single detector, as shown in Figure 4.9.
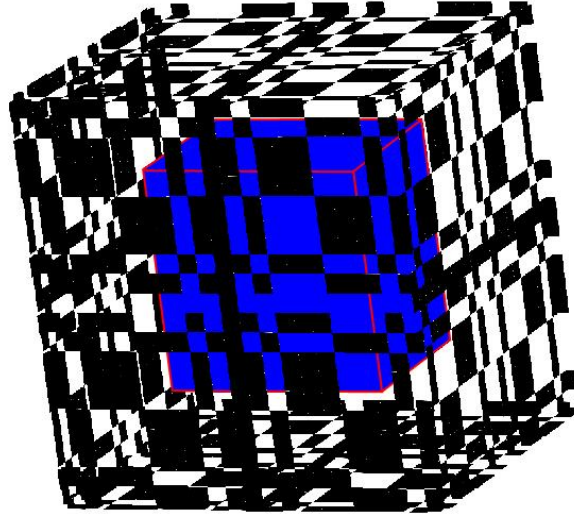
Figure 4.9: Simulated geometry of the mask-detector system in MCNP5. A MURA mask is applied to each side of the detector except the anode side, which has limited imaging capability at low energies due to the anode dead layer.

The CAI algorithm must be altered when considering multiple masks. The main challenge is to determine which mask each gamma-ray passes through. A novel technique to deterministically calculate the probability of an event arriving from each mask is as follows:

$$W_{i,M} = \frac{\exp[-\mu x_{i \to M}]T_M}{\sum_{k=1}^{5}(exp[-\mu x_{i \to k}]T)_k} \tag{4.2},$$

where

W = weight assigned to each mask

i = event in the detector

M = mask of interest

x = distance from event to the surface

T = total counts on the surface

μ = detector linear attenuation coefficient

For each event, *i*, a weighting factor is assigned to each mask, *M*. This factor is based on the attenuation pathlength from the interaction position to the surface of the mask, normalized by the total counts on the surface, divided by the sum of this value over all masks. The principle behind this technique is best illustrated when considering an event that is observed in the center of the detector, 10 mm from each imaging surface. In the absence of any other observations there is an equal probability that this event passed through each mask. However, if many more gamma-rays are observed and they are generally appear close to one side, then it is more likely that the gamma ray detected in the center of the detector came from the same side as all the others. The technique described above takes the information gathered from all observations and uses this to assign the probability of passing through each mask to individual gamma-ray interactions.

For the mult-mask case, the simulation involving a single 122 keV gamma ray point source is repeated; however, this time the polar angle is incrementally varied from 0° from the +x mask to 90° polar angle associated with the +z mask. Figure 4.10 shows the various images associated with these source positions. One can imagine an unfolded box, where each tab represents one of the five masks surrounding the detector. Notice that the source is located on the edge of the +x and +z mask in the middle right image.
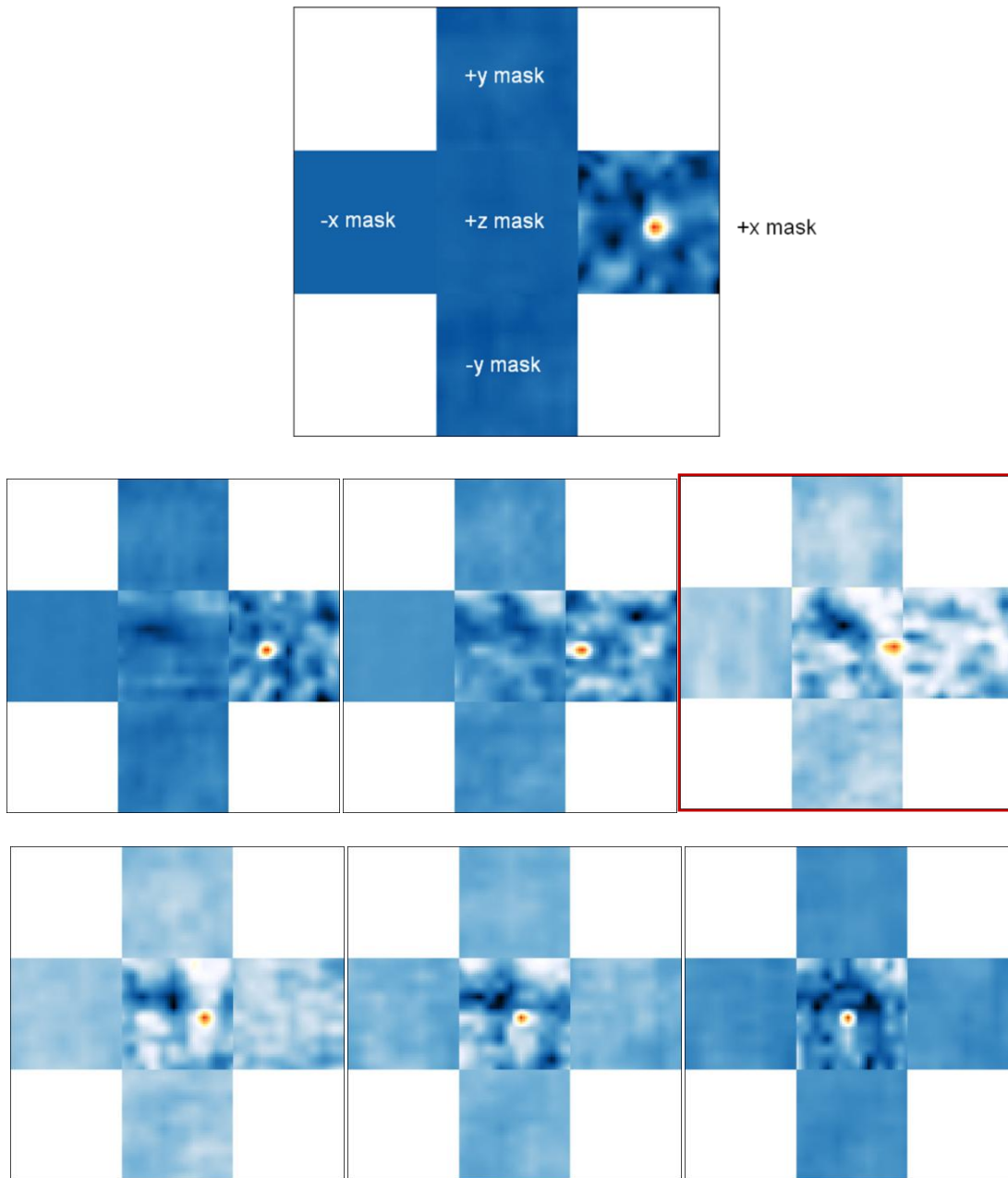
Figure 4.10: Simulated 122 keV gamma ray source positions at various polar angles 0°, 15°, 30°, 45°, 60°, 75°, 90°. Notice how the source straddles two masks in the image highlighted by the red border.

To verify the robustness of this technique and to ensure that it would work with multiple point sources over background, a scenario of multiple weak sources above background is imaged. Three weak sources are simulated in MCNP5. These sources are placed on three sides of the detector with a source strength equal to or half of the

background strength. Figure 4.11 portrays the detectability limit of the multi-mask system. The direction of each source is clearly pinpointed using a minimal number of events.
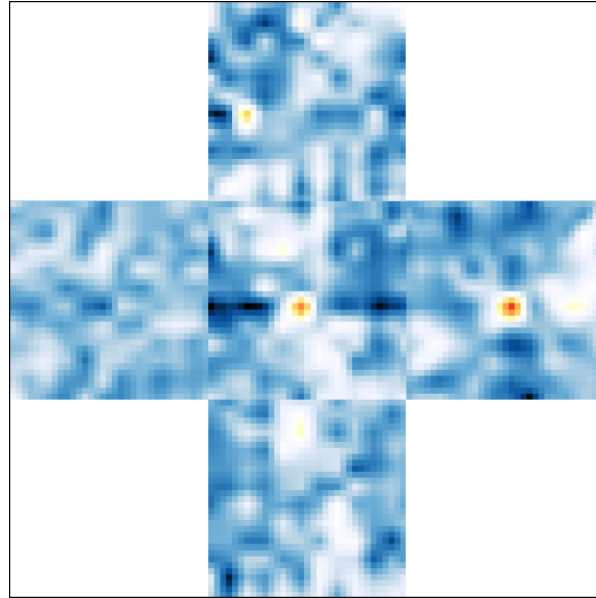
Figure 4.11: Multiple weak sources simulated with a uniform background (200 counts) and imaged using a MURA mask. Source 1 is incident on the +x mask (100 counts), Source 2 is incident on the +y mask (100 counts), and Source 3 is incident on the +z mask (200 counts).

The images created using the simulated data in MCNP5 demonstrated that a coded aperture imaging system using 3D CdZnTe detectors is theoretically feasible, and that it may be worth investing time, money, and resources to extend the current imaging capabilities to lower energies.

4.5 Conclusions

Through Monte Carlo simulations, the feasibility of near 4-pi CAI using 3D position sensitive CdZnTe detectors was verified. Utilizing 3D position sensitivity allows for potential application of multiple masks to a single detector. The reconstructed images provide good angular resolution. Image reconstruction algorithms were developed to consider depth of interaction, as well as the application of multiple masks. The next chapter focuses on experimentally demonstrating near 4-pi coded aperture imaging using a single and multi-detector system.

4.6   References

[1]   Kaye, W. R., N. D. Bennet, C. G. Wahl, Z. He, and W. Wang. "Gamma-Ray Source Location by Attenuation Measurements." *IEEE Nuclear Science Symposium Conference Record,* (2007).

[2]   Grindlay, J. E., W. W. Craig, N. A. Gehrels, F. A. Harrison, and J. Hong. "X-Ray and Gamma-Ray Telescopes and Instruments for Astronomy"*Proc. SPIE* (2003).

[3]   Kaye, W. R., "Energy and Position Reconstruction in Pixelated CdZnTe Detectors," Ph.D. Thesis, University of Michigan, 2012.

[4]   Joshi Kaye, Sonal; Kaye, Willy R.; He, Zhong, "4-pi coded aperture imaging using 3d position-sensitive CdZnTe detectors," Nuclear Science Symposium Conference Record, 2008. NSS '08. IEEE , vol., no., pp.711-713, 19-25 Oct. 2008.

[5]   Xu, D., "Gamma-ray imaging and polarization measurement using 3-D position-sensitive CdZnTe detectors," Ph.D.Thesis, University of Michigan, 2006.

[6]   Berger, M. J., J.H. Hubell, S. M. Seltzer, J. Chang, J. S. Coursey, R. Sukumar, D. S. Zucker, and K. Olsen, "XCOM: Photon Cross Section Database," *NIST Standard Reference Database 8 (XGAM)*, 1998.

CHAPTER 5

EXPERIMENTAL DEMONSTRATION OF NEAR 4-PI CAI

5.1 Cathode-Side Imaging

Following the simulated results, the logical step would be to test whether or not coded aperture imaging is applicable to a bench top system. Coded aperture masks were fabricated, and slight modifications were made to the imaging code to incorporate true mask-detector geometry, as well as to handle the data format provided by the data acquisition and calibration code. This chapter describes the process through which coded aperture imaging was experimentally demonstrated with 3D position sensitive CdZnTe. The work is based on the material from [1].

5.1.1 Single-Detector Imaging

To begin, a single mask was applied to a single detector system. The mask was first applied to the cathode side of the detector where the best images were expected to be generated, as the anode side has a dead layer due to weighting potential effects, and the other sides have poorer position resolution.

Mask Design

To allow for easy modification of the mask design, a novel technique was developed where a mask element holder is designed in SolidWorks and printed at the University of Michigan 3D Lab. Tungsten pieces with the dimensions $1.72 \times 1.72 \times 1$ mm^3 were purchased through Midwest Tungsten Service. The first mask designs included a 21×21 random array and 21×21 MURA, as shown in Figure 5.1.
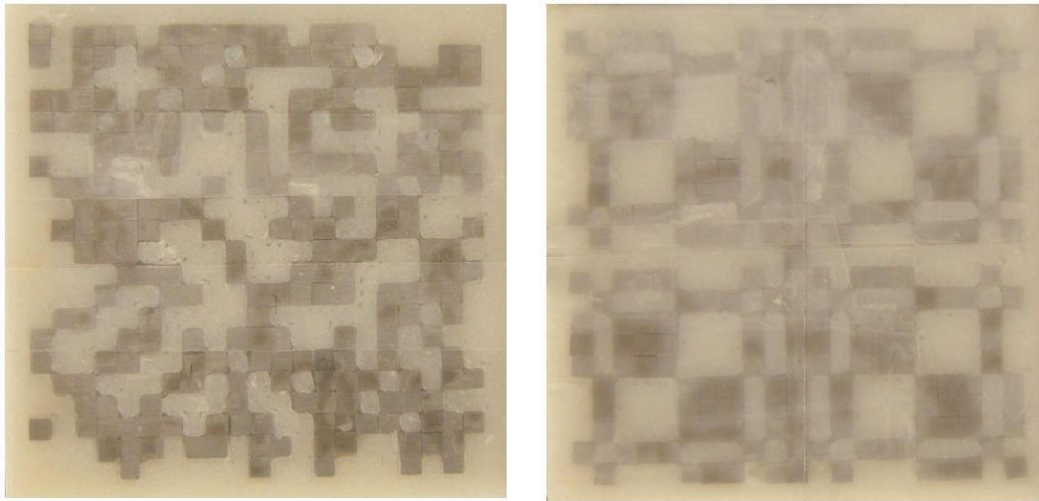
Figure 5.1: Coded aperture mask holders designed in SolidWorks and printed at the UM3D Lab. 21 × 21 random array (left) and MURA (right).

The mask was then aligned with the detector, and mounted on the outside of the detector box. External mounting of the mask allowed for easy application and removal, as the detector systems were shared amongst students in the lab.

Image Reconstruction

The MATLAB code was modified to take into account the actual geometry of the system, including relative detector and mask position, mask design, field of view, as well as the format of the data. The data includes time of event, pixel and depth of interaction, and energy deposited at each position. During this phase of CAI investigation, real-time reconstruction had not yet been implemented. Instead, the data is post processed, first binned by energy of interest and counts in each detector pixel, then processed through the image reconstruction algorithm. An added feature of this version of the code is the ability to image near-field sources in case the source is placed too close to the system relative to the mask-detector separation (distance less than 1 m).

Experimental Setup

In the single-detector case, the detector was oriented such that the cathode side is facing a direction in which a source can easily be placed. The mask was applied to the cathode side of the detector, between the source and detector.
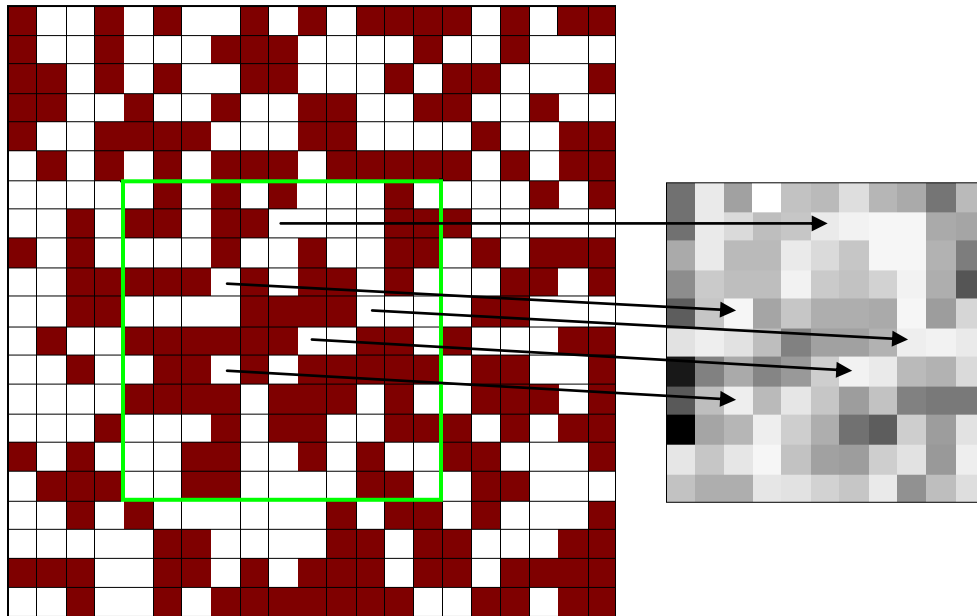
Figure 5.2: The 21 × 21 random pattern (right) compared to the 11 × 11 pixel count distribution (left). The green area is the working zone of the mask. Arrows are used to indicate similarities in mask pattern and detector count distribution.

However, before the mask was applied to the system, the uniformity of the detector was measured by placing a 122 keV source at a distance to simulate a far-field or parallel beam source. The photopeak count rate was measured in each pixel. In an ideal detector, the response would be uniform over all pixels, but from Figure 5.3 a non-uniform response is observed, which has been attributed to a non-uniform electric field due to material defects [2][3]. It is possible that as an electron cloud travels through the detector, rather than traveling straight to the pixel under which the interaction occurred, the path is skewed such that the electron cloud is collected by a neighboring pixel. This skewed path is due to imperfections or impurities (such as tellurium inclusions) in the detector crystal, which affect the electric field. This effect is referred to as "pixel jumping" throughout this work. Pixel jumping will be further discussed in Chapter 6.
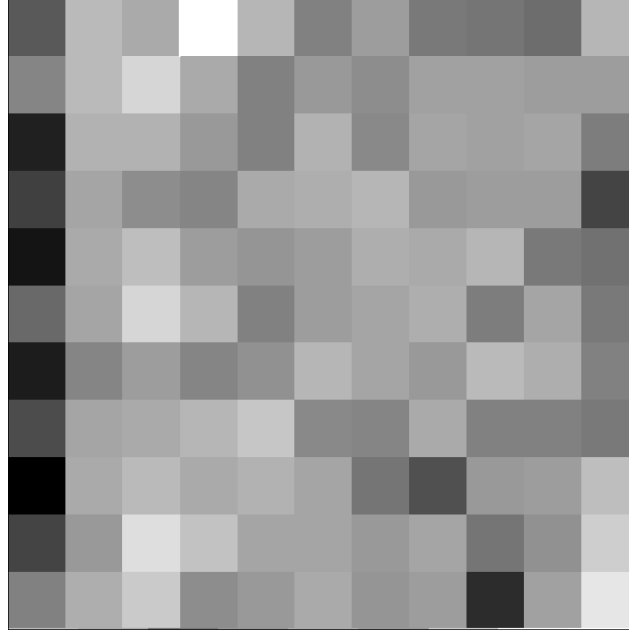
Figure 5.3: The pixel count distribution of a far-field Co-57 source. The expectation is a flat and uniform response. However, this is not the case due to pixel jumping.

After the detector uniformity is measured, a 21 × 21 random mask is placed on the outside of the detector box, which is at a distance of 4 cm from the cathode surface of the detector. To ensure that the mask is centered on the detector such that the mask correctly matches up with the detector pixels, a 122 keV source was placed perpendicular to and centered on the mask. The spectra of each pixel was viewed and adjusted until the shadow of the mask design was accurately recorded by the mask pixels.

Results

Despite the effects of pixel jumping, the image reconstruction code is able to pinpoint the correct location of the source, while using the only inner 9 × 9 pixels. The inner 9 × 9 pixels were used to avoid non-uniform electric field effects of the detector wall. As shown in Figure 5.4, although the hotspot seems to be straddling two image pixels, the most intense pixel corresponds to the correct source direction.
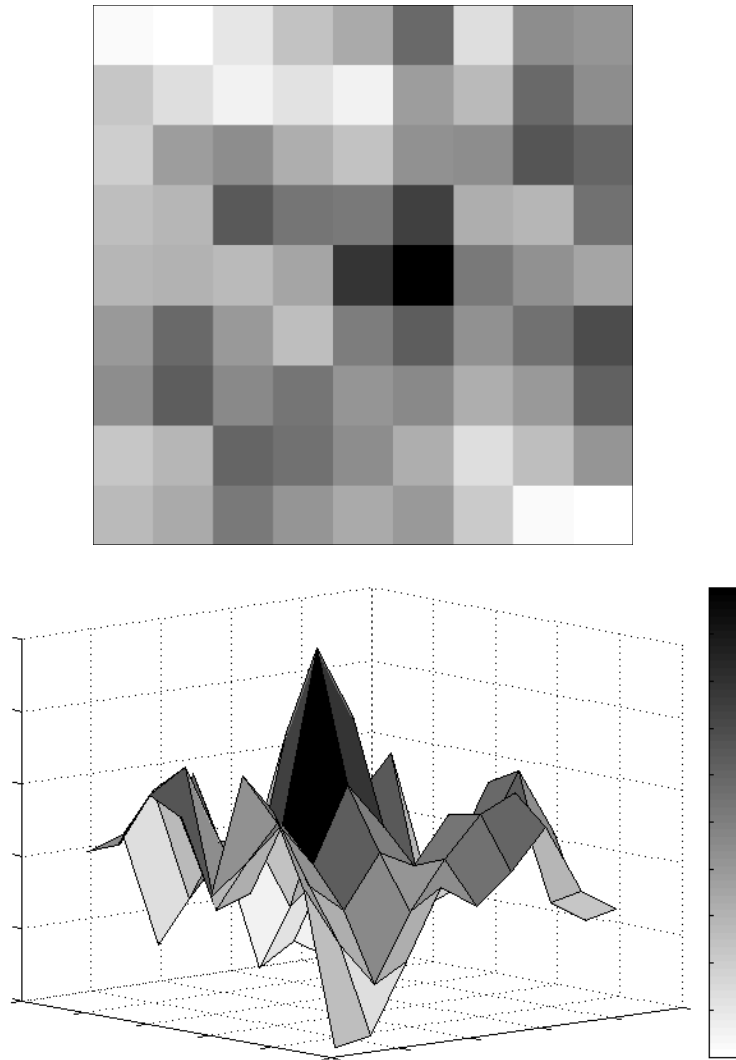
Figure 5.4 First image reconstructed using the single-detector coded aperture imaging system, image view (top), and side view to see relative sidelobe intensities (bottom).

To ensure that the reconstruction of the correct source direction was repeatable, the probability of correctly identifying the source direction is calculated using two different measurement times. In the case where 500 measurements of 100 Co-57 photopeak counts each, the correct direction of the source is located 56% of the time. When the number of counts is increased to 500 photopeak counts per measurement, the source direction is accurately located 98.6% of the time, as shown in Figure 5.5. The measurement shows that given enough photopeak counts and a background rate comparable to the laboratory, imaging is quite reliable.

Figure 5.5 Repeatability of correctly identifying the Co-57 source direction using 500 measurements with 100 counts per measurement (left) compared to 500 counts per measurement (right)

5.1.2 Multi-Detector Imaging

Once single detector coded aperture was demonstrated, the imaging system was extended to multiple detectors. In this case, four detectors formed a 2 × 2 array as shown in Figure 5.6. The detectors all provided a single-pixel interaction energy resolution of 1.5% FWHM at 662 keV or better, with more detailed specifications shown in Figure 5.7. The detector pitch is 22 mm, indicating a 2 mm gap exists between each detector.
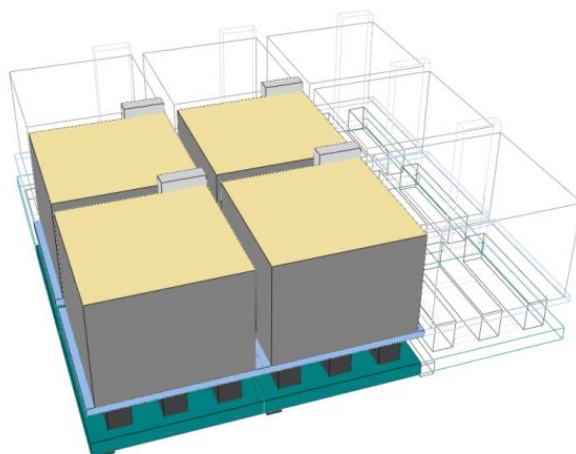
Figure 5.6: Four-detector imaging system relative to the nine-detector CdZnTe detector array

45

Detector #11	Detector #21
4E5 – **eV Products**	**4E10** – **eV Products**
GMI ASIC	GMI ASIC
Energy Resolution **~1.5%**	Energy Resolution **~1.3%**
(1-pixel interaction)	(1-pixel interaction)

Detector #12	Detector #22
4R8 – **Redlen**	**4R2** – **Redlen**
GMI ASIC	GMI ASIC
Energy Resolution **~1%**	Energy Resolution **~1%**
(1-pixel interaction)	(1-pixel interaction)
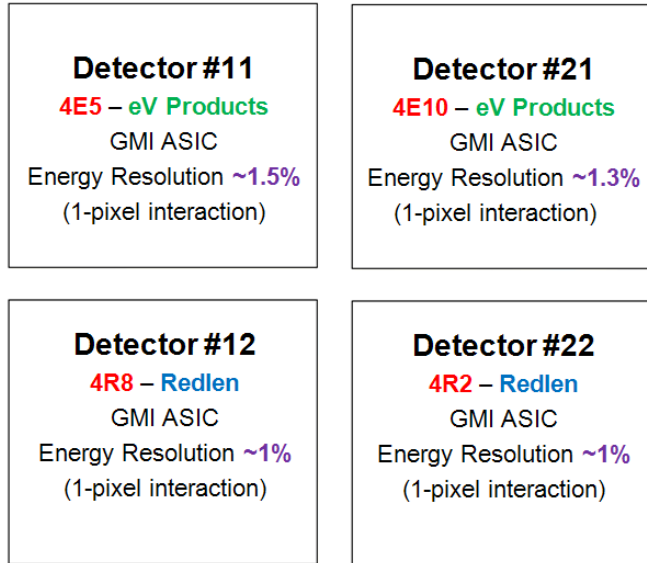
Figure 5.7: CdZnTe crystal details for each detector used in the 2 × 2 array

Mask Design

To reduce the effects of pixel jumping, the mask element size was increased to double the detector pixel dimensions from 1.72 mm × 1.72 mm to 3.44 mm × 3.44 mm. While this does reduce the angular resolution of the image it also reduces the effect of pixel jumping because the image reconstruction becomes less sensitive to the spatial resolution within the CdZnTe which is effectively degraded by pixel jumping. The mask also must be large enough to encompass all four detectors. Since the mask element size was increased, the 21 × 21 random array could still be utilized as it encompassed the entire four-detector array.
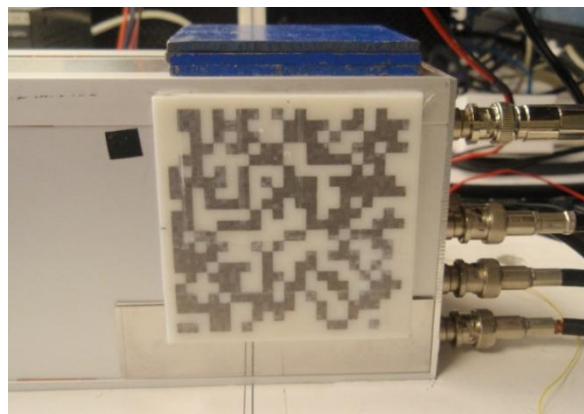
Figure 5.8: 21 × 21 random array centered on a four-detector system, placed 4 cm from the cathode surfaces.

Image Reconstruction

A few changes had to be incorporated in the imaging code when moving from a single detector system to a four-detector array. One is that the relative detector-mask positions must be considered. Then, the images were first reconstructed for each detector individually. Once the relative positions were considered, the images are combined, resulting in the final image. The images can simply be added together, representing a single pixelated detector array with voids in the place of the gaps between detectors.

Experimental Setup

Similar to the single detector case, a Co-57 source emitting 122 keV gammas is positioned 20 cm from the mask. Again, near-field effects must be considered as the source is very close to the system relative to the mask-detector geometry. The source is incrementally moved from one edge of the field of view to the other, spanning approximately 60°. Each measurement consisted of at least 1000 counts per detector.

Results

The image of each source position is created using 1000 counts in each detector. Individual detector images are reconstructed and combined. The point source can be tracked in the coded aperture image as it moves across the field of view. However, the artifacts are much more prominent than expected, based on the simulated results, which could ultimately lead to misidentification of source positions, as shown in Figure 5.9. To better understand why the measured data provides such noisy results, it was necessary to examine the images formed by each individual detector.

The counts from each detector code are processed individually, and the image is displayed before summation. From the individual images, only one of the four detectors forms a clear image of the source direction, shown in Figure 5.10.
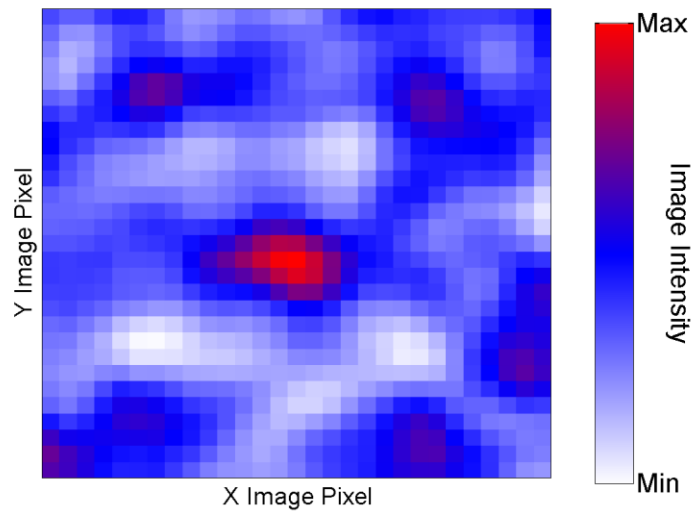
Figure 5.9: Image formed by a four-detector array with the source is placed in the center of the field of view. The sidelobes are much more prominent than expected from simulation.
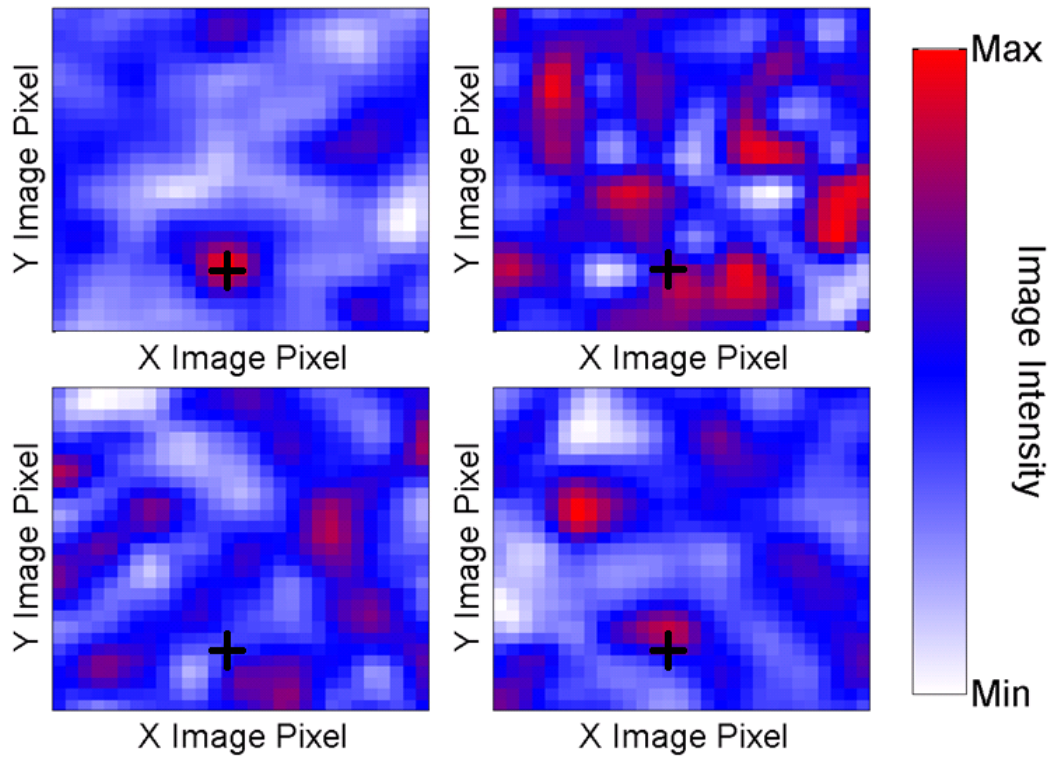
Figure 5.10: Individual images formed using measured Co-57 data from the four-detector array. Note that the placement of each detector's image is the same as shown in Figure 5.7.

A simple experiment was conducted to better understand the characteristics of each individual detector. The four detectors were irradiated uniformly from the cathode side with a near-parallel Cs-137 beam without an aperture mask. In an ideal case, the same count rate should be observed in each pixel. However, as shown in Figure 5.11, severe non-uniformities in the count rate are observed in all detectors, except the one that provided the smooth image. This is surprising, as this detector has the most severe trapping (~5%) and worst energy resolution (~1.5% FWHM at 662 keV) of the four detectors.
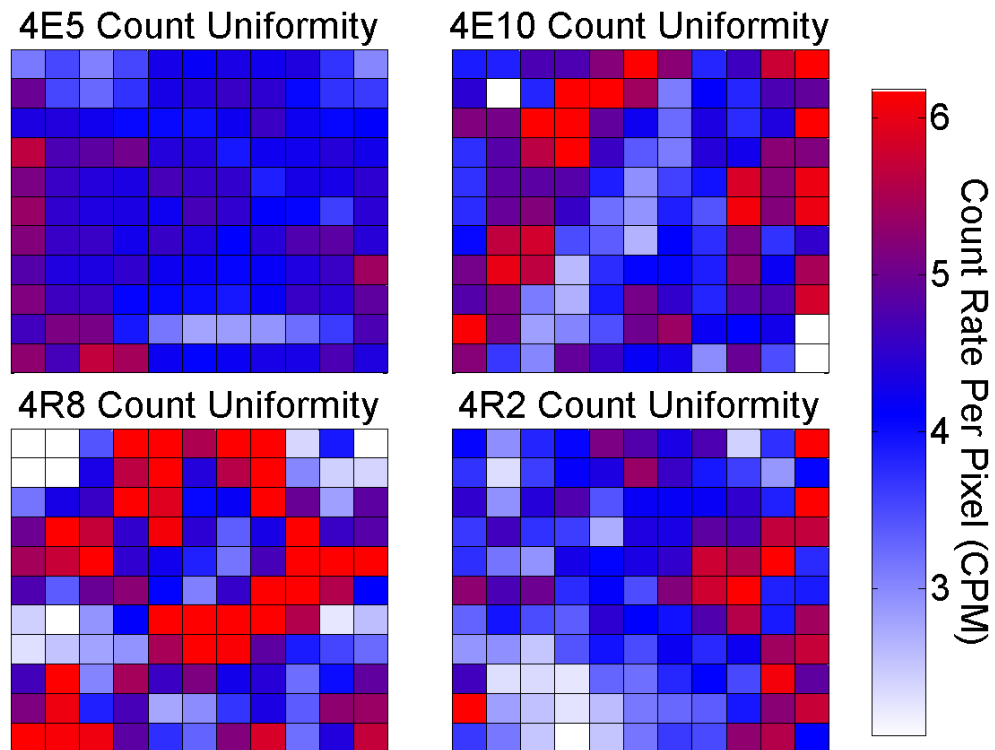
Figure 5.11: The count rate in each pixel of the four-detector array under uniform Cs-137 irradiation without an aperture mask.

Although the non-uniformity may be a result of count loss, perhaps due to the properties of the side surfaces of the detector of the anode dead layer, it is believed that some of the non-uniformity is actually due to pixel jumping. This is due to the fact that the efficiency of some pixels is above the expected efficiency determined through simulation.

As mentioned before, pixel jumping is when radiation interactions occur under one pixel and are recorded by a neighboring pixel. This effect has been studied and is caused by space charge in the detector, yielding electric field non-uniformities, which ultimately skews the electron-cloud track. Experiments have shown that this problem cannot be resolved by a simple efficiency normalization of each pixel.

Generally, pixel jumping does not have as a great of an effect on thin CdZnTe detectors. However, low energy gamma ray imaging using thicker detectors is more susceptible to pixel jumping, as the events occur near the cathode surface such that the electron clouds have almost the entire bulk of the detector to drift through before being collected by the anode side. Therefore, as the thickness increases, the probability that the electron cloud will drift away from the original interaction pixel also increases.

High quality Compton images have been formed using the same detector system for many years. Therefore, it has been hypothesized that this effect has a more dramatic effect on coded aperture imaging as compared to Compton imaging. This may be due to the fact that a simple shift from one pixel to another could completely reverse the contribution of the count in CAI, as compared to Compton imaging, which would create a small effect if one event were shifted, and no real effect in cone angle if both events shifted together by the same amount. The first half of Chapter 6 is devoted to better understanding pixel jumping effects and possible methods to reduce its effect on CAI.

Comparison to Simulations

When comparing the coded aperture image of measurements of the most uniform detector to images formed using MCNP5 simulated data of the same geometry in Figure 5.12, one can see that the sidelobes are prominent in both cases, likely a property of the random mask design, rather than a product of a material property, such as pixel jumping, since the simulation of the detector contains no such physics. These results are promising since it proves that there are no fundamental issues using thick CdZnTe detectors for coded aperture imaging, which had never been demonstrated before.
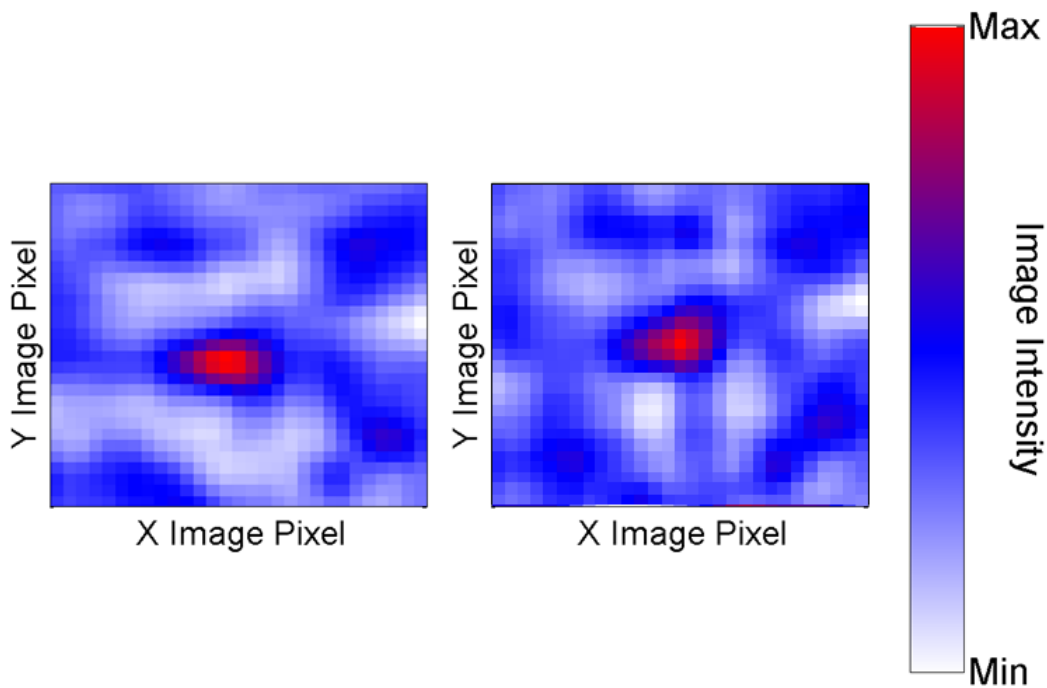
Figure 5.12: Single-detector image created using data from most uniform detector of four-detector array (left) and MCNP5 simulation of the same geometry (right).

Improvement due to Depth Information

Pixel jumping effects are smoothed out due to the fact that a different shadow is cast on the detector at different interaction depths. To demonstrate this, measurements were taken using Ba-133 (356 keV) such that gamma rays penetrate deeper in the detector, rather than interacting near the surface at lower energies, such as 122 keV. The interactions are binned by depth, in distance from the cathode surface. Then images are formed using depths 0 – 2 mm and 2 – 5 mm. Figure 5.13 shows images from both of those depth ranges, separately, and then combined.
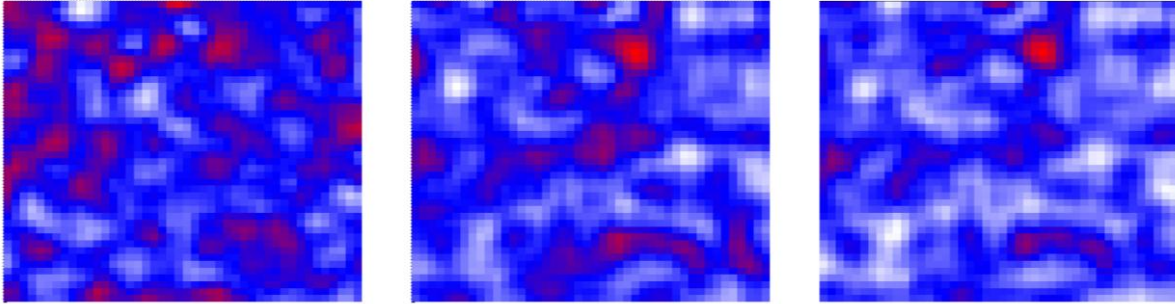
Figure 5.13: Images of Ba-133 (365 keV) produced using 450 counts each interacting between depths 0 – 2 mm (left), between depths 2 – 5 mm (middle), and a simple addition of two (right) showing reduction of artifacts, possible produced by pixel jumping effects.

The combined image is much better than the individual images, therefore, it is beneficial to consider actual depth of interaction when implementing CAI. This depth correction is implemented in the real-time, event-by-event image reconstruction, which is described later in Chapter 8.

Improvement Due to Uniform Detectors

At a later date, four of the most uniform detectors of a nine-detector array were used to reconstruct images of a Co-57 source at a distance of 35 cm from the mask. Using a computer controlled track, the source was mechanically moved in 1 cm increments from the center to the edge of the FOV. First, each detector's image was reconstructed individually, providing better individual detector images than in the past, most likely due to the improved uniformity of the detectors. Then the combined image was created, by simply summing the individual images. The improvement in the combined image is encouraging and promising. Benefits of using detector arrays will be covered in more detail in Chapter 7.
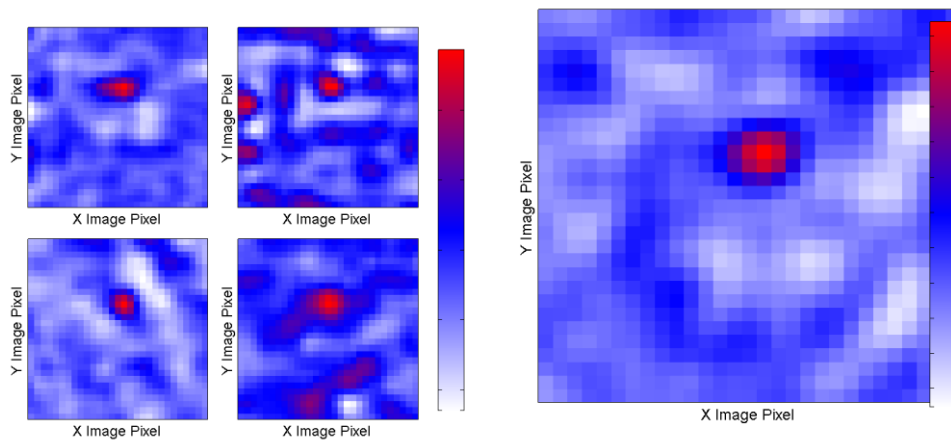
Figure 5.14: Improved images of Co-57 (122 keV) using four uniform detectors, individually (left), and combined (right).

Improvement Due to Increased Counts

To demonstrate the image improvement due to increased number of counts, Ba-133 (81 keV) was imaged using both 1×10^3 and 1.2×10^4 counts. Artifacts due to the random mask design will remain, however, there is much improvement in the image contrast. A method is later implemented to calculate SNR to quantify this improvement.
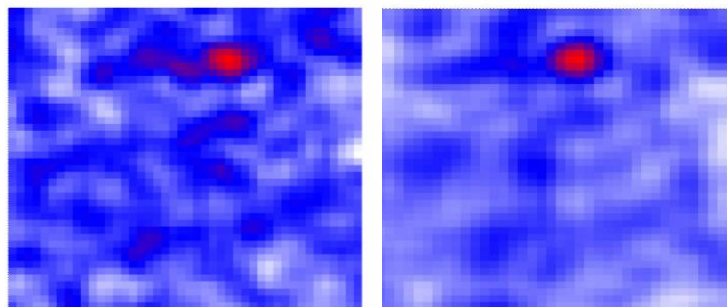
Figure 5.15: Image of Ba-133 (81 keV) using 1E3 counts (left) and 1.2E4 counts (right)
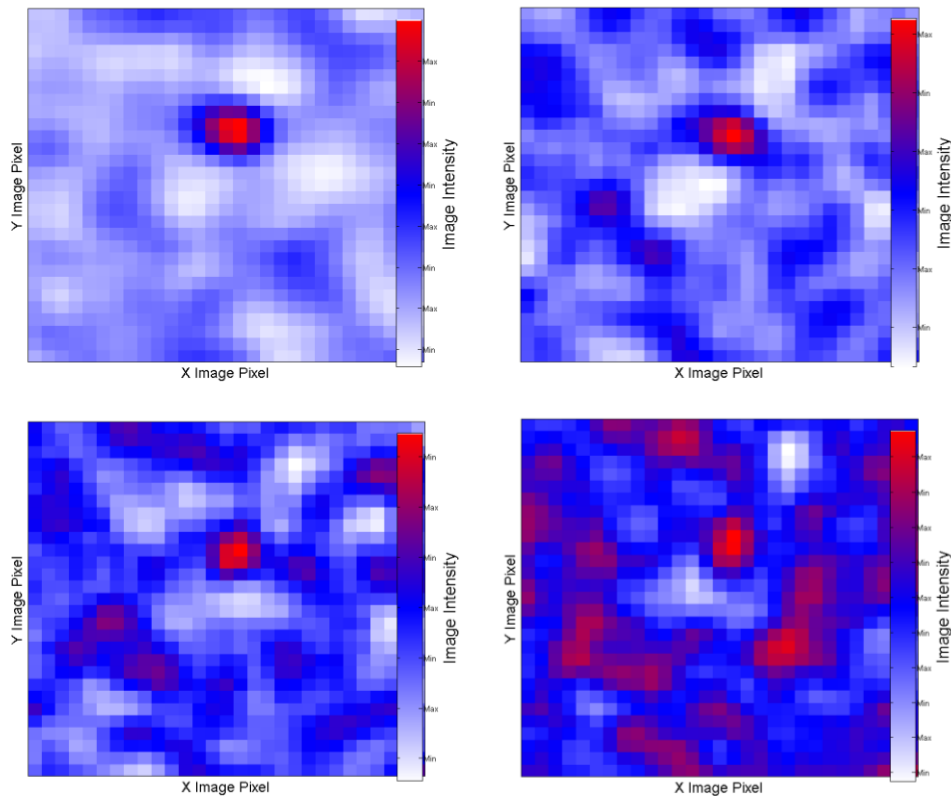
Figure 5.16: Image using four-detector array of Co-57 (122 keV) using 1.2×10⁴ counts (upper left), 500 counts (upper right), 50 counts (lower left), and 20 counts (lower right).

5.2 Non-Cathode-Side Imaging

Once cathode-side imaging was studied and proven possible, the next logical step was to implement near 4-pi CAI is applying a mask to one of the four non-cathode sides of the detector.

Mask Design

The count distribution to be considered on the side is the x-depth or y-depth dimension, depending on which side of the detector is being considered. Since only one of the four detectors provided a uniform response, a single 21 × 21 random mask, with 1.72 mm × 1.72 mm × 1 mm mask elements, is centered on the side of that detector at a distance of 2 cm from the non-cathode side, as shown in Figure 5.17.

Figure 5.17: A 21 × 21 random mask random mask pattern placed on the non-cathode side of a single detector.

Image Reconstruction

The difference in non-cathode side image reconstruction is that rather than using the discrete x-y pixel count distribution to reconstruct the image, either the x-depth or y-depth count distribution must be used. Depth is a continuous parameter ranging from 0 to 15 mm (thickness of the detector), therefore must be discretized. This is generally done in forty depth bins. However, it can be optimized to match the position resolution that would reconstruct the best image.

Experimental Setup

Similar to the non-cathode side, a Co-57 (122 keV) source is placed 20 cm from the mask. Since the source is relatively close to the system, near-field effects are once again accounted for the imaging algorithm. The source is incrementally moved along a plane 20 cm above the mask from one edge of the FOV to the other.

Results

Images were reconstructed at the various source positions within the FOV, and although the source direction was accurately pinpointed each time, the images were significantly noisier than through the cathode-side mask. There are at least three possible explanations for noise in the non-cathode side image. First, due to the fact that low-energy gamma rays interact near the surface of the detector, there may be non-uniform charge loss

due to the variable electric field on the outer edges of the detector. Secondly, only 11 pixels are being irradiated rather than 121 in the cathode-side case making it more sensitive to issues with individual pixels. The image reconstruction should suffer from the fact that one of the 11 pixels is very noisy and does not show a clear Co-57 photopeak. And lastly, the mask element size selected for the side was on the order of a detector pixel (1.72 mm × 1.72 mm, rather than 3.44 mm × 3.44 mm), therefore making it much more susceptible to effects of pixel jumping. Non-cathode side characterization will be studied in further detail in Chapter 6 to determine ways to improve the image.
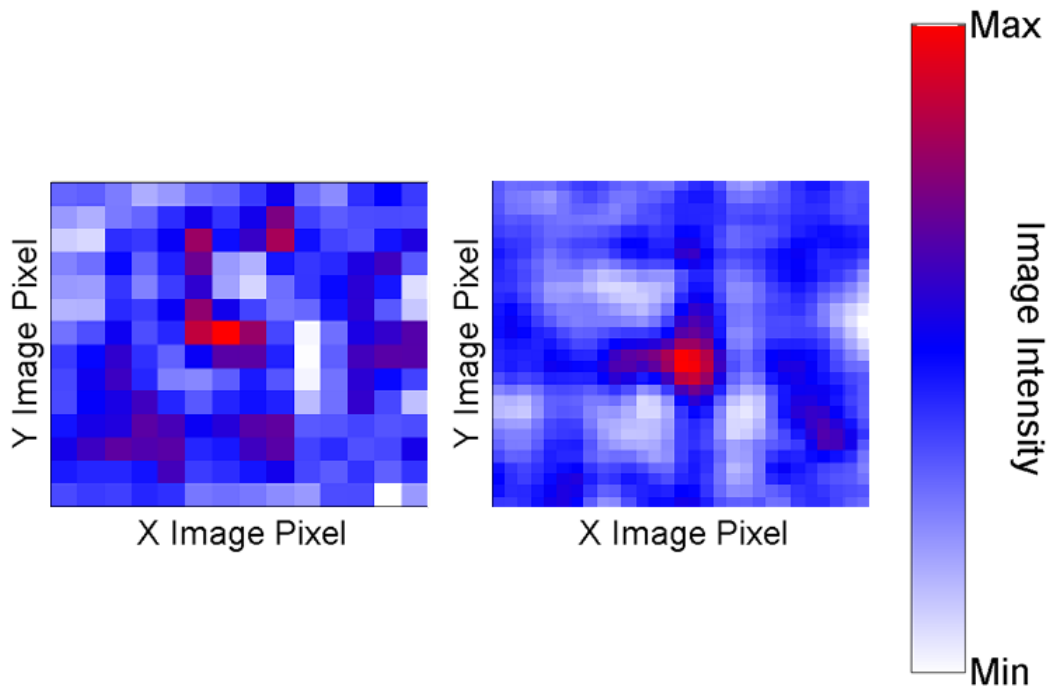
Figure 5.18: A single-detector image of Co-57 through one of the four non-cathode side masks (left). The resultant image is much noisier than the cathode side image of Ba-133 (right).

5.3 Conclusions

By applying coded masks to the cathode and one of the four non-cathode sides of a detector, it has been shown that near 4-pi coded aperture imaging using 3D CdZnTe detectors for low energy gamma rays is indeed possible. However, the quality of the images formed is limited by detector properties, such as uniformity. Pixel jumping effect explains the detector's non-uniform response to flood irradiation. A larger mask element was used to reduce the effects of pixel jumping, which heavily affects CAI versus other

imaging modalities, such as Compton imaging. Side imaging is affected by the non-uniform electric field near the edge of the detector, reducing the position resolution, resulting in noisier coded aperture images. Pixel jumping and non-uniform electric field properties will be explored in more detail in Chapter 6. Overall images are improved by combining images reconstructed from various depths in a single detector, as well as individual images from multiple detectors in an array. Benefits of multi-detector arrays will be discussed further in Chapter 7.

5.4   References

[1]   Joshi Kaye, Sonal; W. R. Kaye, and Z. He. "Experimental Demonstration of Coded Aperture Imaging using Thick 3D-Position-Sensitive CdZnTe Detectors," Nuclear Science Symposium Conference Record, 2009.

[2]   A. E. Bolotnikov, S. Camarda, Y. Cui, A. Hossain, G. Yang, H. W. Yao, and R. B. James, "Internal electric-field-lines distribution in detectors measured using X-ray mapping." *SORMA* (2008)

[3]   Szeles, C., "Advances in the Crystal Growth and Device Fabrication Technology of CdZnTe Room Temperature Radiation Detectors." *IEEE Transactions on Nuclear Science,* vol. 51, no. 3, pp. 1242-1249 (2004).

CHAPTER 6
EXPERIMENTAL LIMITATIONS OF NEAR 4-PI CAI

Up until now, the chapters have demonstrated the feasibility of near 4-pi low-energy gamma-ray imaging using 3D CdZnTe. However, there is greater degradation in quality when comparing images created from measured data versus Monte Carlo simulations. This is in part due to material properties, such as pixel jumping and non-uniform electric fields, as well as readout system and data reconstruction effects, such as trigger thresholds and improper depth determination [1][2][3]. This chapter further investigates the underlying issues that could possibly explain the differences in simulation and measurement, as well as a few suggestions to lessen or eliminate such effects.

6.1 Pixel Jumping

Using a nine-detector system, whose detectors were selected for excellent energy resolution, allows for an opportunity to better understanding pixel jumping. All nine detectors are uniformly irradiated with Cs-137 (662 keV) and then Co-57 (122 keV). The pixel jumping in Co-57 is worse than in Cs-137 as shown in Figure 6.1 and Figure 6.2. This is consistent with the fact that when irradiating the cathode of a detector, low energy gamma rays have a longer path to travel through the detector before being collected by the anode. Of the nine detectors shown in both figures, the detector which provides both high energy resolution and uniformity is located in the second row, third column.
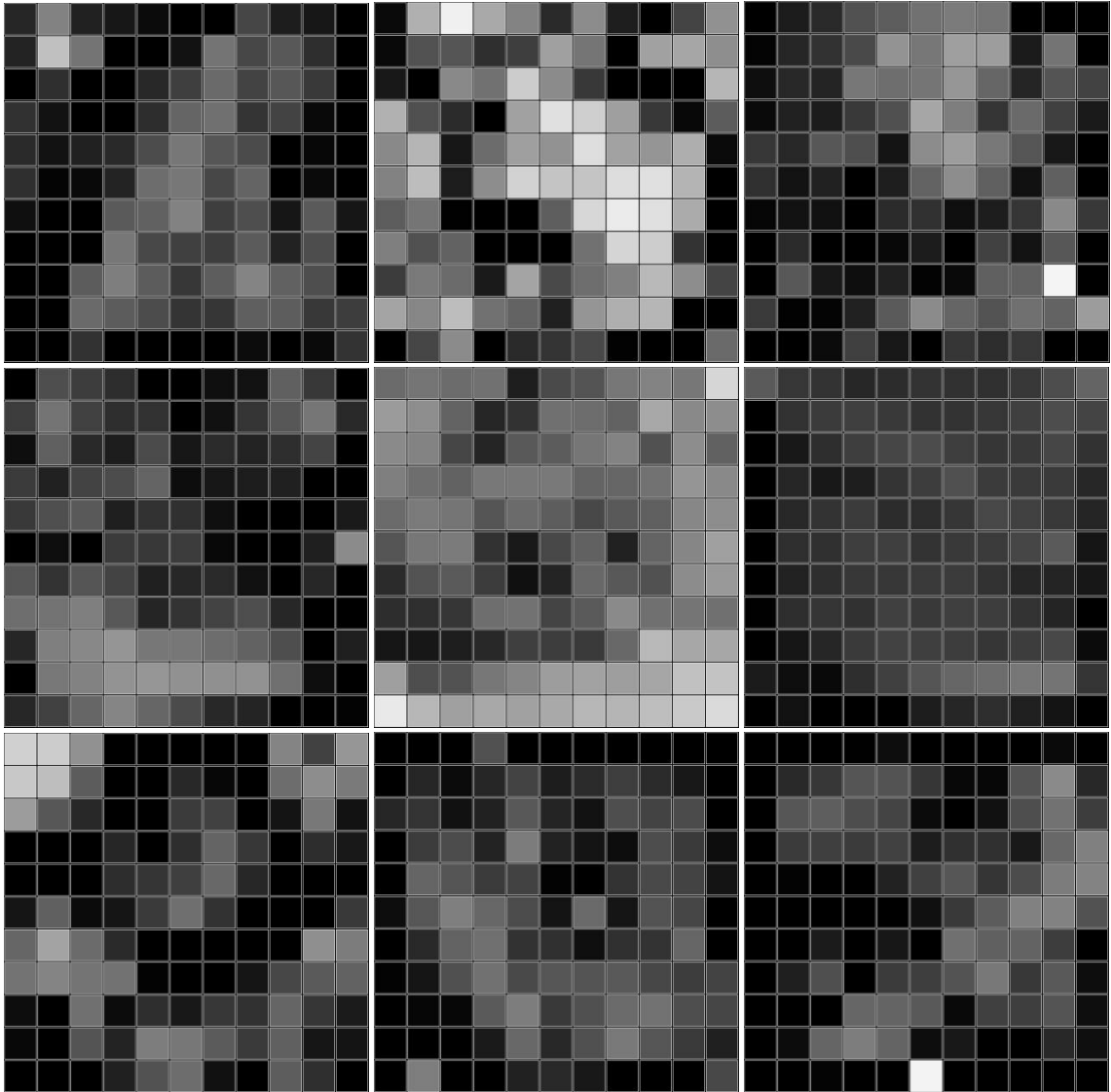
Figure 6.1: Uniformity of nine-detector imaging array using Cs-137 (662 keV). The count scale ranges from 0 to 4×10⁴ counts.
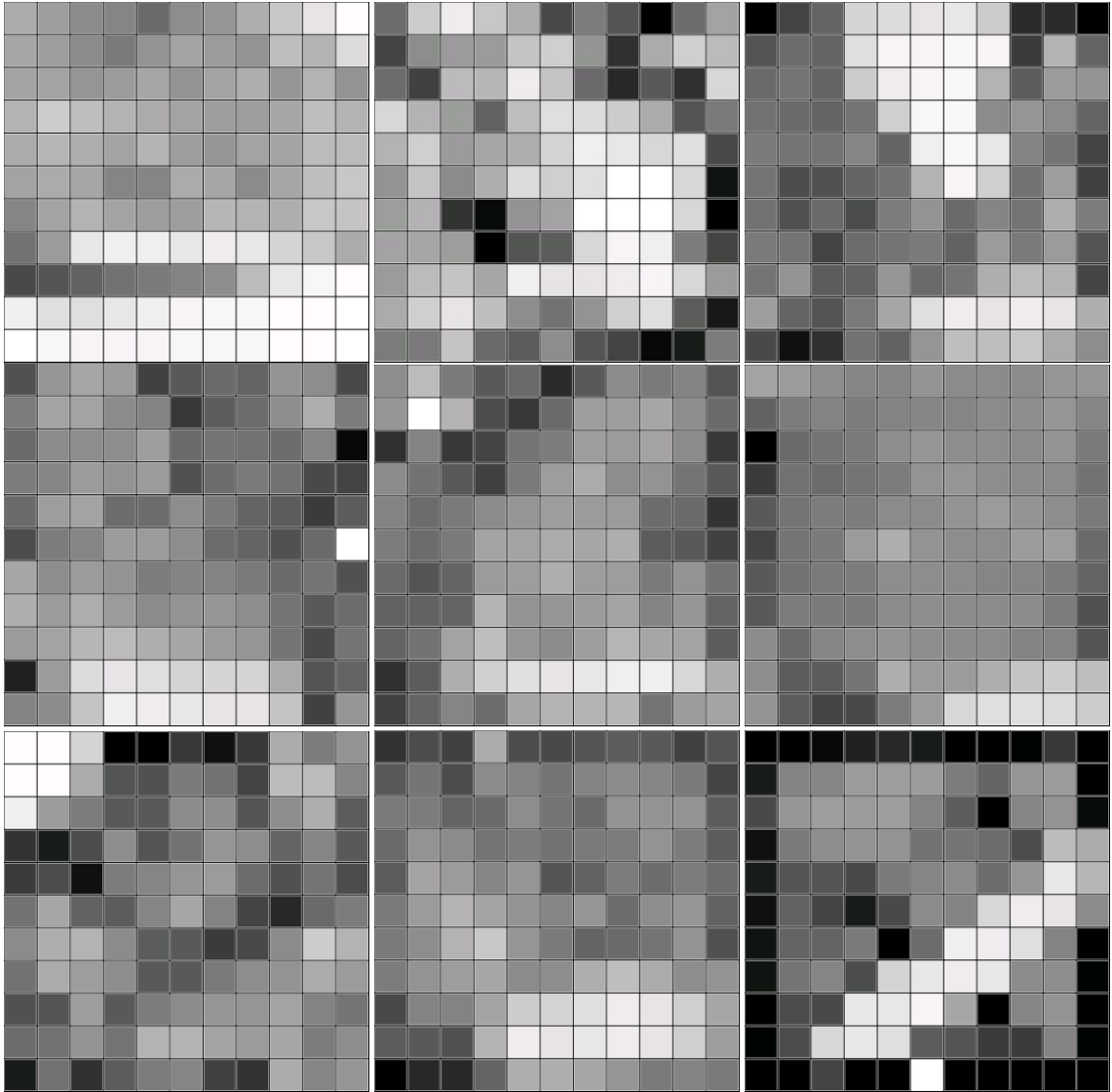
Figure 6.2: Uniformity of nine-detector imaging array using Co-57 (122 keV). The count scale ranges from 0 to 7.5E4 counts.

6.1.1 Collimator Study

To better understand pixel jumping, a collimator study was performed using a 100 μm tungsten collimated Cs-137 (662 keV) rod source. The collimator was incrementally moved, while irradiating columns of pixels across the cathodes of three detectors simultaneously. It is expected that the majority of the counts be recorded in the pixels that were irradiated by the source. However, as shown in Figure 6.3, the lower detector shows slight deviation in counts to the left-hand neighboring pixels. Since this occurs only in the

center of the detector, it is unlikely that this is due to a systematic beam misalignment, but rather material property, most likely pixel jumping.
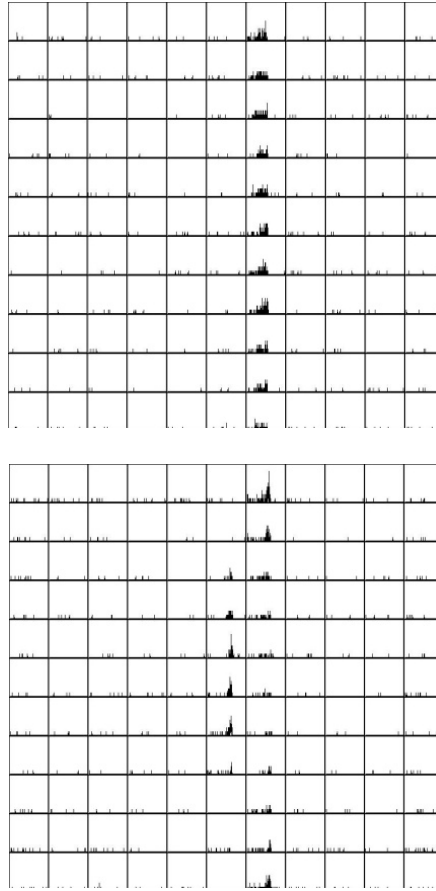
Figure 6.3: The photopeak region of the spectrum in each pixel for two of the nine-detector array irradiated by a collimated Cs-137 source. All counts should occur in the same column of pixels, however, some counts are relocated to neighboring pixels, most likely due to pixel jumping.

6.1.2 Uniformity over Time

Before a pixel jumping correction can be considered, it needs to be verified that it does not change over time. If pixel jumping is observed to be constant over time, then a correction can be applied, ultimately improving coded aperture imaging. To show how uniformity behaves over time, measurements were taken using a single detector and a Cs-137 (662 keV) source. A higher energy gamma ray source is utilized in this measurement, such that bulk effects can be differentiated from surface effects. The source is placed 20 cm from the detector box, and aligned with the center of the cathode side. Figure 6.4 is a plot

of the energy resolution map for this detector to increase familiarity with the detector. The center and lower left regions provide relatively good energy resolution, while the other regions provided poorer energy resolution.

2.24	1.39	1.99	1.33	1.48	1.80	1.07	1.06	1.52	1.17	3.57
2.08	1.14	1.40	0.98	1.00	0.92	1.54	3.04	1.37	1.18	1.63
1.13	1.05	1.04	0.84	0.89	0.97	1.07	1.62	1.06	1.13	1.34
0.97	0.94	0.86	0.88	0.94	0.87	0.92	2.58	1.06	1.15	1.59
1.17	0.85	0.94	0.87	0.89	1.05	0.88	0.94	1.13	1.19	1.33
1.31	0.93	0.95	0.85	0.79	0.97	0.88	0.93	0.82	1.28	1.63
1.26	1.42	1.07	1.04	0.87	0.98	0.85	0.84	1.02	1.31	1.49
1.83	0.91	0.93	0.97	0.84	0.94	0.89	0.84	1.02	1.62	1.55
1.08	0.94	1.04	0.94	0.87	0.94	0.95	0.85	1.24	1.28	1.74
0.91	0.91	0.92	0.86	0.98	1.38	0.92	0.81	1.15	1.66	1.57
1.68	1.25	1.07	1.00	1.02	1.04	1.26	1.37	1.09	1.65	2.28

Figure 6.4: Energy resolution map at 662 keV of detector 4R8 used for pixel jumping studies.

Measurements were taken in a couple different laboratories, which accounts for slight variation in ambient temperature and humidity, at various points in time. The process of moving the detector includes manual biasing up and down of the detector. On day 1, the measurement was taken in laboratory 1. On day 3, the detector was manually biased down and moved to laboratory 2, where the detector was biased up and a second measurement was taken. The measurements were repeated in this location on days 6 and 9.
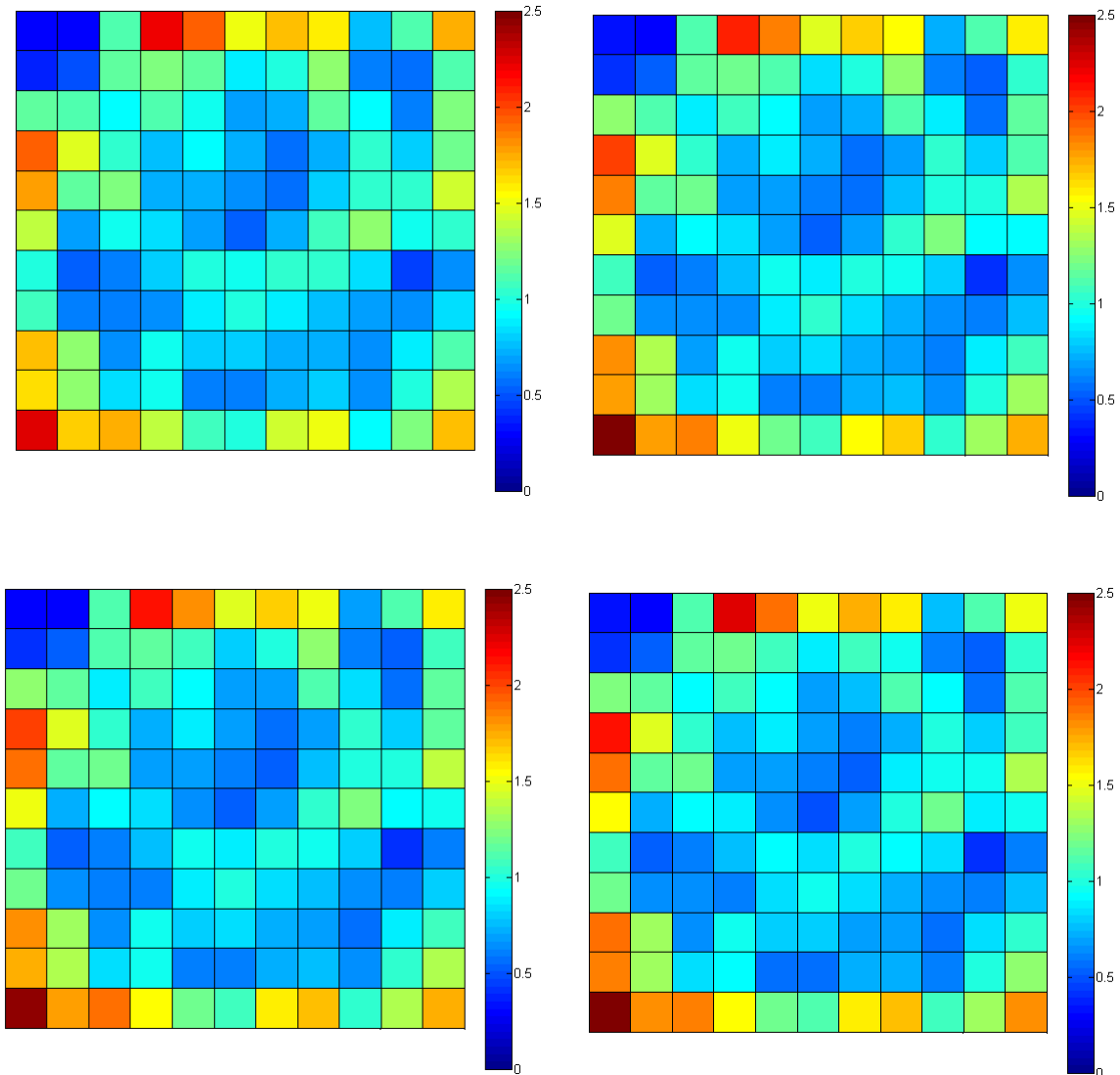
Figure 6.5: Pixel efficiency of detector 4E8 using Cs-137 (662 keV) with at least 1E4 counts per pixel, on Day 1 (upper left), Day 3 (upper right), Day 6 (lower left), and Day 9 (lower right). Each distribution is normalized to the mean pixel count. The count scale ranges from 0 to 2.5 (no units).

The pixel efficiency distribution was plotted for each measurement. Each individual pixel receives approximately 1E4 counts. Each plot is normalized to the mean of the dataset. As shown in Figure 6.5, a very consistent image is observed, showing some change in the lower left-hand corner.

A simple subtraction between the first image and the other three is performed to highlight the differences, shown in Figure 6.6. Since the first measurement varied the most from the other three, it provides the greatest difference.
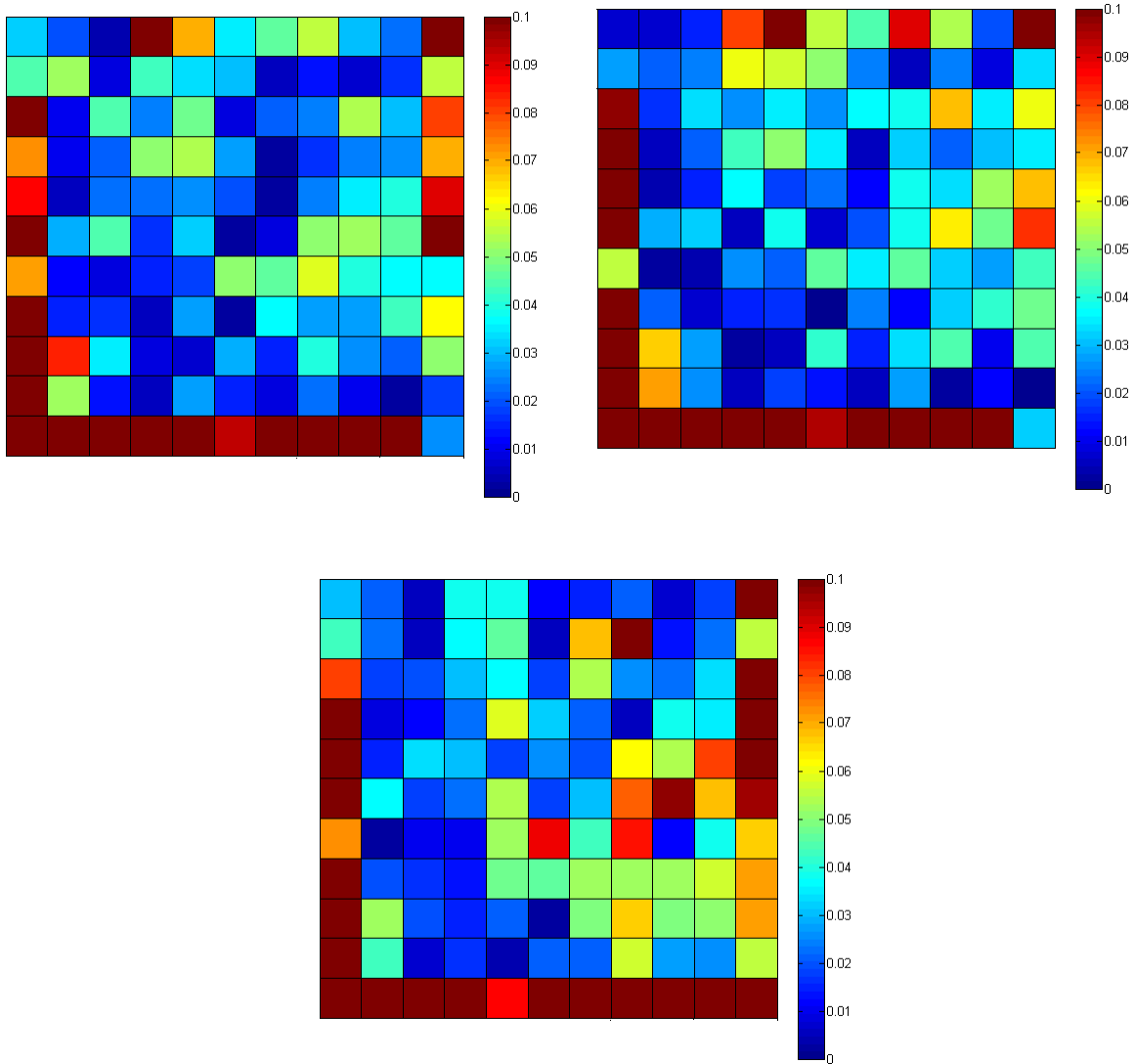
Figure 6.6: Difference between normalized pixel efficiency plots of day 1 and: day 3 (upper left), day 6 (upper right), day 9 (lower). The count scale ranges from 0 to 0.1 (no units).

However, when comparing the difference plots of the last three measurements, the characteristics of the distributions are remarkably similar, as shown in Figure 6.7. Since it seems as though the count distribution remains quite uniform over the period of a week or so, it is likely that it would remain constant over the timeframe of a few years. Due to this consistency of uniformity over time, it seems as though it would be possible to apply a simple correction to limit the impact of pixel jumping. One possible method will be suggested in the following section.
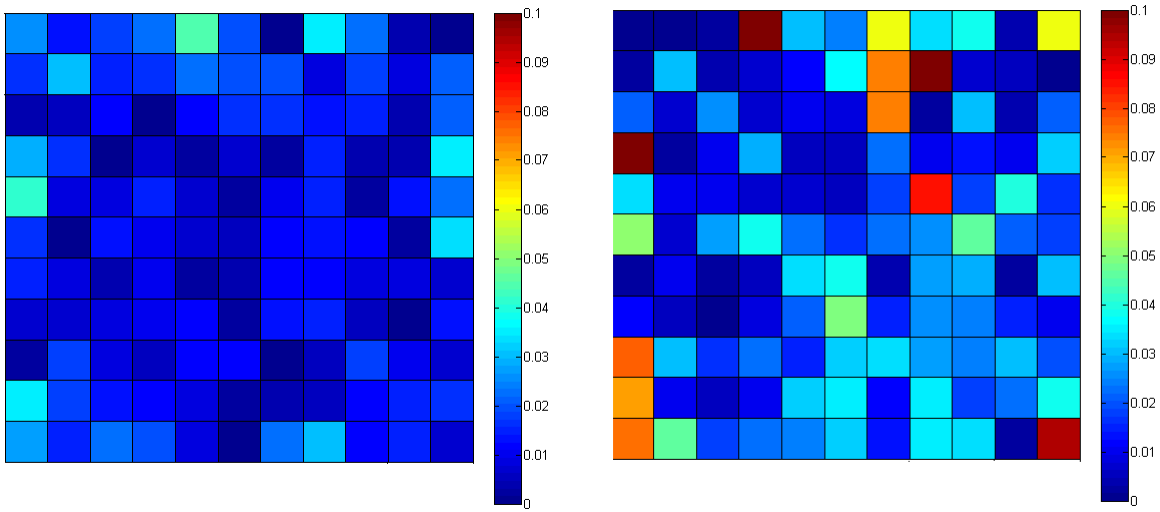
Figure 6.7: Difference between normalized pixel efficiency plots of: day 3 and day6 (left),day 3 and day 9 (right).The count scale ranges from 0 to 0.1 (no units).

Based on this evidence, it would appear that pixel jumping is constant over time. This means that for each possible gamma-ray interaction position within the CdZnTe there is only one pixel that can collect the charge, albeit that pixel may not be directly underneath the interaction location. This collection process defines the effective volume under each pixel. In an ideal detector, these effective volumes would have square cross sections that extend directly from the anode pixel to the cathode plane. However, in a detector with pixel jumping, these volumes have non-uniform shapes.

The key is to know exactly where the gamma ray interacts and which pixel it triggers and is collected by, knowing that it may not have been the pixel under which the interaction occurred. An ideal correction would involve determining the true shape of the effective volume for each pixel, such that this volume would be used for the back-projection area through the mask when an event is observed in that pixel. It should be noted that even this ideal algorithmic correction to pixel jumping is significantly less desirable then using a good quality detector that does not suffer from pixel jumping. If a single pixel can collect charge from a spatial region greater than the pixel itself, then the spatial resolution of that pixel has inevitably been degraded. Also, if the effective volume of each pixel is not uniform, then it becomes much more challenging to find an appropriate mask pattern to minimize image artifacts. In the absence of pixel jumping an optimized pattern such as

MURA is an excellent choice, but with severe pixel jumping even a MURA mask will not have a significant advantage over a random one.

6.2 System Readout and Reconstruction Effects

In Chapter 5, it was shown that non-cathode side imaging was much noisier as compared to the cathode side images. This section describes non-material properties, including the system readout and reconstruction effects on low-energy gamma rays in the CAI range. The effects of both the cathode timing trigger and proper depth reconstruction are investigated using bulk irradiation of the non-cathode side of the detector.

6.2.1 Timing Trigger Threshold

Measurements were taken using three detectors: 4E6, 4E3, and 4E7 to investigate the effects of timing trigger thresholds on low-energy gamma ray detection. All three detectors were irradiated with a Co-57 and an Am-241 source, spanning the CAI range of energies. Energy spectra are produced using the data from these measurements, and are compared between detectors. To utilize information that would otherwise be lost, spectra were created with events where a valid cathode timing trigger is both required and not required. When the timing trigger is not required, all events are included in the spectrum. However, when the cathode timing trigger is required, events are lost from the lower energy region of the spectrum, as it is less likely that a low energy event will induce sufficient charge on the cathode preamplifier to result in a trigger. The low energy event is still read out when the charge reaches the anode, as the rapid change in the weighting pixel as the charge approaches a pixel is sufficient to generate an anode trigger.

Figure 6.8 is an energy spectrum from counts recorded in detector 4E6. The two peaks associated with gamma emissions from Co-57 at 122 keV and 136 keV are apparent. However, the 60 keV peak due to Am-241 is invisible in this case. The reason for this becomes more clear when comparing this energy spectrum with that of the other two detectors.
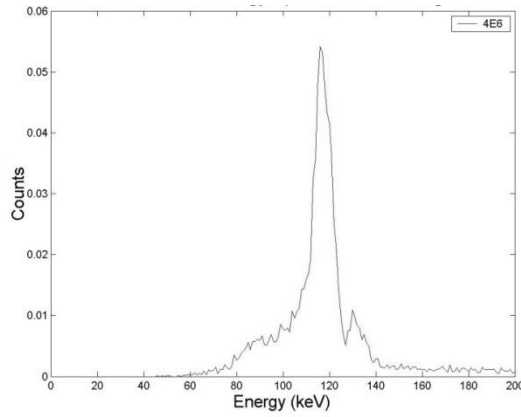
Figure 6.8: Energy spectrum of 4E6, with timing trigger required.
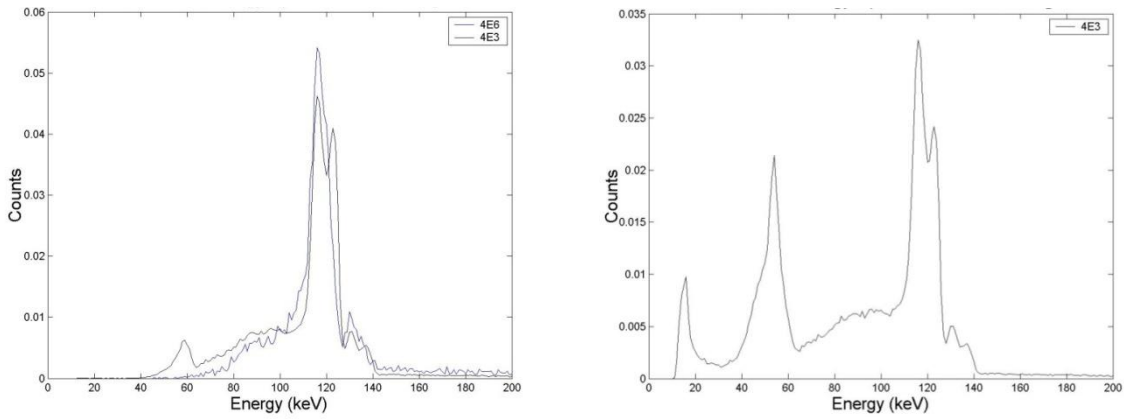
Figure 6.9: Energy spectrum of 4E6 and 4E3, with timing trigger required (left) and 4E3, without timing trigger required (right). When focusing on the 4E3 comparison, the low energy peaks are missing when timing trigger is required.
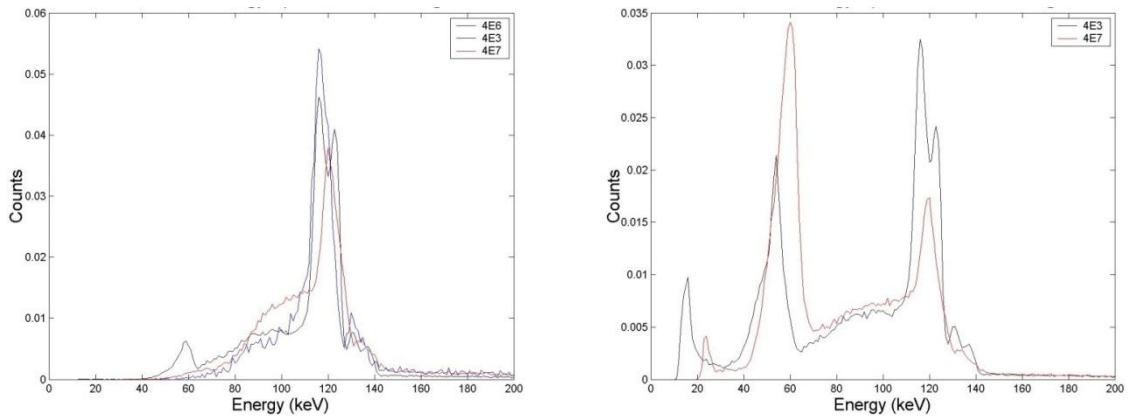
Figure 6.10: Energy spectrum of 4E6, 4E3, and 4E7, with timing trigger required (left) and 4E3 and 4E7, without timing trigger required. When focusing on the 4E7 comparison, low energy peaks are missing when timing trigger is required.

When comparing Figure 6.9 of the spectrum of detector 4E3 with timing trigger required to the spectrum from detector 4E3 with no timing trigger required, in the latter case the lower energy peaks are much more prominent. The difference in the spectra between timing required and not is due to the fact that the timing trigger threshold is set too high to recognize lower energy events. The same is also true when comparing 4E7 in Figure 6.10. The conclusion that can be made from this is that to perform CAI, all events should be considered, thus the cathode trigger requirement was ultimately disabled in Polaris.

6.2.2 Depth Reconstruction

Next, the depth distribution is plotted for each of the three detectors with an energy window centered at 122 keV. Figure 6.11 shows that the depth distribution of detector 4E6 ranges from a CAR of 0.5 to 1 rather than the full range of 0.1 to 1.
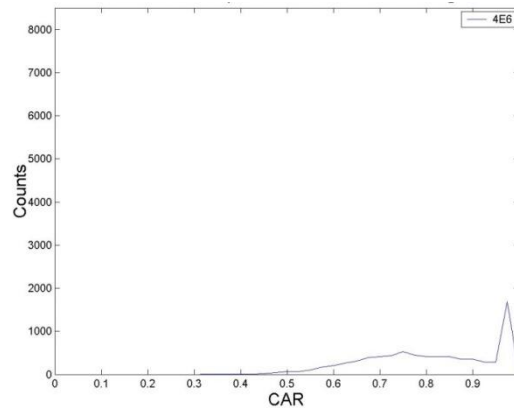
Figure 6.11: Depth distribution for 4E6 at 122 keV with timing trigger required.

This is then repeated for detector 4E3 as shown in Figure 6.12, which yielded a much flatter depth distribution, probably due to the fact that the anode and cathode gain and offset were calculated more accurately than for detector 4E6.
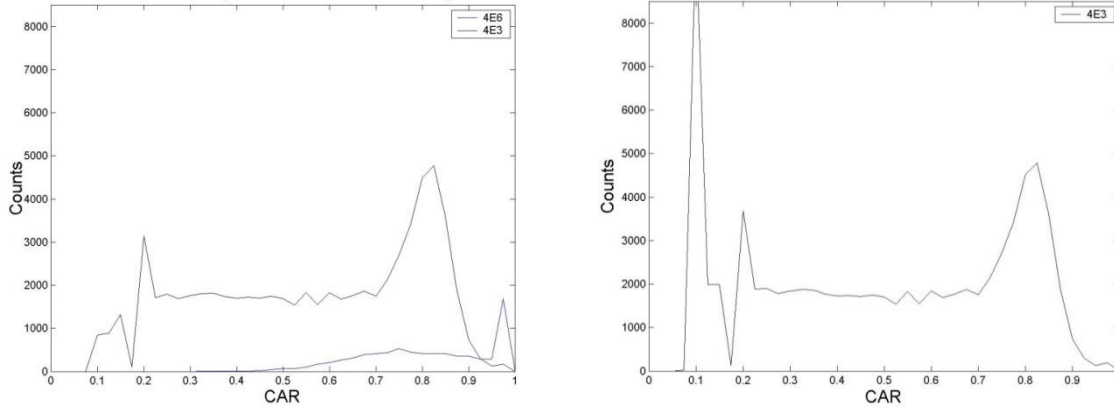
Figure 6.12: Depth distribution for 4E6 and 4E3 at 122 keV with timing trigger required (left), and for 4E3 at 122 keV without timing trigger required (right).

Figure 6.13 shows the depth distribution for detector 4E7, which is not as uniform as detector 4E3, however spans a larger depth range than detector 4E6. When comparing the depth distribution plots with timing trigger versus depth distribution of all events, a few significant features include the peak on the cathode side of the detector (CAR = 1), as well as omission of the events on the anode side (CAR = 0).

The pileup of events on the cathode is due, in part, to hole movement, as well as the events that are initially reconstructed at a depth beyond the cathode and arbitrarily assigned to the cathode position. These events beyond the cathode occur because both the cathode and anode signals have noise associated with their signals, so events already close to the surface could appear beyond it. When these events occur the position must be placed within the volume of the detector and the cathode surface is the highest probability position estimation.
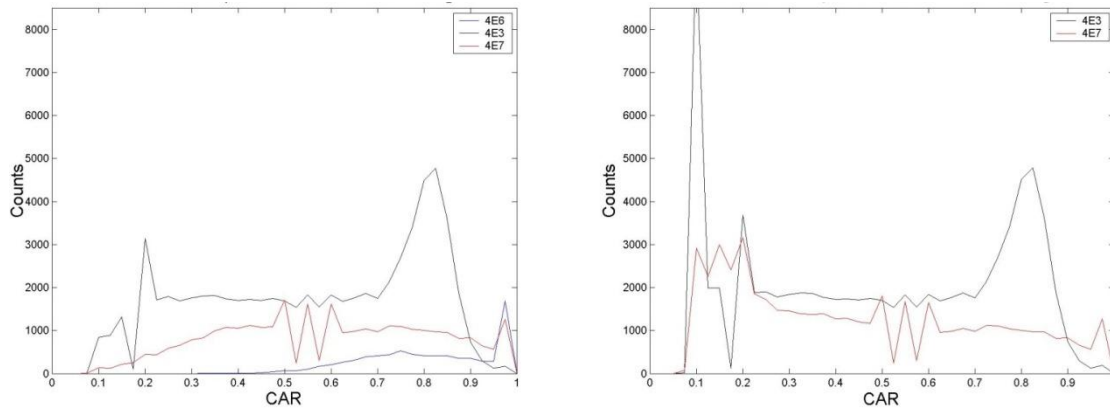
Figure 6.13: Depth distribution for 4E6, 4E3, and 4E7 at 122 keV with timing trigger required (left), and for 4E3 and 4E7 at 122 keV without timing trigger required (right).

The cathode-triggered spectrum tails off near the anode due to the fact that the cathode is less likely to trigger events near the anode for two reasons. Most likely, the anode triggers before the cathode, therefore, the event will not appear in the cathode triggered spectrum, even though the cathode may have eventually been triggered. Since it did not receive an expected timing value, the event was thrown out. The second reason is that the event did not induce sufficient charge on the cathode to result in a trigger due to its limited drift length before collection.

6.2.3 Depth Reconstruction Study

A collimator was setup to perform measurements with Co-57 to see what depth reconstruction looks like at CAI energies. Five (5) minute measurements were taken using a 160 μm collimated fan-beam source at different depths (relative to the anode side). The goal of these measurements is to determine the depth resolution at each depth. Through these experiments, what was discovered is that the depth resolution varied significantly between the high quality "jewelry box" detector (1.7 mm) and the standard Redlen detector (2.6 mm). This is evident over all depths from 1 mm to 15 mm. A single depth is shown in Figure 6.14.
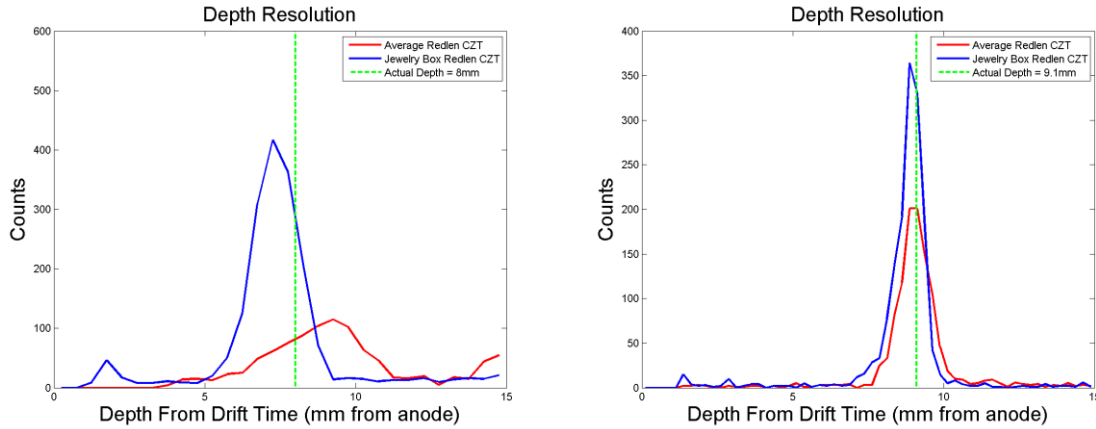
Figure 6.14: Comparison of collimated Co-57 measurement using average Redlen CdZnTe (FWHM = 2.6 mm) and jewelry box Redlen CdZnTe (FWHM = 1.7 mm) (left), and when the proper depth correction is applied (right).

When comparing plots from when improper depth correction (left) to proper depth correction (right), both the FWHM and alignment improve significantly in the latter case. To ensure that proper depth reconstruction is applied, the accurate determination of the gain, as well as cathode and anode baseline is key. The gain does not have as great of an affect at low energies as it is pinned at 662 keV. Therefore, the low energy depth reconstruction is most sensitive to the baseline offset. The cathode baseline offset is the most difficult to accurately determine, and therefore the most likely cause of the degradation.

After performing all three studies in this section, it is evident that for successful implementation of CAI, it is important that the cathode timing requirement is disabled and that appropriate depth reconstruction be performed by proper determination of the baseline offset for both cathode and anode signals such that low-energy events are considered and properly reconstructed.

6.3 Side Characterization

To better understand material properties which affect side imaging, including the severity of the non-uniform electric field near the edge of the detector, a collimator experiment was performed using a 100 μm collimated fan-beam Co-57 source, scanning in both the vertical and horizontal dimensions of the non-cathode side. The goal of these

measurements to determine the effective position resolution, and to better understand the cause of the degradation of side imaging in measurements, compared to simulation.

In one dimension it is assumed that the position resolution is equivalent to the pixel pitch, of 1.72 mm. The other dimension, depth, is determined using the collimator results; the assumption is that this value is approximately 1.5 mm. This result will help determine the appropriate mask element to detector pixel ratio, as well as the effective side imaging area due to the anode dead layer, which has been shown to be as large as 3 mm.

6.3.1 Vertical Collimator Measurements on Side Surface

The collimator is set up such that the detector is irradiated from the side so that the same row of 11 detector pixels are irradiated at various depths, as shown in Figure 6.15.
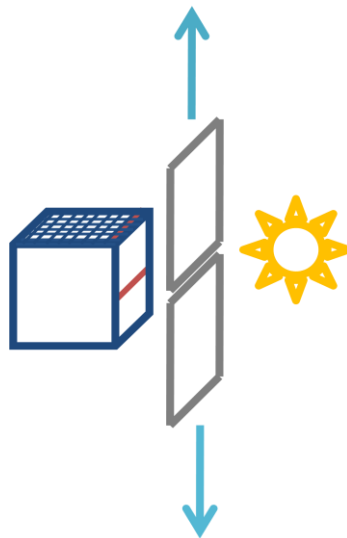
Figure 6.15: Collimator experimental setup to irradiate a single strip of pixels at various depths. Since a low energy Co-57 (122 keV) source is being used, most interactions occur in the edge column of pixels.

The first step is to determine the edge position and extent of the detector within the box. This is done by systematically sweeping the beam across the cathode edge of the detector. Measurements were taken at 0.1mm increments. The count rate at each of these positions is determined, and the cathode edge was estimated to be the halfway point between the maximum count rates (beam fully on the detector) and minimum count rate, supposedly from background (beam fully off the detector), as shown in Figure 6.16.
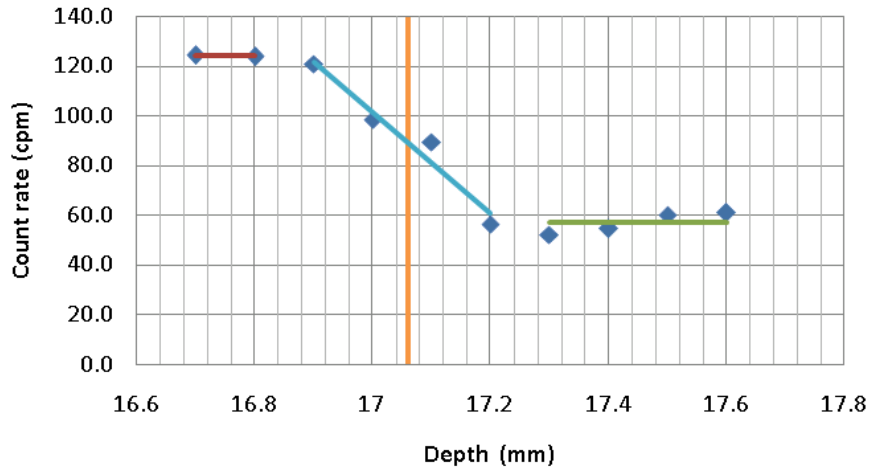
Figure 6.16: The collimated beam is swept across the detector to estimate the location of the cathode edge. The orange line corresponds to the approximate collimator position, halfway between the fully "on" and "off" positions.

Once the cathode edge was determined, thirty measurements were taken between the cathode and anode with a step size of 0.5mm, as shown in Figure 6.17. The black vertical strip represents a position where data was not recorded correctly, but does not indicate any issue with the material or reconstruction.
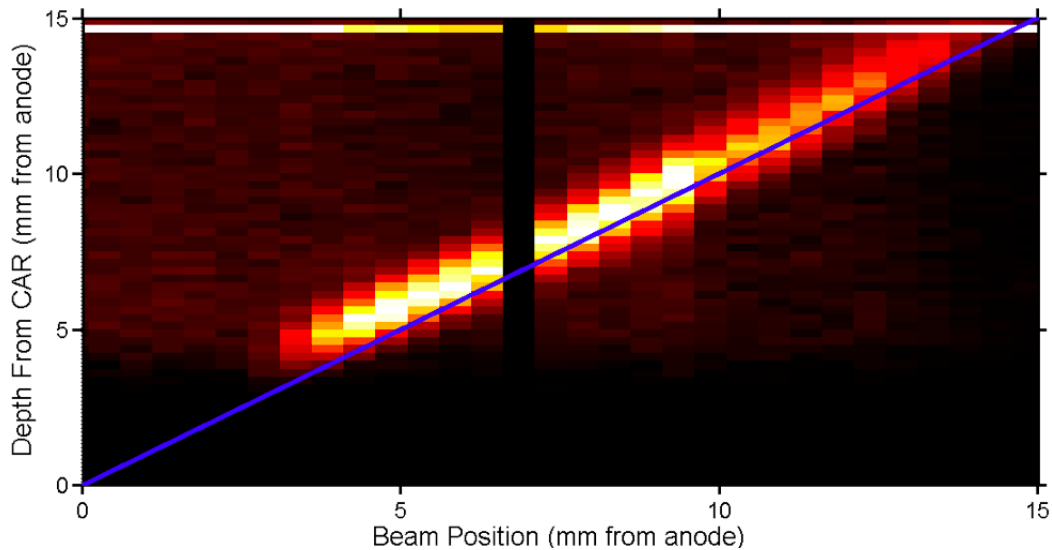
Figure 6.17: Cathode-to-Anode Ratio (CAR) versus true depth (FWHM ~ 1.4 mm) at 122 keV. Dead layer between 0 to 3 mm from anode.

The results of the vertical scanning shows that the depth can be recorded accurately over a significant fraction of the crystal, if the depth reconstruction is performed correctly. The effective size of the crystal is 12 mm rather than 15 mm, due to an approximate 3 mm dead layer near the anode at 122 keV. This should be considered when designing a mask and when establishing expectations on system performance.

6.3.2 Lateral Collimator Measurements on Side Surface

The collimator measurement is then repeated in the other dimension, still using the same 100 μm collimated fan-beam Co-57 source, whereas each measuremement now irradiates a single pixel at a time, at all depths simultaneously,as shown in Figure 6.18. The collimator is moved vertically in small enough increments to determine how distinct the transition is between each pixel and the effective area of each pixel.
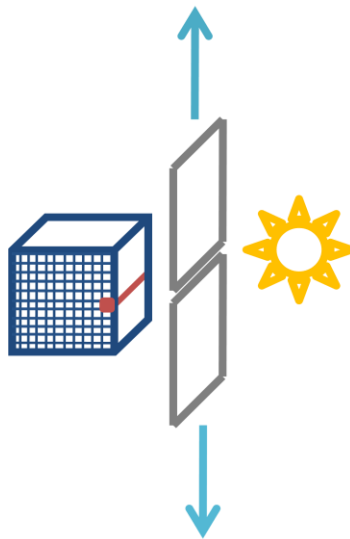
Figure 6.18: Collimator experimental setup to irradiate a single pixel at all depths.

For each measurement, a region of interest (ROI) was selected around the Co-57 122 keV photopeak in the energy spectrum. A plot of the energy spectrum in each pixel is used to determine whether the center of the detector or the gap between detectors was being irradiated, as shown in Figure 6.19.
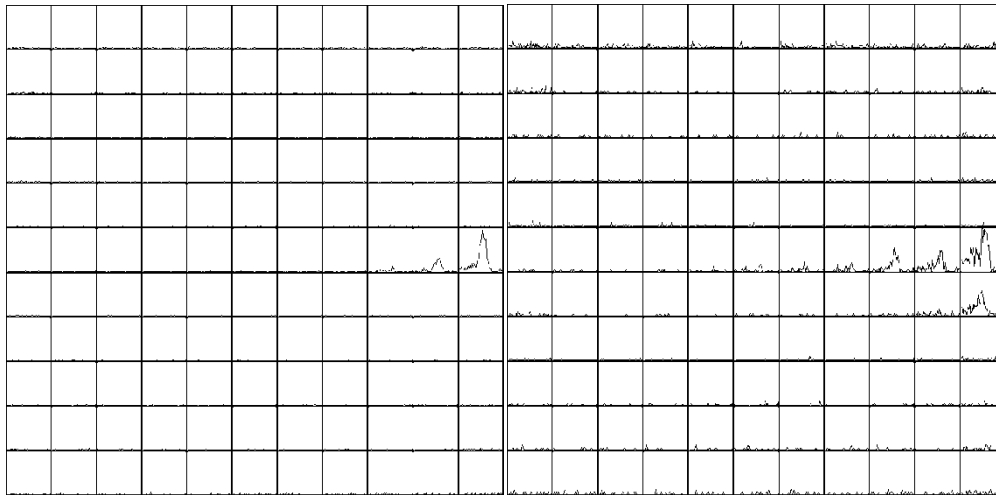
Figure 6.19: An example of a side irradiation of a single pixel at all depths displaying the energy spectrum at each beam position to determine whether the center of a pixel is being irradiated (left), or if the beam is directed at the gap, such that counts are being shared between detectors (right).

For each beam position, only the number of counts within the ROI in the right-most pixel is recorded, since 122 keV gamma rays do not penetrate more than a few pixels. Theoretically, when plotted, the distribution of counts versus beam position should look something similar to Figure 6.20. However, in reality the pixels will not have such distinct edges, and will result in a transition region between pixels. The point of the experiment is to determine the intervals between pixels, and correlate it to the active area of each pixel.
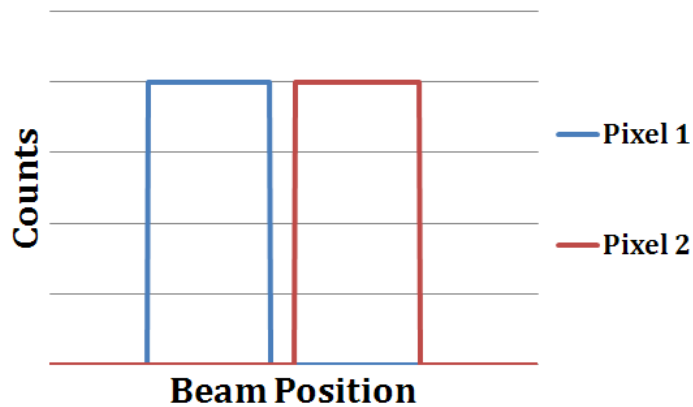
Figure 6.20: An ideal count distribution in two neighboring pixels as a function of beam position.

Once the detector-collimator was setup, 10 minute measurements were taken with both the 100 μm beam and the 50 μm beam to determine if the 100 μm beam could provide precise enough position information and counting statistics for the same measurement

75

time as the 50 μm beam. The obvious benefit of the 100 μm beam is the improved counting statistics, while the 50 μm beam would provide better position precision. The question is whether or not that precision is necessary to determine the end of one pixel and the beginning of the next.

Figure 6.21 shows the count distribution in all 11 pixels where the beam is positioned between two pixels (shown in green and red). As the beam is swept across the length of the detector, the count rate decreases in one pixel (green), while simultaneously increasing in the neighboring pixel (red).
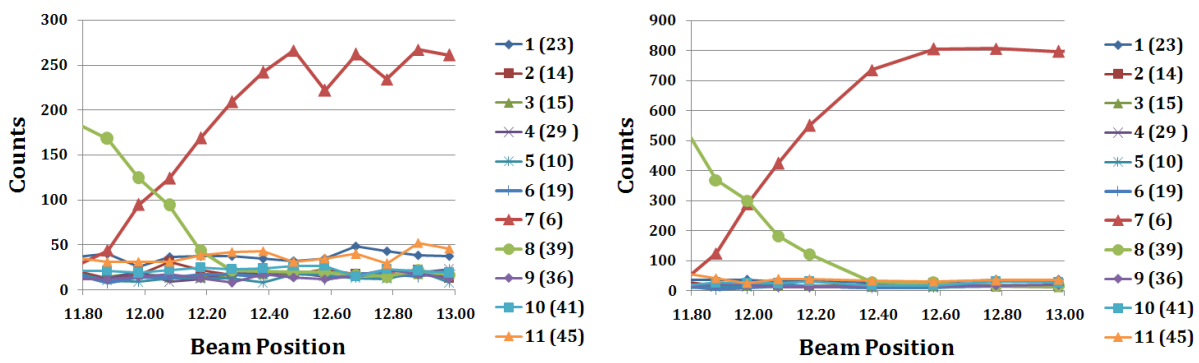
Figure 6.21: Counts versus beam position between two pixels (green and red) using a 50 μm beam (left) and 100 μm beam (right). The counts in the other pixels are most likely due to background.

The 50 μm beam introduces greater statistical noise due to the reduced count rate, and does not seem to provide more information about the position of the pixel edge. Therefore, the 100 μm beam should be sufficient for these measurements. In the interest of time, five (5) minute measurements were taken with the 100 μm beam in 50 μm intervals across the entire 20 mm length of the edge of the detector.
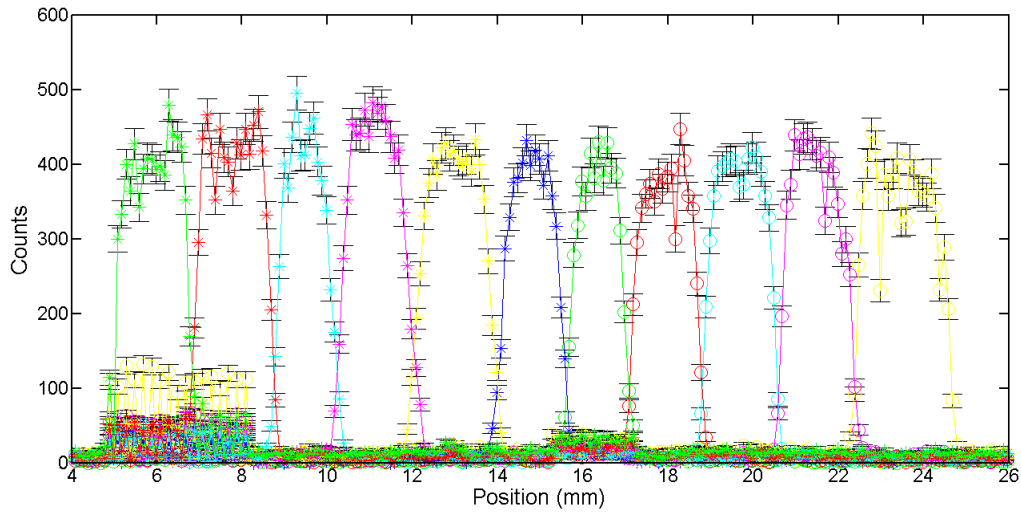
Figure 6.22: Counts versus beam position across all depths of the detector. Each color represents a different detector pixel.

The result of the collimated measurement in Figure 6.22 shows that unfortunately the width of each pixel width is variable. The mean pixel pitch is 1.735 +/- 0.1772 mm. Similar to pixel jumping, the variablility may pose a problem while reconstructing side coded aperture images if the actual side pixel widths are not considered during image reconstruction.

It is reasonable to believe that these widths remain constant over time. However, if one were to characterizing each detector and apply a correction it would be very time costly, as these measurements are very tedious. If high quality non-cathode side images are desired, it would bemore efficient to simply acquire higher quality and more uniform crystals.

6.4 Conclusions

As shown in the previous chapters, image quality using measured data just does not compare to the Monte Carlo simulations, even when applying expected, and realistic, energy and position uncertainty. This is due to material, as well as system readout and reconstruction properties. System properties, which are much more easily adjustable and controllable, include proper depth reconstruction, as well as disabling of the cathode timing trigger requirement, which affects the detection of low energy events.

Material properties include non-uniform electric fields, resulting in pixel jumping and inconsistent and unpredictable effective pixel sizes. A possible solution to correct for these effects is to map out each detector by individually irradiating every pixel and determining the response; this is very tedious and impractical. Another idea is to apply a correction to remove or lessen the contribution of pixels that incorrectly reconstruct the source direction. Nonetheless, nothing is as effective as selecting uniform, high quality detectors where these effects are minimal in the first place.

6.5 References

[1]   A. E. Bolotnikov, S. Camarda, Y. Cui, A. Hossain, G. Yang, H. W. Yao, and R. B. James, "Internal electric-field-lines distribution in detectors measured using X-ray mapping." *SORMA* (2008)

[2]   Szeles, C., "Advances in the Crystal Growth and Device Fabrication Technology of CdZnTe Room Temperature Radiation Detectors." *IEEE Transactions on Nuclear Science,* vol. 51, no. 3, pp. 1242-1249 (2004).

[3]   W. R. Kaye, "Energy and Position Reconstruction in Pixelated CdZnTe Detectors," Ph.D. Thesis, University of Michigan, 2012.

PART III
CODED APERTURE IMAGING USING 3D CdZnTe ARRAYS

CHAPTER 7
BENEFITS OF 3D CdZnTe ARRAYS

Beginning in Fall 2010, the first Polaris array was assembled and utilized for coded aperture imaging. These detectors were selected for energy resolution, not uniformity or detector quality. Despite the fact that these detectors suffer from pixel jumping and other material defects, which degrade image quality, it has been shown that the use of multi-detector arrays can reduce the overall impact of these detrimental effects. This chapter highlights the benefits of applying coded aperture imaging to an array of 3D CdZnTe detectors. The work is based on the material from [1] and [2].

7.1 Improvement Due to Combined Images

In Chapter 5, it was shown that combining images from multiple detectors improves the overall image quality, even when individually each detector's resultant image is quite poor. This section highlights the extent of the improvement of coded aperture images when using an array of detectors.

Two large 32 × 32 random coded aperture masks were applied to both 3 × 3 planes of the first Polaris system, at a distance of 6 cm from the cathode sides, as shown in Figure 7.1. The mask elements are 3.44 mm × 3.44 mm to reduce effects of pixel jumping. The imaging code is modified to incorporate detectors from the nine-detector array and account for the larger element random mask. The geometry was modified to account for the differences in the detector-mask orientation so that both planes could be imaged.
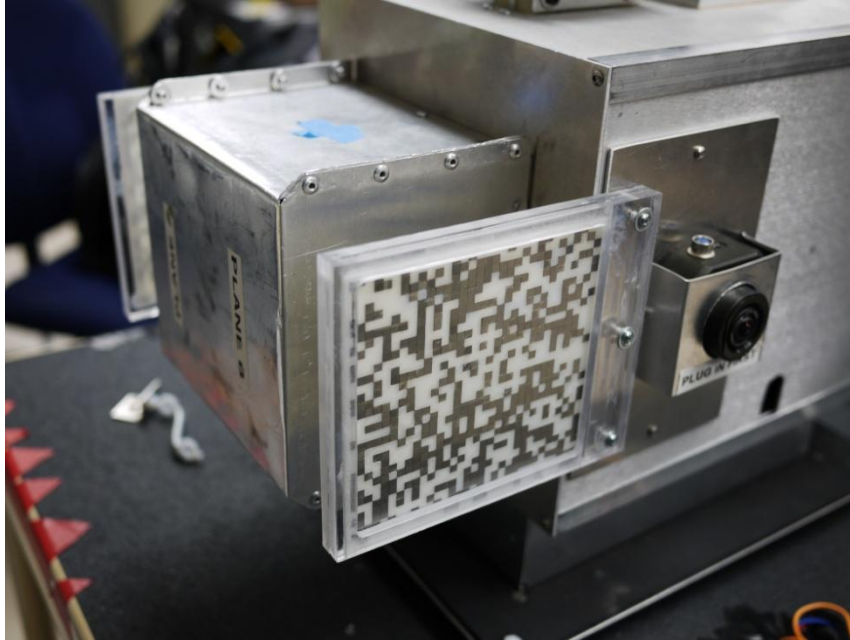
Figure 7.1: The first Polaris system assembled in Fall 2010. Two planes of 3 × 3 arrays of CdZnTe detectors located between two random masks, cathode sides facing outwards.

The more uniform of the two planes was used in this study. A 100 µCi Co-57 point source was placed in the far field, at various positions in the field of view. Since a strong source was used, images could be formed using measurement times on the order of minutes.

Images from all nine detectors of a single Polaris plane are combined for measurements at the various source positions in the field of view as shown in Figure 7.2. The combined images provide a clear hotspot in the source direction. The fluctuation in the background image, or sidelobes, is due to the nature of the random mask design.
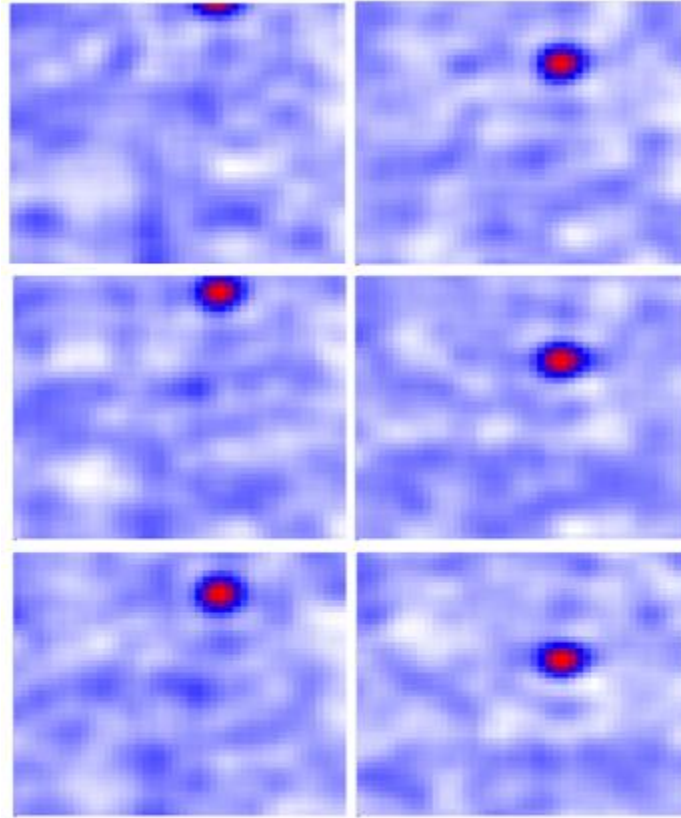
Figure 7.2: Images tracking a Co-57 (122 keV) source at various positions in the field of view using all nine detectors of a Polaris plane.

Pixel Jumping vs. Image quality

Since the detector uniformities of these nine detectors vary from one to the other (as shown in Chapter 6), it is expected that the images will also vary in quality, which is the case. To better understand the correlation between pixel jumping and its effects on image quality, measurements were taken using 26 unique detectors from two different Polaris systems. Images were reconstructed and were categorized into three types: the Good, the Bad, and the Ugly.

Good detectors are those whose largest sidelobe (hotspot in non-source direction) is less than 75% of the source intensity. The detector is considered Bad if the largest sidelobe is greater than 75% the source intensity. A detector is considered Ugly if the largest sidelobe is greater than the source intensity. This categorization is utilized to understand the relationship between pixel jumping and image quality.
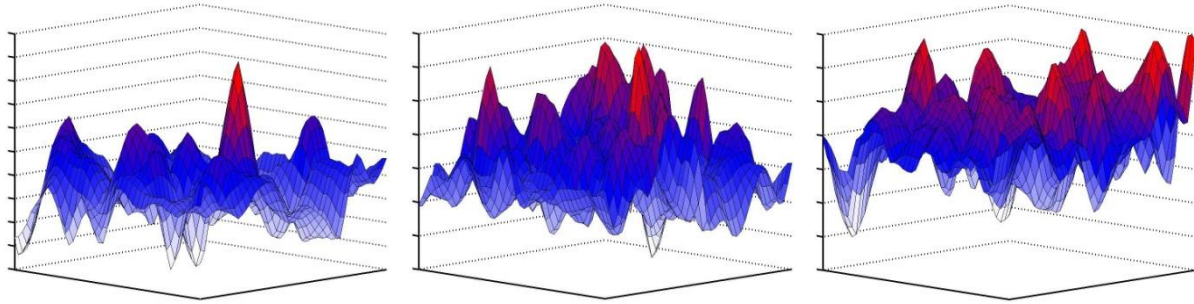
Figure 7.3: Image shown in 3D to demonstrate the relative intensity and fluctuation of the image sidelobes as compared to the hotspot formed by the source. Examples of coded aperture images from Good (left), Bad (middle), and Ugly (right) detectors.

The goal is to come up with a metric that can predict whether or not a detector will perform well without going through the trouble of imaging with it. In principle the uniformity of the count rate from pixel to pixel when the entire cathode surface is irradiated should indicate the degree of pixel jumping. Therefore, the standard deviation of the counts in each pixel was calculated for each detector based on data from a Co-57 flood irradiation with no mask. These standard deviation values are binned and shown for each detector quality grade in Figure 7.4. A trend can be noted; as expected, Good detectors are associated with more uniform count distributions, while Ugly detectors tend to have high pixel-to-pixel variance in the count rate.
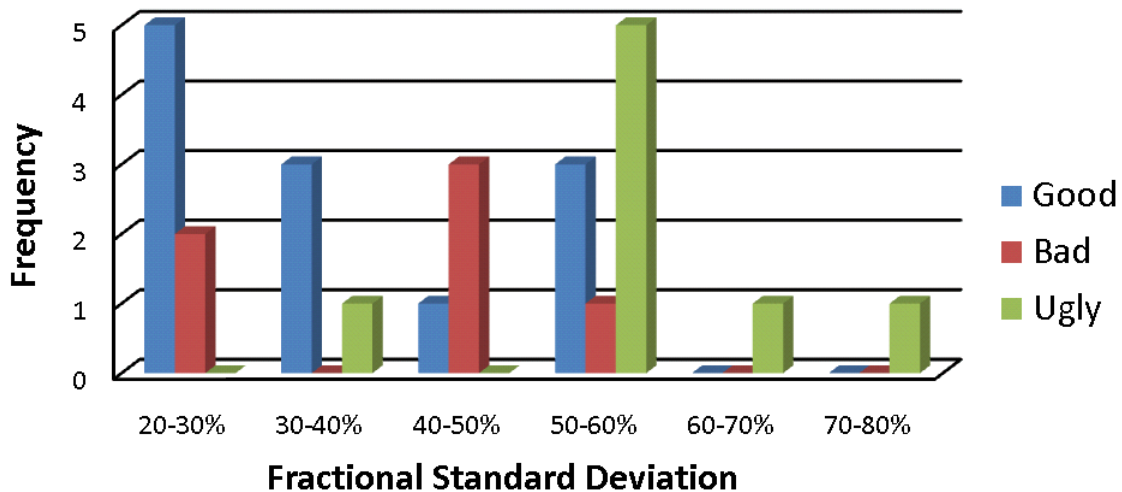
Figure 7.4: Correlation between image quality and count rate uniformity. The frequency of each image type is shown as a function of the standard deviation of the count rate under uniform Co-57 (122 keV) irradiation.

82

Benefits of Detector Arrays

Although the Bad and the Ugly images do not clearly identify a point source as the Good images do, generally they do possess a more intense spot in the source direction, as compared to image background. The sidelobes are in different directions for all detectors due to the nature of the random mask pattern, with an additional effect of pixel jumping. Because the hotspot which represents the source position is in a consistent direction, when the images are combined from multiple detectors in an array, the source intensity is amplified, while the fluctuating sidelobes in the image background are flattened. This results in the production of better images with a single hotspot, showing improved SNR. This is why when multiple Bad detector images are combined, the result is a Good image, as shown in Figure 7.5. When images from all nine detectors of a Polaris plane, including Good, Bad, and Ugly detectors, are combined, the SNR of the resultant image is much better than any individual detector in the array shown, as in Figure 7.6.
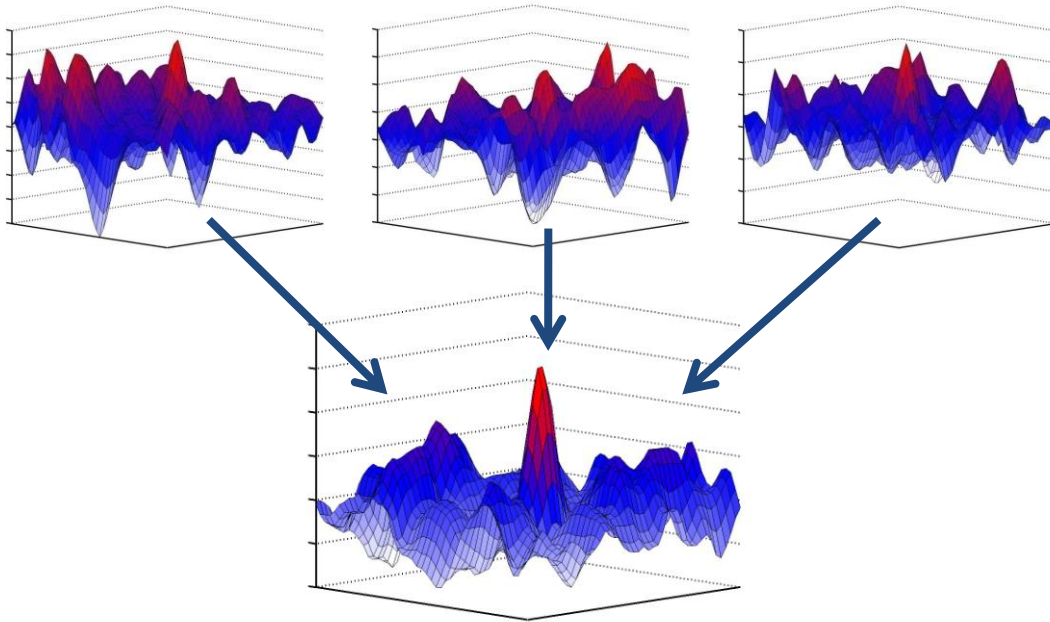
Figure 7.5: The combination of three Bad images (top) resulting in a Good image (bottom).
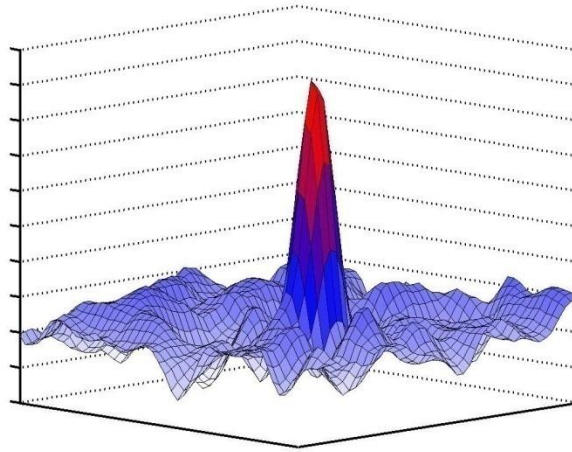
Figure 7.6: Improved CAI formed by combing images from all nine detectors from a single Polaris plane.

What this shows is that the benefit of using an array of detectors for coded aperture imaging goes beyond the improvement in efficiency. Systematic effects, such as pixel jumping that degrade the image quality in large volume CdZnTe detectors, are also improves. This is due to the fact that 1) a different part of the mask is being sampled, and 2) each detector is uniquely affected by pixel jumping. Both of these effects create a unique sidelobe pattern, especially when using a random mask. Thus, when multiple images are combined, the image in the source direction is amplified, while the background, or noisy sidelobes, tends to reduce in variability and flatten out. Even in the case of long count times, many detectors cannot independently form a coherent image. However, when images from several detectors are combined, the systematic biases are canceled out. This is not due solely to the best detector in the array, evidenced by a good image formed exclusively by poor detectors.

Benefit of Increased Counts

Even if the image is formed using all nine detectors, if a sufficient number of counts are not measured, the result will be a noisy image. To better understand the limits of the CAI using this system, measurements were taken with Ba-133 (80 keV, 356 keV), Co-57 (122 keV), and Cs-137 (662 keV). Figure 7.7 and Figure 7.8 demonstrate how increased measurement times or source strengths improves image quality. In Figure 7.7, Co-57 events that interact in the top 5 mm layer of the detector were imaged using a variable

84

number of counts. This is repeated for Ba-133 in Figure 7.8. Both images show an improvement in image quality when number of imaged counts is increased.
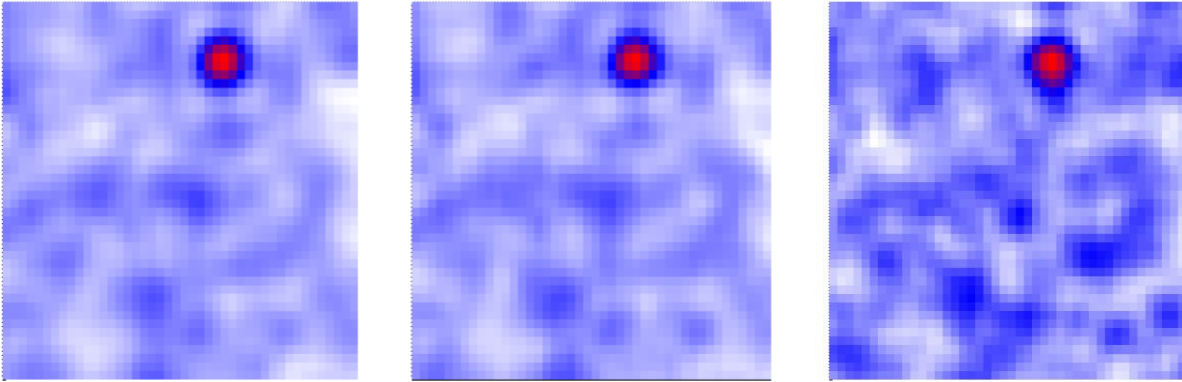
Figure 7.7: Co-57 images from all nine detectors combined for 8E5 counts (left), 3.6E3 counts (middle), and 360 counts (right).
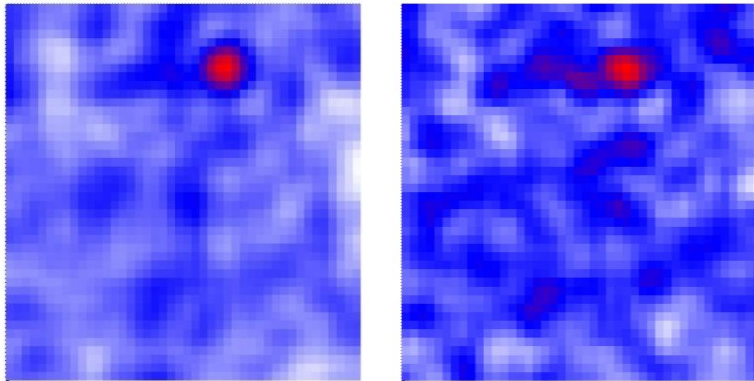
Figure 7.8: Ba-133 images from all nine detectors combined for 1.2E4 counts (left) and 1E3 counts (right).

Signal-to-Noise Ratio Analysis

The previous two sections demonstrated the improvement in image quality when increasing the number of counts and combining images from multiple detectors. This section quantifies the improvement using SNR analysis. The SNR is calculated as described in Appendix C. Measurements were performed using one of the two nine-detector planes and random coded aperture masks. An 80 µCi Co-57 (122 keV) source is placed at a distance of approximately 1 m from the detectors.

Figure 7.9 is a plot of SNR vs. the number of counts using a single detector and multiple detectors. In the top figure for a single detector, the baseline SNR is a function of the mask design optimization. The SNR has minimal improvement as the number of counts increases. However, in the bottom figure, which is a plot of SNR vs. the number of counts using images combined from a 3 × 3 array of detectors, the SNR increases as the number of counts increases. Images from each detector in an array contain large variations in image artifacts; when these images are combined, the artifacts tend to smooth out, while the peak intensity is amplified, improving the SNR.
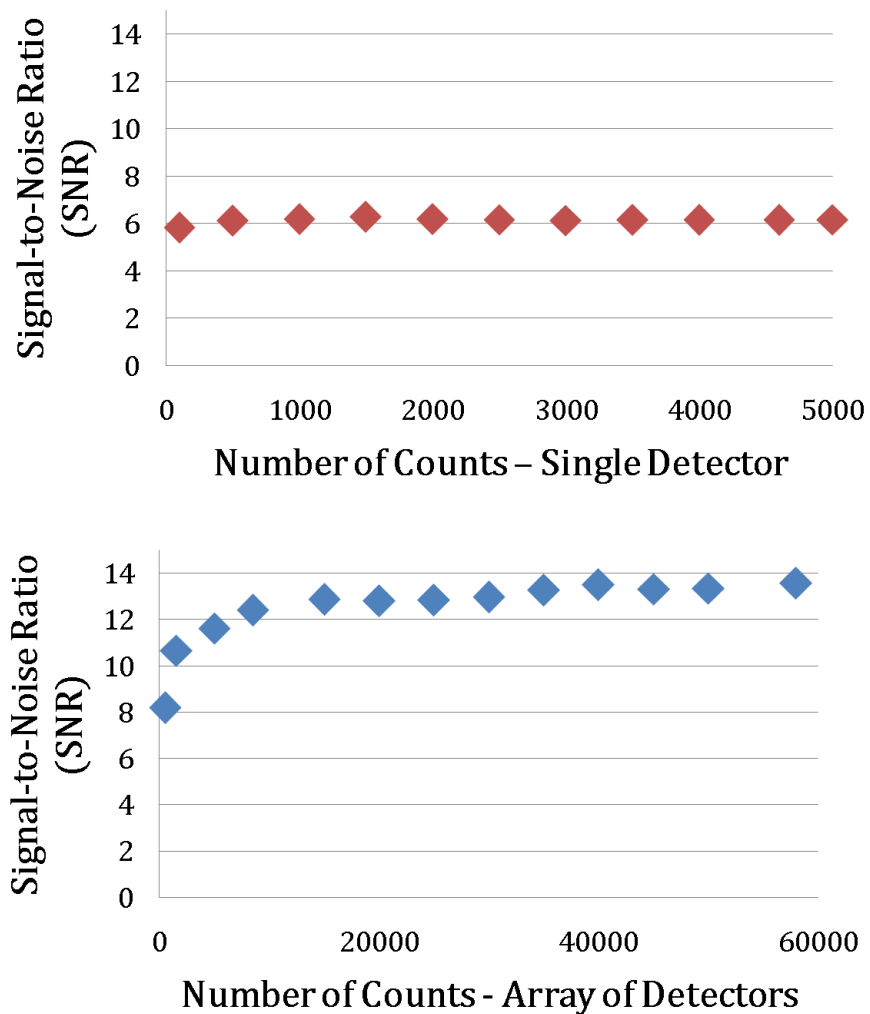
Figure 7.9: SNR vs. the number of counts using a single detector (top), and images combined from a 3×3 array of detectors (bottom).

In Figure 7.10, which is a plot of SNR vs. the number of detector images contributing to the final combined image, one can see that unlike the single detector case, the SNR steadily increases as the number of combined detector images increases, despite the fact that the same number of counts is used in each image. This improvement begins to fade at about five to six detectors, in this particular case.
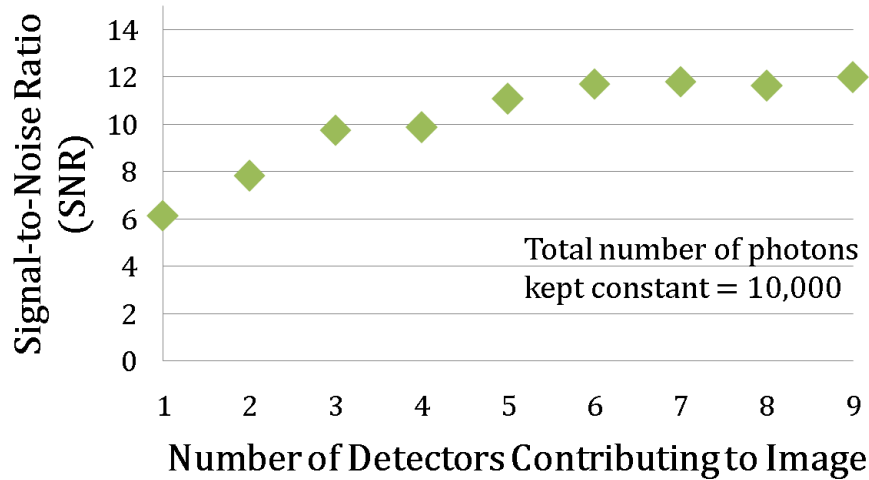
Figure 7.10: SNR vs. the number of detector images contributing to the combined image.

To understand the variation of SNR as a function of source direction, measurements were taken in five positions within the FCFOV. The SNR was calculated and reported as a function of X and Y position, relative to normal. The SNR stays relatively constant in both dimensions, as shown in Figure 7.11.
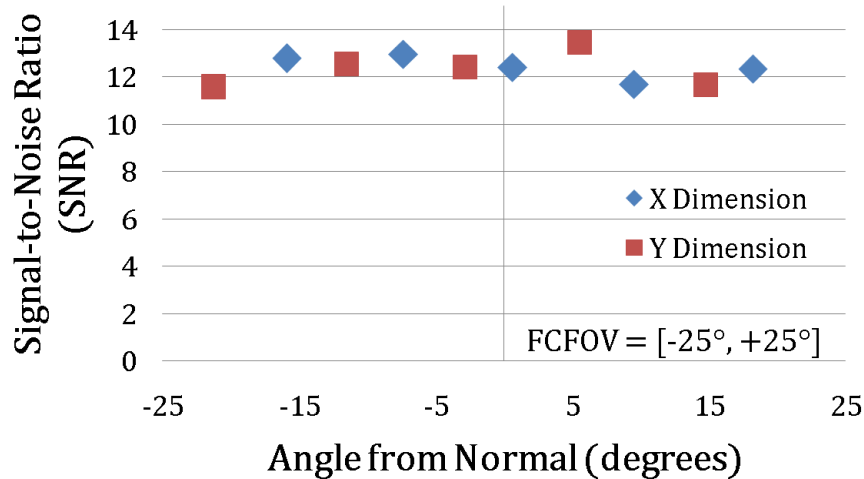
Figure 7.11: SNR vs. the source angle from the normal, spanning across the entire fully-coded field of view (FCFOV)

7.2 Improvement Due to Moving Sources

The concept of combining images for improved SNR can be extended further to two other cases: moving source and moving detector applications. This motion can be used to our advantage in the case of an imperfect detector and mask configuration with image artifacts. By averaging the images from multiple source or detector positions, the image intensity in the source direction will be unaffected, while the artifacts will be reduced significantly.

In theory, this motion compensated image will not only reduce the fluctuations due to non-uniformity of the detector material properties, but will also flatten the image sidelobes caused by the random mask design, thus improving the SNR of the source peak to background in the reconstructed image. The focus of these measurements is to validate this claim through measurement and simulation, and to ultimately automate this process given the coordinates and direction of the source, in the future.

Moving source imaging has been demonstrated for Compton imaging [3], and is extended to lower energies via coded aperture imaging. In a moving source scenario, the relative source positions must be considered, otherwise the images will be distorted. This movement can be used to our advantage. The individual images from different source positions may have varying image artifacts due to mask design and detector material

properties. The summation of each motion-compensated image provides a resultant image with improved signal-to-noise ratio with flatter sidelobes. The purpose of this work is to investigate the improvement in image quality using multiple source positions.

Measurements

For this analysis, measurements were performed using one of the two nine-detector planes and coded aperture masks. An 80 µCi Co-57 (122 keV) source is placed at a distance of 1 m from the detector. The source is moved to nine (9) discrete positions. The difference in angle of incidence between each position is 1.15°, relative to the center of the FCFOV.

For each source position, individual detector images are reconstructed and then combined. Before images from each source position can be combined, the images must be motion compensated, or else the image of the point sources will look like a large blur, as shown in Figure 7.12. This is done by modifying the geometry file for all eight positions so that the hotspots in the images overlap. For real world applications, the exact position of the sources must be known and this motion compensation will be automated.
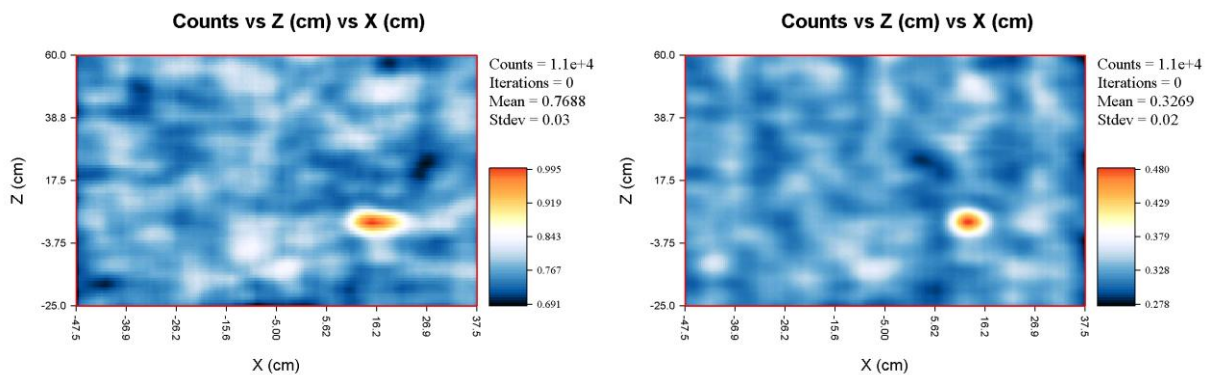
Figure 7.12: Summed images from all nine source positions without motion compensation (left), and with motion compensation (right).

Figure 7.12 also shows the result of combining images from two source positions, however, it is hard to quantify the reduction of sidelobes from a visual inspection of the image. Therefore SNR is used to evaluate image improvement for this study. At the time, the UMImaging code already incorporated real-time Compton imaging [4]. In addition to

implementing real-time CAI in the UMImaging code, a SNR feature is also added. Details on the SNR implementation can be found in Appendix C.

When combining images from position 0 and position 2, there is an increase in overall SNR, as compared to the individual images, even when using the same number of counts. Figure 7.13 showcases this slight improvement; the SNR improvement is not as drastic as seen when comparing a single detector image to an image formed by an array, or simply using good detectors in the first place. It is hypothesized that combining images from source positions that are further apart will provide a larger improvement.
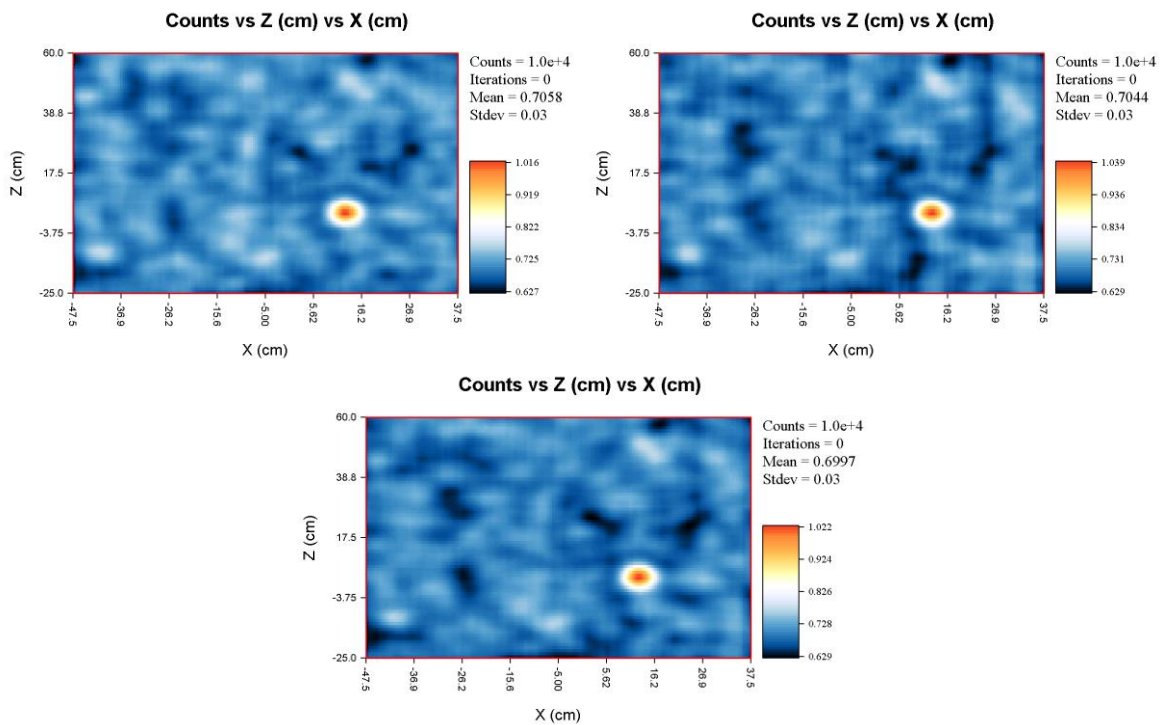
Figure 7.13: Image formed using 1E4 counts at position 0 (SNR = 13.44) (upper left), position 2 (SNR = 13.20) (upper right), and combined (SNR = 13.74) (bottom)

Sources of Image Degradation

There are various possible sources of image degradation including poor mask design, unmodulated background counts, and pixel jumping [5][6], all which introduce artifacts in the coded aperture image, as described in Table 7.1. Some solutions include the moving sources scenario, where the source is moving in space as a function of time; the moving detector scenario, in the case where the detector is being moved by the operator in

search of a stationary source; as well as combining images from multiple detectors in a single array [1].

Table 7.1: Causes of coded aperture image artifacts and possible solutions.

	Poor Mask Design Producing large sidelobes in the image	**Unmodulated Background** Counts that interact with the detector without passing through the mask	**Pixel Jumping** When an interaction occurs under one pixel and the electron cloud is collected by another pixel
Moving Source Summing images of multiple source positions after motion compensation. Source is moving. Detector and background are stationary. Using simple motion compensation technique.	MUCH IMPROVEMENT: (observed) Moving the source utilizes multiple realizations of the mask, which maintains the signal, while averaging out the artifacts.	SOME IMPROVEMENT: (expected) Unmodulated counts will be projected through a different region of the mask, which may tend to average out the artifacts.	SOME IMPROVEMENT: (observed) May slightly improve images from detectors suffering from pixel jumping affect, by averaging out the artifacts.
Moving Detector Summing images of multiple detector positions after motion compensation. Detector is moving. Source and background are stationary.	MUCH IMPROVEMENT: (expected) Moving the detector will improve the SNR as the source is being modulated by different regions of the mask.	SOME IMPROVEMENT: (expected) Summing images from multiple detector positions may average out artifacts due to unmodulated background that is non-uniform.	SOME IMPROVEMENT: (expected) May slightly improve images from detectors suffering from pixel jumping effect, by averaging out the artifacts.
Multiple Detectors An array of detectors are utilized to improve efficiency.	MUCH IMPROVEMENT: (observed) Summing images from multiple detectors provides improved SNR, as a larger number of mask elements are used.	SOME IMPROVEMENT: (expected) The unmodulated background counts will increase at about the same rate as the source.	MUCH IMPROVEMENT: (observed) More pixels means more realizations of pixel jumping, which tend to average out artifacts relative to the increased source intensity.

The moving source correction is useful in scenarios where sources are continuously moving in space and the source position and/or direction is known. This movement can be utilized to improve the image quality in two ways: increased efficiency by combing multiple images, and improved SNR by sampling various parts of the mask.

To quantify the impact of combining multiple source positions, the relative improvement is calculated. This is done by taking the difference between the SNR of the

combined image from all source positions and the average SNR of the image from individual source positions, all divided by the average SNR.

$$Improvement = \frac{SNR_{sum} - SNR_{avg}}{SNR_{avg}} \qquad (7.1)$$

The improvement is calculated for combinations of various number of source position. Each image is created using 10,000 counts for consistency. Figure 7.14 shows that the maximum improvement is achieved by combing all five source positions, but this improvement tapers off at about four images, in this particular case.
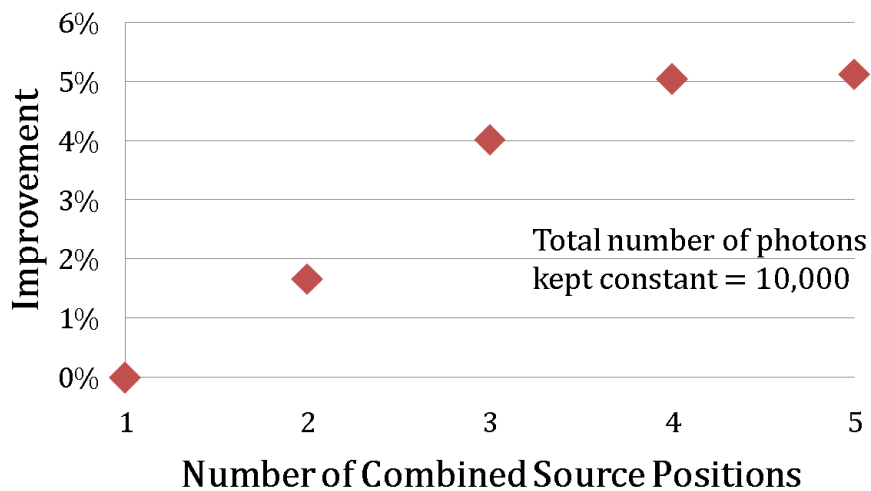
Figure 7.14: Relative SNR improvement vs. the number of combined source positions.

Lastly, pairs of images are combined to determine the optical angular difference between two source directions to give the best percent improvement. Three of the source directions (angle of incidences) are selected: 0°, 1.15°, and 2.30°. Images from these three source directions are individually combined with images from its four neighboring source directions, and the percent improvement is calculated.
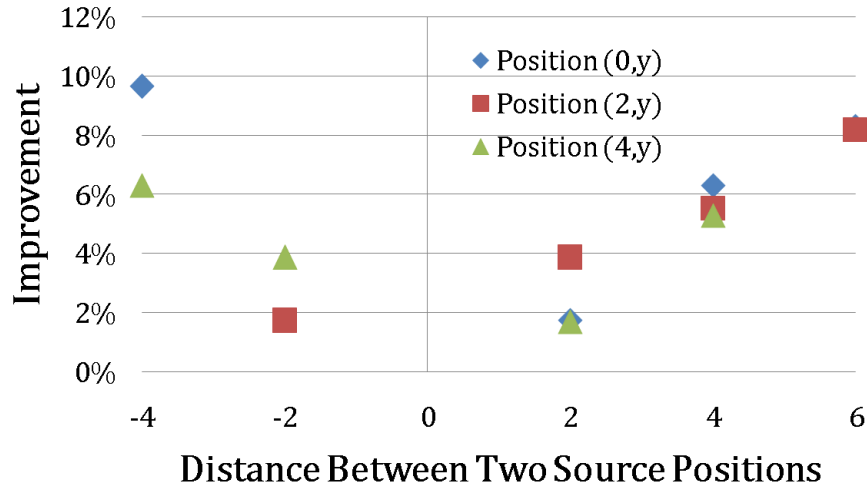
Figure 7.15: Improvement vs. the difference in angle of incidences (degrees). The percent improvement is calculated after individually adding images of three source directions (0°, 1.15°, and 2.30°) with images of four other possible directions. These results show that the percent improvement increases as the difference in angle of incidence between the two source directions increases. All measurements were taken at a constant y coordinate.

From Figure 7.15, one can see that the best percent improvement occurs when combining images with the largest difference in angle of incidence. This is due to the fact that the larger the difference, the greater the variation in the mask shadow cast on the detector. Thurs, adding two images with the largest variation in image artifacts results in the greatest percent improvement. Nonetheless, the improvement is very slight compared to the improvement due to the use of detector arrays and sufficient counts in the detector.

7.3 Conclusions

There are many causes of coded aperture image degradation including non-ideal mask design and detector geometry, counts due to unmodulated background, as well as non-uniform material properties that cause pixel jumping. Image improvement has been demonstrated through combining individual detector images using a multi-detector array, and images from multiple source positions.

The measured results show that the more images combined from a multi-detector array greatly improves SNR. Even when Bad detectors individually cannot distinguish the source direction from background, when a few images from detectors of this sort are

93

combined, the result is a Good image that pinpoints the source direction. This is due to the fact that the image background is flattened, while the source direction is amplified.

When images were combined from multiple source directions, the result was a slight improvement in SNR. The largest improvement arose from the combination of images from the most extreme source directions within the FCFOV, resulting in the largest improvement.

However, the SNR improvement due to the moving source scenario is very slight compared to the use of multi-detector arrays and sufficient detector counts. Practical implementation is necessary for real world application of the moving source case. Due to the fact that improvement was slight, and implementation efforts are great, further investigation may not be an efficient use of time.

7.4 References

[1] Joshi Kaye, S.; Kaye, W.R.; He, Z., "Experimental Limitations of Coded Aperture Imaging Using Thick 3D-Position-Sensitive CdZnTe Detectors," *Nuclear Science Symposium Conference Record (NSS/MIC)* (2010).

[2] Joshi Kaye, S.; Jaworski, J. M., Kaye, W. R., He, Z., "Source Motion Compensated Coded Aperture Imaging Using Thick 3D-Position-Sensitive CdZnTe Detectors," *Nuclear Science Symposium Conference Record (NSS/MIC)* (2011).

[3] Jaworski, J. M., C. G. Wahl, W. Wang, J. A. Fessler, Z. He, "Model-based reconstruction of spectral and spatial source distribution from objects with known motion," *Nuclear Science Symposium Conference Record (NSS/MIC)* (2010).

[4] Wahl, C. G., J. M. Jaworski, and Z. He, "UMImaging: A Software Package for Imaging Reconstruction From 3D-Position-Sensitive Gamma-Ray Detectors," *IEEE Transactions on Nuclear Science,* vol. 59, no. 4, pp. 1672-1680 (2012).

[5] A. E. Bolotnikov, S. Camarda, Y. Cui, A. Hossain, G. Yang, H. W. Yao, and R. B. James, "Internal electric-field-lines distribution in detectors measured using X-ray mapping." *SORMA* (2008)

[6] Szeles, C., "Advances in the Crystal Growth and Device Fabrication Technology of CdZnTe Room Temperature Radiation Detectors." *IEEE Transactions on Nuclear Science,* vol. 51, no. 3, pp. 1242-1249 (2004).

CHAPTER 8

CURRENT POLARIS ARRAY

The previous chapters demonstrate the feasibility of coded aperture imaging using 3D position sensitive CdZnTe detector arrays. The goal of this thesis is to seamlessly extend gamma-ray imaging to lower energies. The focus of this chapter is to reveal the state of coded aperture imaging as applied to the current 18-detector Polaris system. The work is based on the material from [1].

8.1 System Geometry

As described in Chapter 2, the current Polaris system consists of two 3 × 3 CdZnTe arrays. The cathode sides face outwards partly to reduce the attenuation of low energy gamma rays before reaching the detector material, but primarily because the anode dead layer of approximately 3 mm thickness reduces the effectiveness of coded aperture imaging.

Figure 8.1: Polaris II system with two 32 × 32 random masks applied to each 3 × 3 array of detectors.

A 32 ×32 array coded aperture mask is applied to both arrays. The mask elements are 3.44 mm × 3.44 mm, twice the dimensions of the detector pixels to reduce the effects of pixel jumping. The mask design was originally a random pattern due to concerns that the 2 mm gap between detectors would add significant noise to the image, and is now a MURA pattern, which provides improved SNR.

8.2 Imaging Algorithm

Coded aperture imaging algorithms were originally implemented and tested in MATLAB. Since low-energy imaging was to be seamlessly integrated with the currently implemented Compton imaging, event-by-event coded aperture imaging was integrated into the imaging software known as UMImaging. UMImaging is a code developed at the University of Michigan, which is used to image both measured and simulated data for any detector geometry and material composition. Detector geometry and event data, including gamma-ray interaction position, time, and energy deposition, is streamed from the detector system to UMImaging in real time to allow for near real-time imaging [2].

CAI integration with UMimaging not only allowed for real-time imaging, it also opened up the possibility for using different imaging tools previously implemented by other students, and for the implementation of a signal-to-noise ratio (SNR) calculation, which was critical for the study presented in Chapter 7. Most importantly, the integration made combined coded aperture – Compton imaging possible. This ultimately lead to optical image overlay, enabling real-time search and location of low-energy sources.

8.3 Image Characteristics

As the Polaris system evolved, the geometry also changed and improved. The primary difference in the coded aperture geometry between the past system and the current system is the mask-to-detector distance. The mask distance was decreased from 7 cm to 4.5 cm, such that the FOV increased from 30° to 50° in both dimensions. However, this modification came at a price, worsening angular resolution from 4° to 7°. This was a small price to pay given the drastic enlargement of the FOV, especially when considering

SBP Compton imaging resolution is about 40° (at best 20° using inter-module events). The difference in FOV and angular resolution can be noted in Figure 8.2.
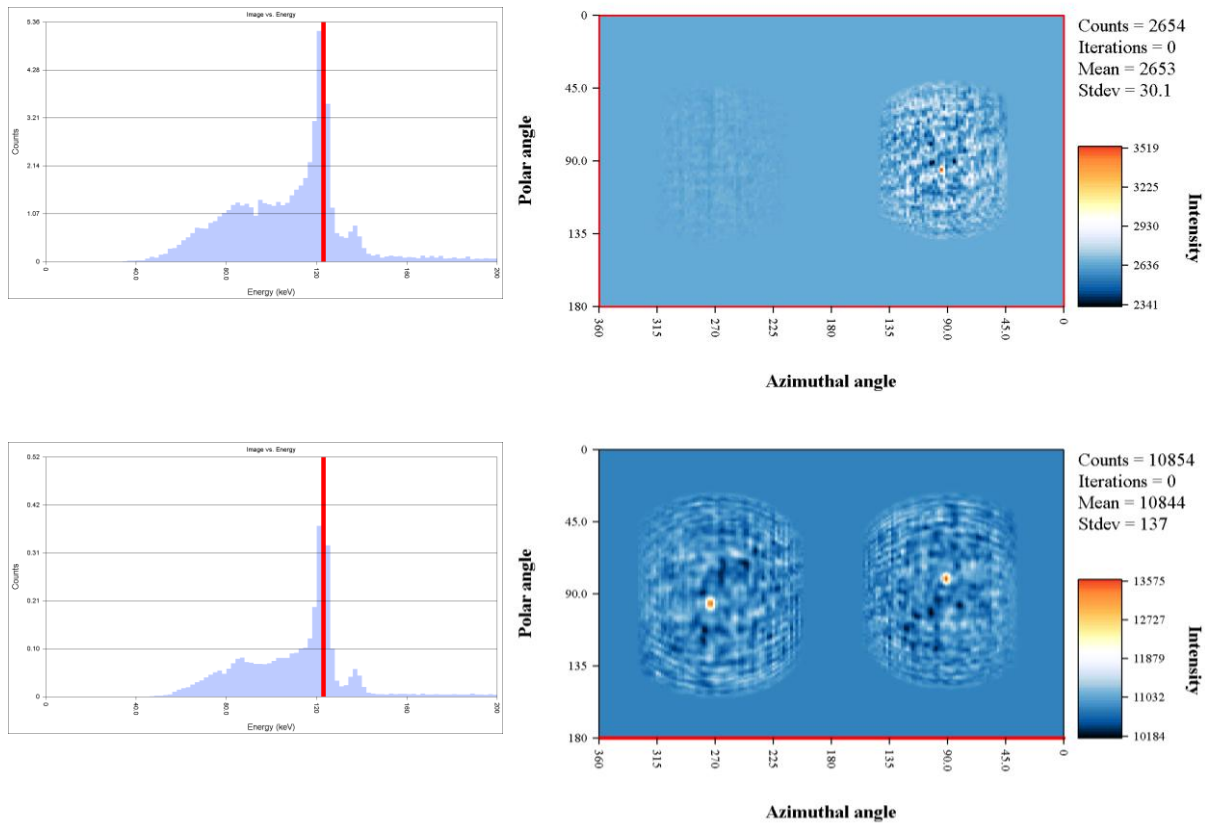
Figure 8.2: Comparison of CAI of Co-57 (122 keV) point source using Polaris I (top) vs. Polaris II (bottom). The decreased masked distance improved the CAI FOV, while worsening angular resolution.

Typically, the Polaris CAI algorithm performance is evaluated using a low-energy source over the background inherent to the laboratory, which is relatively low compared to most real-world measurement scenarios. Image degradation due to CAI of a peak over continuum was studied. A Co-57 (122 keV) source was placed in the same direction as a Cs-137 (662 keV) source. The Co-57 peak is located over the Cs-137 continuum as shown in Figure 8.3 and shows slight degradation in the image. This is not a fair comparison as the Cs-137 source is four times weaker than the Co-57 source. This experiment is repeated when demonstrating combined coded aperture and Compton imaging in Section 8.4.
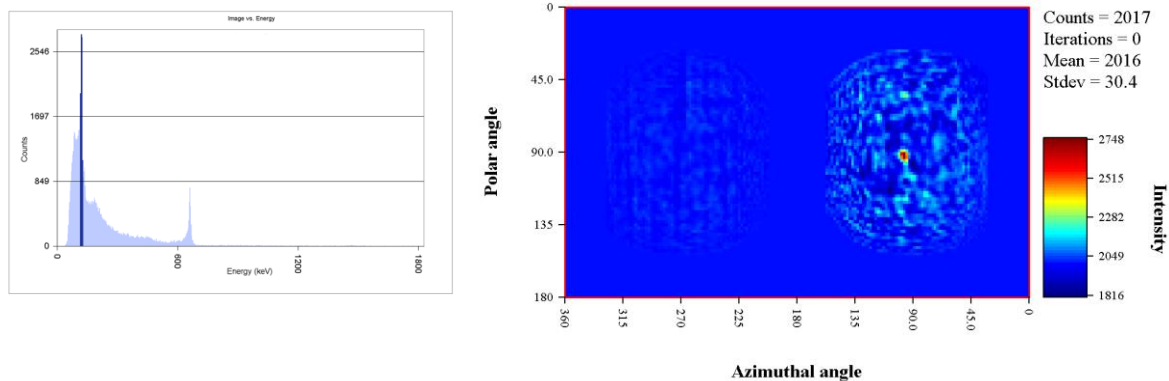
Figure 8.3: Image of low-energy (Co-57) source over high-energy source (Cs-137) continuum.

Continual improvement of energy resolution is a fundamental goal of the Polaris project. The fact that the Co-57 peak can be easily identified over the Cs-137 continuum is due to energy resolution of 3D CdZnTe. This is due to the fact that fine energy resolution improves both detection of sources over background and isotope identification, which leads to improved image SNR.

8.4 Combined Coded Aperture – Compton Imaging

The main justification of applying CAI to the Polaris system was to seamlessly extend gamma-ray imaging to low energies. Until now, CAI had been demonstrated as a standalone imaging technique. The combination of both imaging modalities must be done in real time for deployment purposes. Coded aperture and Compton imaging are inherently complementary imaging modalities spanning the system's dynamic range. Currently, a simple summation of the two images is done. The effortless transition between both techniques has made it possible for the device to be field tested.

A spatial calibration is performed lining up the optical cameras, Compton imaging, and CAI images. This is necessary since the exact alignment of the coded aperture mask and detector plane is unknown. A technique is used to correct this by placing low and high energy sources in various positions in the FOV. The geometry file is modified until these sources line up both via gamma-ray imaging and optical imaging modalities, ensuring that the source directions match well.

Once the calibration is completed, a measurement of Co-57 (122 keV), Na-22 (511 keV), and Cs-137 (662 keV), positioned in the same direction relative to the detector system. First a coded aperture image is reconstructed for the low-energy source, shown in Figure 8.4. The hotspot is magnified to give perspective of the angular resolution. Next, the Compton image is created using the Na-22 and Cs-137 peaks shown in Figure 8.5. Here it becomes obvious that the coded aperture angular resolution is much better as compare to Compton imaging, of 7° and 40°, respectively. Finally, in Figures 8.6 both coded aperture and Compton images are combined, and with optical overlay shown in Figure 8.7.
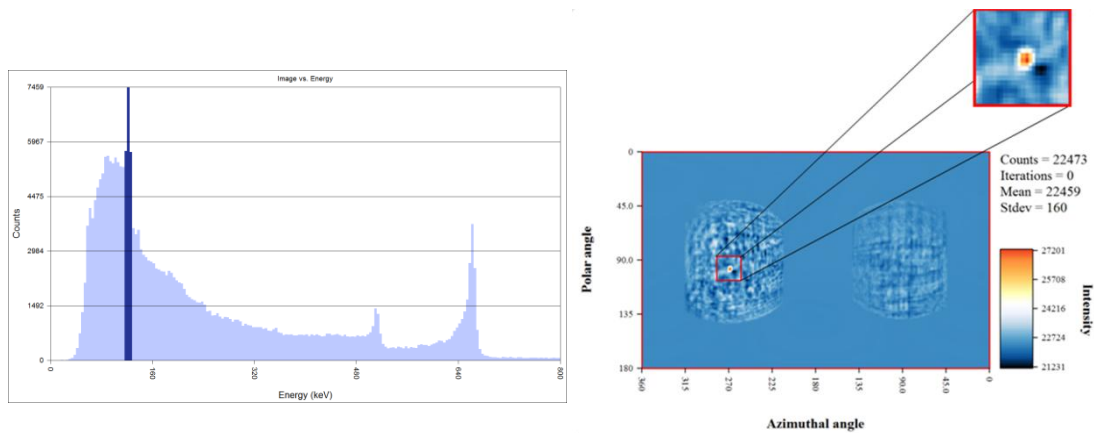
Figure 8.4: Coded aperture image of Co-57 over Na-22 and Cs-137 continuum. All three sources are positioned in the same direction.
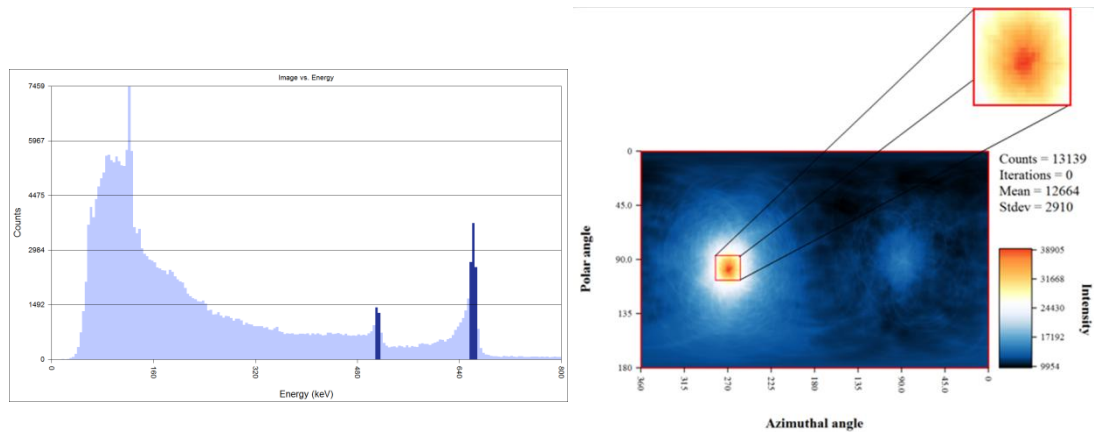
Figure 8.5: SBP Compton image of Na-22 and Cs-137. All three sources are positioned in the same direction.

99
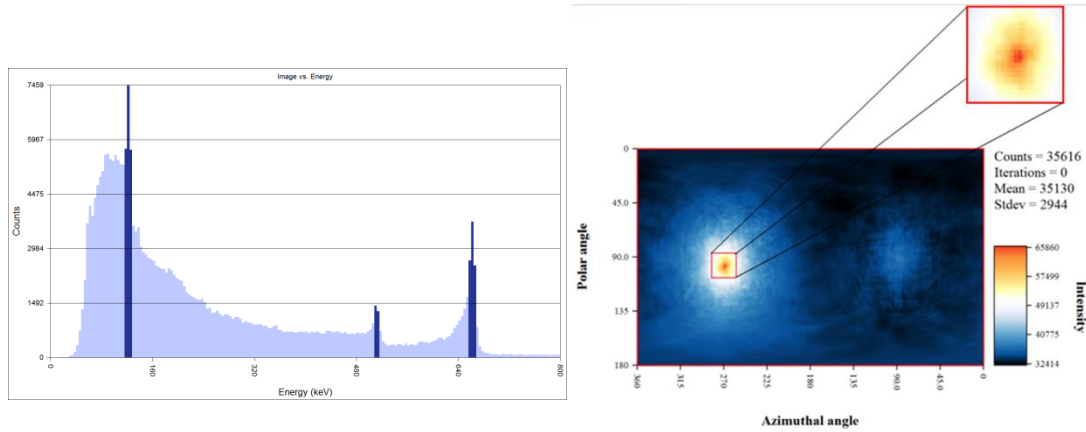
Figure 8.6: Combined coded aperture and Compton image of Co-57, Na-22, and Cs-137. All three sources are positioned in the same direction.
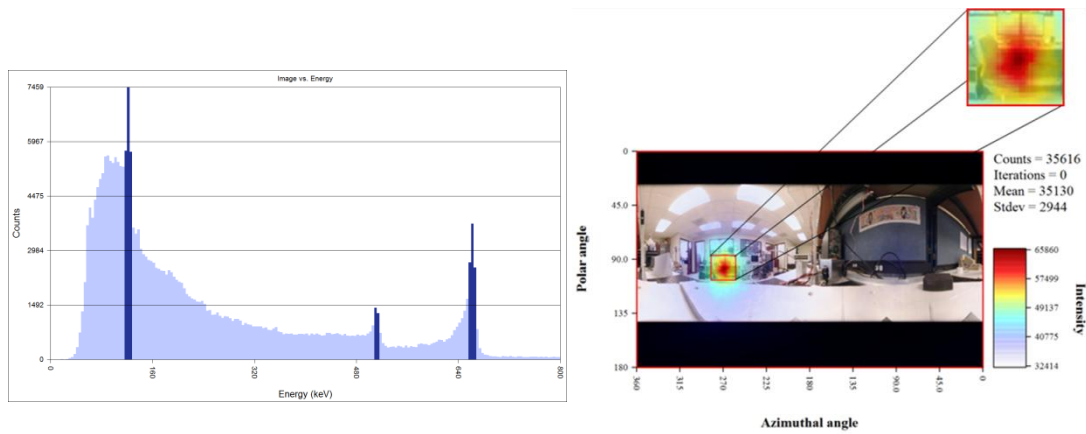
Figure 8.7: Combined coded aperture and Compton image of Co-57, Na-22, and Cs-137, now with optical overlay. All three sources are positioned in the same direction.

Currently both coded aperture and Compton images are simply summed together. However, probabilistic models should be investigated in the future such that only single-event full energy depositions are considered for coded aperture imaging. Also, to truly extend imaging to all directions such that there are no blind spots, coded aperture masks must be applied to all sides of the detector system.

8.5 Future work

Coded aperture imaging has successfully been demonstrated using an array of 3D position sensitive detectors as shown in this chapter. Multiple point sources of the same

energy can be imaged and located in a short amount of time even using weak check sources. But of course, there are many improvements that can be made.

One would be to eliminate the blind spots to low-energy gamma rays by extending CAI to all directions by adding masks to all sides of the detector system. Measurements could be made using extended sources (line, volume, etc.) to determine the limits of the system, such that mask parameters, such as mask thickness and open-closed fraction, are optimized accordingly. And lastly, probabilistic methods could be used to improve the combination of both imaging modalities. This could be done by developing a system model for maximum likelihood that simultaneously considers presence of the coded aperture and the kinetics of Compton scatter or by using a method that accounts for the relative information content of each modality prior to combining the images [3]. Nonetheless, the goal of this project was met, and a device which images low-energy gamma rays has been successfully delivered to government sponsors.

8.6 References

[1]   Joshi Kaye, S.; Jaworski, J. M., Wahl, C. G., Kaye, W.R., He, Z. "Coded aperture gamma-ray imaging using 3D position-sensitive semiconductor radiation detectors for nuclear security applications," *Institute of Nuclear Materials Management (INMM) Annual Meeting* (2011).

[2]   Wahl, C. G., "Imaging, Detection, and Identification Algorithms for Position-Sensitive Gamma-Ray Detectors," Ph.D. Thesis, University of Michigan, 2011.

[3]   Smith, L.E., C. Chen, D. K. Wehe, Z. He, "Hybrid collimation for industrial gamma-ray imaging: combining spatially coded and Compton aperture data," *NIMA* 462 (2001) 576-587.

CHAPTER 9

CONCLUSIONS/FUTURE WORK

The purpose of this work is to extend gamma-ray imaging to low energies for 3D position sensitive CdZnTe detectors. By applying coded aperture imaging, the Polaris system now has the capability to not only detect, but also locate and characterize low-energy gamma ray sources. As this is just a first attempt at applying CAI to thick 3D position sensitive CdZnTe detectors, the work presented in this thesis only scratches the surface of its capabilities and limitations. There are many topics that were touched upon and should be revisited, and many ideas that were conceived but never fully investigated. This chapter summarizes the work that was presented in this thesis, as well as poses possible research questions and future directions, concluding with some closing thoughts.

9.1 Summary

This thesis demonstrated a solution to the need to extend gamma-ray imaging to lower energies where photoelectric absorption is the dominant interaction mechanism in CdZnTe material. These single-pixel interactions were imaged by implementing coded aperture imaging. This was first done by theoretically demonstrating the feasibility through simulations, then through measurements. Masks were applied to the cathode and non-cathode sides of the detector to show that imaging was indeed possible. However, in the process it was discovered that material properties, such as pixel jumping and non-uniform electric fields, limit the quality of images. These properties were studied in further detail, showing that detector pixels are non-uniform in size, and that substantial improvement in image quality would require application of novel measurement and algorithmic techniques, which may not be feasible if such a system were to be mass produced.

Next, the use of an array of detectors to improve image quality was investigated, showing that although individually detectors with pixel jumping and poor uniformity

cannot pinpoint the source direction, that the combined image from multiple detectors provides a much improved SNR. Also, the moving source scenario was studied, where images from multiple source positions are combined to improve image quality. However, what was found is that the improvement is slight compared to the improvement due to the use of multiple detectors.

Finally, the state of the current Polaris system was presented. Coded aperture imaging was applied to the two detector planes, imaging multiple point sources in the field of view (FOV) using a random and MURA mask. Combined coded aperture – Compton imaging is shown, with improved angular resolution and overlaid on an optical image.

9.2 Future Work

Through the study of the application of CAI to thick 3D CdZnTe detectors, there were areas that were touched upon that could be further studied and/or improved. The most relevant work for further investigation is highlighted here:

1) Variable pixel size accountability – A method could be developed to measure and account for the cross-sectional variation in pixel size as a function of depth. This could be done through measurement to characterize the properties of the detector, through algorithmic corrections to more accurately determine the actual gamma-ray interaction position before events are reconstructed.

2) Optimize mask design for extended sources – Given that sources are more likely to be extended in nature (rather than point sources), and are often located in the near field, the mask design should be optimized to image line, volume, and sources which span larger fractions of the FOV. This includes parameters such as the fraction of open to closed mask elements.

3) Multiple detectors to locate and characterize sources in 3D space – With the use of two or more detector systems, sources can be reconstructed in 3D space. This can be done in two ways. The first is to perform 2D reconstruction (as currently implemented), and use the relative orientations of the detector systems to determine the intersection of the 2D source directions, which results in a source position in 3D space. An alternate method is to begin with a 3D image mesh and

perform backprojection into 3D space itself, as has been implemented for Compton imaging [1].

4) Digital ASIC CAI – The digital ASIC provides improved interaction position resolution, even smaller than the pixel size [2]. This is done by using the transient signals produced on the eight neighboring pixels of the collecting pixel (pixel under which the interaction occurs). These signals can be used to provide the user with a more precise interaction position, allowing for the use of smaller mask elements. Given this sub-pixel resolution, it would be worthwhile to determine to what extend the improved position resolution would improve angular resolution.

5) Extend CAI to 4-pi – Currently, the implemented CAI is only possible within a limited FOV. For seamless transition between high and low energy gamma-ray imaging, 4-pi CAI must be implemented to match Compton imaging space. Based on the findings in Chapter 6, before this can be implemented, non-cathode side imaging must be studied in further detail. Also, explore statistical and iterative methods for combining Compton imaging and CAI [3].

The strength of CAI with 3D position sensitive CdZnTe is that it provides high resolution in both the spectral and spatial domain. It is best suited for use when the presence of radiation is known and further characterization of the source type and extent is necessary. Future work should continue to improve the system's capability to help the user learn more about an object. The aforementioned research areas should be considered by future students or members of the community to further improve coded aperture imaging with 3D position sensitive CdZnTe detectors.

9.3 Conclusions

The main purpose of this thesis is to inform the research community, as well as future University of Michigan students, about the steps that were taken to make coded aperture imaging possible for the Polaris system. A CAI system was successfully built to extend gamma-ray imaging to lower energies for 3D CdZnTe detectors. The Polaris system now has the ability to real-time image gamma rays extending from 30 keV to 3 MeV through dual modalities with both good energy and angular resolution, making it an

excellent candidate for various applications. The use of thick CdZnTe detectors increases efficiency, making it even better candidate for handheld systems. Its capabilities have been demonstrated by users at various nuclear security and government facilities, and have the potential to make an immediate impact in many fields, including nuclear and homeland security, emergency response, health and medical physics.

In many ways, the process of developing this system has unraveled more questions than it has answered. But in many ways this is only the beginning, as next generation of readout technology will enable a whole new era of high-resolution coded aperture imaging. As systems become faster, more efficient, compact, durable, it is incredible to imagine what future generations will invent based upon the technology that has been developed today.

9.4 References

[1]   Jaworksi, J. M., Z. He, "3D Compton imaging reconstruction using a moving 3D-position sensitive room-temperature CdZnTe detector array," *Nuclear Science Symposium and Medical Imaging Conference (NSS/MIC), 2011 IEEE*, pp.976,981 Oct. 2011.

[2]   Zhu, Y., S. E. Anderson, Z. He, "Sub-Pixel Position Sensing for Pixelated, 3-D Position Sensitive, Wide Band-Gap, Semiconductor, Gamma-Ray Detectors." *Nuclear Science, IEEE Transactions* vol.58, no.3, pp.1400, 1409, June 2011.

[3]   Smith, L.E., C. Chen, D. K. Wehe, Z. He, "Hybrid collimation for industrial gamma-ray imaging: combining spatially coded and Compton aperture data," *NIMA* 462 (2001) 576-587.

APPENDICES

APPENDIX A

Aperture Generator Code

An aperture generator code was programmed in C++ to create mask designs of various types and sizes, including random pattern and MURA. A random mask was simply created using a random number generator (RNG). The RNG generates a number between 0 and 1. Given a fixed open-closed mask element fraction of 50/50, if the number is great than or equal to 0.5 it is considered open, otherwise considered closed. This is repeated for each element in the mask. Figure A.1 shows an example of a 14 × 14 random pattern.
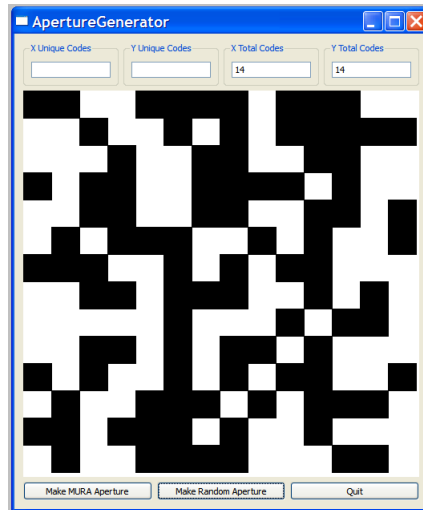
Figure A.1: An example of a 14 × 14 random array.

An algorithm was used to generate the MURA pattern. The variable, p, is the dimension of the array, for example, in the case of a 5 × 5 MURA base pattern, the variable p = 5. The following operations are performed for mask element k = 0 to p-1, shown in Table A.1. C_i and C_j represent the x and y coordinates of the mask. C_k is the product of these two

values. This value is then used to determine the mask element value, either 0 or 1. The 5 × 5 MURA base pattern case is demonstrated in Table A.1.

Table A.1: Operations performed to generate MURA base pattern

k	k²	k² % p	C_k
0	0	0	1
1	1	1	1
2	4	4	-1
3	9	4	-1
4	16	1	1

Then the map is determined using the following algorithm:
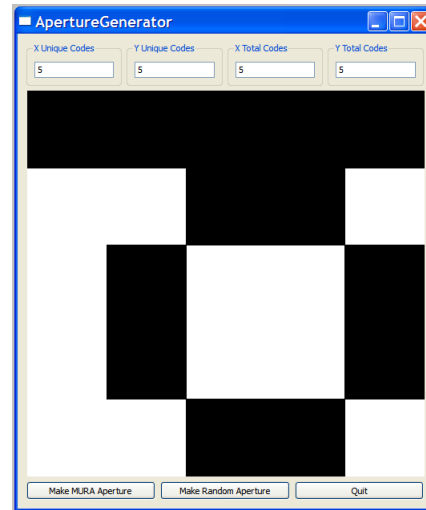
```
for all values where j = 0,        mask value = 1;
      if  I = 0 and j != 0,        mask value = 0;
      if  Cᵢ × Cⱼ = +1,            mask value = 0;
      if  Cᵢ × Cⱼ = -1,            mask value = 1;s
```

This results in a pattern as shown in Figure A.2.



Figure A.2: 5 × 5 MURA base pattern generated by the algorithm.

Given this 5 × 5 MURA base pattern, a 2 × 2 mosaic is created, as shown in Figure A.3.
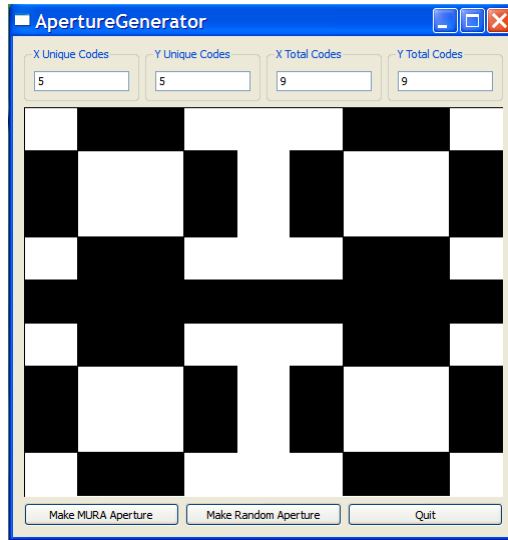
Figure A.3: 5 × 5 MURA base pattern in 2 × 2 mosaic pattern.

In scenarios where more mask elements are necessary, a larger array is generated. A 211 × 211 MURA base pattern is generated using the code, and arranged in a 2 × 2 mosaic, shown in Figure A.4. The open and closed pixels can be translated to 1s and 0s, which is used as the input for UMImaging geometry file, simulation codes such as Geant4 and MCNP, as well as to generate the mask holder in SolidWorks.
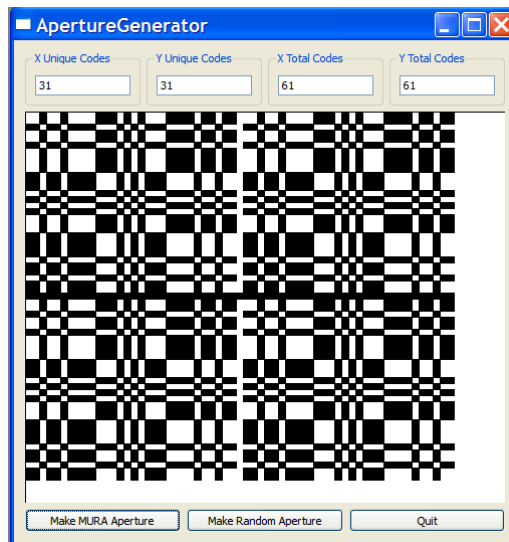
Figure A.4: 211 × 211 MURA base pattern in 2 × 2 mosaic pattern.

APPENDIX B

Image Reconstruction Algorithm

The post-processing CAI simple back projection (SBP) algorithm is straightforward, and can be described by the following pseudocode:

```
for each detector (D)
     for each detector pixel (d)
          for each image pixel (i)
               calculate the vector which connects the detector pixel
               (d) and image pixel (i),

               determine if the mask element  through which this
               vector passes is open or closed,

               project the detector pixel on to the mask plane along
               this vector, then calculate the fraction of the
               detector pixel area that is exposed to an open mask
               element,

               add this value to image pixel (i).
          end

          normalize the image to 1
          multiple by the number of counts in detector pixel (d)

     end

end
```

The algorithm was modified slightly for real-time, event-by-event CAI:

```
for each event (e)

      for each image pixel (i)

            calculate the vector which connects the detector pixel (d)
            position of event (e) and image pixel (i),

            determine if the mask element  through which this vector
            passes is open or closed,

            project the detector pixel on to the mask plane along this
            vector, then calculate the fraction of the detector pixel
            area that is exposed to an open mask element,

            add this value to image pixel (i).

            end

      end

end
```

APPENDIX C

Signal to Noise Ratio Calculation

The signal-to-noise ratio (SNR) is a common metric used to quantify the quality of an image. There are various ways to calculate SNR. For this analysis, SNR is defined as:

$$SNR = \frac{S - \mu_{Bkgd}}{\sigma_{Bkgd}} \quad (C.1),$$

where, S is the signal or the hottest spot in the coded aperture image, and σ_{Bkgd} is the standard deviation of the background, where the background is considered to be the region outside of 2.5 × FWHM.

S = intensity of the source, or the hottest spot in the coded aperture image

$Bkgd$ = background, the region outside of 2.5 × FWHM

μ_{Bkgd} = mean of the background

σ_{Bkgd} = standard deviation of background.

The standard deviation was calculated as follows:

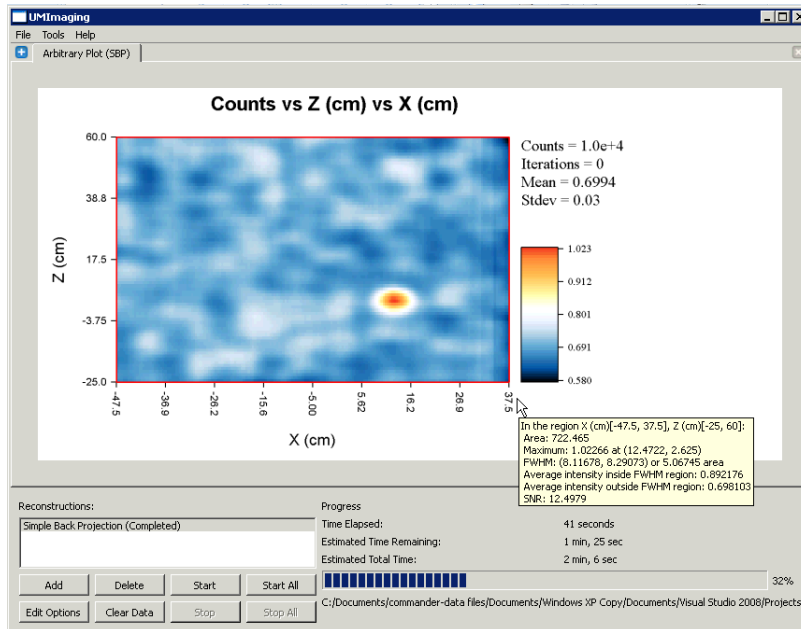$$\sigma = \sqrt{\frac{1}{N} \sum_{i=1}^{N} (x_i - \mu_{Bkgd})^2} \quad (C.2),$$

where

$$\mu_{Bkgd} = average\ background = \frac{1}{N} \sum_{i=1}^{N} x_i$$

and

N = image pixel.

These calculations were implemented in UMImaging, such that when a hotspot in the reconstructed image is highlighted by the user in the GUI, the SNR is displayed, as shown in Figure C.1.

Figure C.1: The SNR is reported in the UMImaging GUI when the hotspot in the image is highlighted.